



HAL
open science

Electrical transport in nanostructures of the Weyl semimetal WTe₂

Valentin Labracherie

► **To cite this version:**

Valentin Labracherie. Electrical transport in nanostructures of the Weyl semimetal WTe₂. Superconductivity [cond-mat.supr-con]. Université Grenoble Alpes [2020-..]; Technische Universität (Dresde, Allemagne), 2021. English. NNT : 2021GRALY019 . tel-03487115

HAL Id: tel-03487115

<https://theses.hal.science/tel-03487115>

Submitted on 17 Dec 2021

HAL is a multi-disciplinary open access archive for the deposit and dissemination of scientific research documents, whether they are published or not. The documents may come from teaching and research institutions in France or abroad, or from public or private research centers.

L'archive ouverte pluridisciplinaire **HAL**, est destinée au dépôt et à la diffusion de documents scientifiques de niveau recherche, publiés ou non, émanant des établissements d'enseignement et de recherche français ou étrangers, des laboratoires publics ou privés.

DISSERTATION

Submitted to obtain the degree of

DOCTOR OF SCIENCE

of the **UNIVERSITÉ GRENOBLE ALPES**

and of the **TECHNISCHE UNIVERSITÄT DRESDEN**

Specialty: **Physics – Condensed Matter**

Arrêté ministériel : le 6 janvier 2005 – 25 mai 2016

Presented by

Valentin LABRACHERIE

born on 19.05.1994 at Saint-Junien (France)

Thesis directed by **Romain GIRAUD** and **Bernd BÜCHNER**
co-supervised by **Joseph DUFOULEUR**

prepared from **October 2017 to May 2021**,
at the **Leibniz Institute for Solid State and Materials Research Dresden**
(**Dresden, Germany**) and the **Laboratory for Spintronics and Devices**
Technology (Grenoble, France)

as a co-tutelle thesis between the ComUE UGA and the TU Dresden

**Electrical transport in nanostructures
of the Weyl semimetal WTe_2**

Thesis defended publicly on **12.07.2021**,
in the presence of the dissertation committee:

Prof. Dr. Carsten TIMM,

Professor, Faculty of Physics - TU Dresden, Germany; Chair

Prof. Dr. Hartmut BUHMANN

Professor, Faculty of Physics - University of Würzburg, Germany; Reviewer

Dr. Walter ESCOFFIER

Associate professor, LNCMI Toulouse, France, Reviewer

Prof. Dr. Bernd BÜCHNER

Professor, Faculty of Physics – TU Dresden, Germany; Examiner

Dr. Olivier FRUCHART

CNRS research director, IRIG-SPINTEC, Grenoble, France; Examiner

Dr. Benoit JOUALT

CNRS research director, L2C University of Montpellier, France; Examiner



Abstract

Electrical transport in nanostructures of the Weyl semimetal WTe_2

by Valentin LABRACHERIE

Recently, different studies on Weyl semimetals have shown some great potential for applications in spintronics. Indeed, spin-chiral Weyl nodes are perfect sources or sinks of the Berry curvature, which give new transport properties due to their topological nature, such as the chiral anomaly, and a large anomalous Hall response. Moreover, type-II Weyl semimetals, such as WTe_2 , have a specific band structure with tilted Weyl cones and overlapping electron/hole bands that can result in a perfect charge compensation and an extremely large magnetoresistance (XMR). Yet, in WTe_2 , Weyl nodes are usually located about 50 meV above the Fermi energy, a situation that questions the observation of both a large positive XMR and a negative magnetoresistance attributed to the chiral anomaly in some studies.

In this work, we investigate the magneto-transport properties of WTe_2 nanostructures obtained by different methods (mechanical exfoliation, chemical vapor transport), considering both the real electronic band structure and scattering by disorder. Although the XMR amplitude also depends on charge mobilities, it is shown that the subquadratic response is not strongly influenced by the degree of disorder. Taking carrier densities inferred from quantum oscillations into account, a three-band model explains this behavior by a large difference in hole mobilities, as confirmed by numerical simulations. At low temperatures and for small magnetic fields, an isotropic negative magneto-resistance is observed and attributed to a topological property of the band structure far away from the Weyl nodes. This new mechanism, different from the chiral anomaly, allows us to reproduce the experimental results by numerical calculations based on the real band structure of WTe_2 .

En Français

Récemment, différentes études sur les semimétaux de Weyl ont montré leur large potentiel pour des applications en spintronique. En effet, les noeuds de Weyl avec leur chiralité de spin sont des sources ou puits parfaits de la courbure de Berry, ce qui peut conduire à de nouvelles propriétés de transport, dues à la nature topologique de la structure de bande, comme l'anomalie chirale et une large réponse liée à l'effet Hall anormal dit intrinsèque. De plus, les semimétaux de Weyl de type II, comme WTe_2 , ont une structure de bande particulière avec des cônes de Weyl inclinés et un chevauchement des bandes de trous et d'électrons qui résulte en une forte compensation de charge et une magnétorésistance extrêmement large (XMR) associée. Cependant, dans WTe_2 , les noeuds de Weyl se trouvent environ 50 meV au-dessus de l'énergie de Fermi, ce qui remet en cause la possibilité d'observer à la fois une XMR positive à fort champ et une magnétorésistance négative à champ faible due à l'anomalie chirale.

Dans ce travail, nous étudions les propriétés de magnéto-transport de nanostructures WTe_2 obtenues par différentes méthodes (exfoliation mécanique, transport en phase vapeur), avec des degrés de désordre microscopique différents, en considérant à la fois la structure de bande réelle du matériau et les processus de diffusion liés au désordre. Il est montré que la XMR présente un comportement subquadatique, qui peut être compris dans le cadre d'un modèle multi-bandes, au-delà de deux bandes, comme confirmé par des simulations numériques. A très basse température et faible champ magnétique, une magnétorésistance négative et isotrope est observée et attribuée à une propriété topologique de la structure de bandes loin des noeuds de Weyl. Ce nouveau mécanisme, différent de celui de l'anomalie chirale, nous permet de reproduire nos résultats expérimentaux par des simulations numériques basées sur la structure de bande réelle de WTe_2 .

Auf Deutsch

In den vergangenen Jahren haben verschiedene Untersuchungen von Weyl Halbleitern gezeigt, dass sich diese sehr gut als Spintronische Geräte eignen. In der Tat sind die Spin-chiralen Weyl Quasiteilchen perfekte Quellen und Abflüsse der Berrykrümmung, was auf Grund ihrer topologischen Natur neue Transporteigenschaften hervorruft, wie beispielsweise die chirale Anomalie und einen großen, anomalen Hall Effekt. Außerdem haben Typ II Weyl Halbleiter wie WTe_2 eine spezifische Bandstruktur mit gekippten Weylkegeln und überlappenden Elektronen-/Lochbändern, die dazu führen können, dass die Ladungsträgerkompensation ideal wird und ein sehr starker Magnetowiderstand (XMR) entsteht. Dennoch befinden sich die Weylknoten in WTe_2 ca. 50 meV über dem Fermi-niveau, eine Beobachtung die sowohl den starken positiven Magnetowiderstand, als auch den negativen Magnetowiderstand, der meist mit der chiralen Anomalie in Verbindung gebracht wird, in Frage stellt.

In dieser Arbeit untersuchen wir die Magnetotransporteigenschaften von WTe_2 Nanostrukturen, die durch verschiedene Wachstumsarten hergestellt werden (mechanische Exfoliation, chemische Gasphasenabscheidung), um sowohl die reale Bandstruktur, als auch Streuung an Störstellen in Betracht ziehen zu können. Es wird gezeigt, dass der extrem große Magnetowiderstand nicht direkt vom Grad der Unordnung abhängt und dass das typisch subquadratische Verhalten im Rahmen eines Multibandmodells, was über das Zweibandmodell hinaus geht, verstanden werden kann und sich auch mit numerischen Simulationen bestätigt lässt. Bei tiefen Temperaturen und für kleine Magnetfelder kann ein isotropisch negativer Magnetowiderstand beobachtet werden, der der topologischen Eigenschaft der Bandstruktur weit weg von den Weylknoten geschuldet ist. Dieser neue Mechanismus, der sich von der chiralen Anomalie unterscheidet, erlaubt es uns die experimentellen Ergebnisse mit numerischen Berechnungen, die auf der realen Bandstruktur basieren, zu reproduzieren.

Dedicated to my parents and my brother.

Acknowledgements

To complete this doctoral project, it is important to look around and see all the people who helped, formed or supported this work along the way, and I would like now to thank them. To do so, I will switch to French for the French speakers.

J'aimerai remercier Joseph et Romain pour m'avoir donné l'opportunité de travailler avec eux et de m'avoir appris tant de choses ces dernières années. Cela n'a pas toujours été facile, certainement dû à mon tempérament mais je vous remercie de m'avoir accueilli dans votre équipe, soutenu et supporté. En plus des travaux scientifiques, c'est aussi une ouverture sur le monde que j'ai entrepris en partant vivre à l'étranger et cela je le dois à vous. J'aimerai aussi remercier Louis qui est de retour à l'IFW pour nous régaler (littéralement). J'ai l'impression que c'était encore hier que je venais dans ton bureau à l'institut Néel pour te demander conseil avant d'accepter ce projet de thèse.

I would like to thank Prof. Dr. Büchner for giving me the opportunity to do my doctoral thesis in Dresden. I am very grateful for the great environment that the IFW Dresden provides to its PhD students.

I would like to acknowledge the member of the Jury and specifically thank Dr. Walter Escoffier and Pr. Dr. Hartmut Buhmann for their time.

I am grateful to Grigory, Felix, Dr. Saicharan and Dr. Hampel for their continued work on the growth of WTe₂ crystals. I would like to thank Dr. Sykora for all his help on the numerical simulations. I want to thank Barbara Eichler and Sandra Nestler for their help in the preparation of the samples. I would like to acknowledge Kerstin Höllerer, Katja Schmiedel and Rita Taubert for their administrative support.

In the quantum transport group, when I arrive there was no other PhD student and now, we are 7 including Louis group. I am grateful to be join just after by Aoyu that always make us laugh in the office with almost nothing ;-). I would like to thank Teresa for her kindness, her patience and her craziness (to not feel alone). A thanks also for helping me with the German version of the abstract. Un français qui m'a fait me sentir moins seul durant des débuts difficiles et qui aura réussi à toujours introduire une ou deux citations de Kaamelott durant nos discussions parfois compliquées sur PtBi₂, merci à toi Arthur. I would like also to thank Kyril for the exfoliation of WTe₂ that save me precious time at a moment where I had none.

Pour arriver où j'en suis aujourd'hui, cela n'a pas été un voyage facile mais j'ai pu compter sur des personnes incroyables qui ont toujours été là pour m'aider et cela commence par ma famille. Merci à mes parents et à mon frère qui ont toujours su

m'épauler ou me contenir dans les moments plus difficiles. J'aimerais remercier toute ma famille et tout particulièrement mon parrain.

I would like to thank Riswati for her patience with me and all the love and strength that she gave me during these past years. It would have been very difficult without you. . .

J'aimerais aussi remercier ma seconde famille, mes amis, qui sont si inestimables que je n'ai pas les mots. Une partie à Bordeaux avec Thomas (oui je t'inclus dans Bordeaux et non Paris ;-)), Guillaume et Benjamin que je ne peux pas remercier assez pour ces moments de défoulement en jeu en ligne dont j'avais besoin pour m'évacuer la tête. Une autre partie à Grenoble, avec ceux qui ont fait de mes années de Master, une des plus belles parties de ma vie jusqu'à maintenant. Flora, Nicolas, Clara, Sébastien, Jérémy, Léo et Loïc, merci. Même si je n'ai pu être longtemps à Bordeaux ou à Grenoble ces dernières années, j'ai toujours réussi à sentir votre soutien durant ces années de doctorat.

TABLE OF CONTENTS

EXTENDED SUMMARY	15
------------------------	----

CHAPTER 1

INTRODUCTION TO TOPOLOGICAL CONCEPTS	19
--	----

1.1 Topology of electronic bands	20
1.1.1 Berry Curvature	20
1.1.2 Topological invariants	22
1.1.3 Topological classification	23
1.2 Quantum Hall effect and Topological Insulators	25
1.2.1 Integer Quantum Hall Effect	25
1.2.2 2D Z_2 Topological Insulator : Quantum Spin Hall effect	26
1.2.3 3D Z_2 Topological Insulator	30

CHAPTER 2

TOPOLOGICAL SEMIMETALS	33
------------------------------	----

2.1 Construction of Dirac and Weyl Semimetals	34
2.2 Transport properties of Topological Semimetals	37
2.2.1 Discovery and Fermi arcs	38
2.2.2 Anomalous Hall Effect	38
2.2.3 Extremely Large Magnetoresistance	40
2.2.4 Chiral Anomaly	42
2.3 WTe_2 : a type II Weyl semimetal	43
2.3.1 Band structure	43
2.3.2 Indication of Weyl orbits due to the Fermi arcs	46
2.3.3 Type-II nature	48
2.3.4 Planar Hall effect	49

CHAPTER 3

CRYSTAL GROWTH AND EXPERIMENTAL TECHNIQUES	51
--	----

3.1 Growth of WTe_2	52
3.1.1 Crystal structure	52
3.1.2 Chemical Vapor Transport Growth	53

3.1.3 Flux Growth	56
3.2 Nanostructures of WTe ₂	58
3.2.1 Exfoliation and search of nanostructures	58
3.2.2 Nanofabrication	60
3.3 Cryogenics and low noise measurement techniques	62
3.3.1 ³ He- ⁴ He dilution refrigerator system	63
3.3.2 Low noise electrical measurements	64

CHAPTER 4

EXTREME MAGNETORESISTANCE : BAND STRUCTURE AND DISORDER 67

4.1 Motivation	67
4.2 Temperature dependence of the longitudinal resistivity	68
4.3 Extreme magneto-resistance	69
4.3.1 Simple analysis of the experimental results	69
4.3.2 Refinement based on the Shubnikov-de Haas measurements	72
4.3.3 Comparative study	75
4.4 Multi-band model	76
4.4.1 Formalism	76
4.4.2 From a two-band to a three-band model	77
4.5 Numerical simulations	81
4.5.1 Projective renormalization method	81
4.5.2 Results	84
4.6 Conclusion	87

CHAPTER 5

TOPOLOGY AND TRANSPORT PROPERTIES AT VERY LOW TEMPERATURE 89

5.1 Motivation	89
5.2 Low-field transport properties	90
5.2.1 In-plane Magnetoresistance at 4.2K	90
5.2.2 Very low temperature dependence of the longitudinal resistance	92
5.2.3 Isotropic negative magneto-resistance	93
5.3 Theory and discussion	96
5.4 Conclusion	100

CHAPTER 6

CONCLUSION 101

BIBLIOGRAPHY	105
APPENDIX A	
TWO-BAND MODEL FITS OF S3 DATA	119
APPENDIX B	
TYPE II WEYL SEMIMETALS INFORMATIONS	121
APPENDIX C	
COLD FINGER DESIGN	123
LIST OF FIGURES AND TABLES	127
LIST OF PUBLICATIONS	129
ABSTRACT EN FRANÇAIS	131
ABSTRACT AUF DEUTSCH	135
DECLARATION OF AUTHORSHIP	139

EXTENDED SUMMARY

One severe limitation of the development of electronics devices nowadays is the power consumption. Following the Moore's law, the number of transistors in integrated circuits has doubled every year for decades. While the size of logical components continues to decrease, the power consumption due to interconnects is so large that it can strongly heat up nearby components and even damage them. A possible way to overcome this issue is to use spin currents, which can even be dissipationless [Sonin, 2010] [Šmejkal et al., 2017]. In this branch of spintronics, emergent materials are studied in order to find some which can generate, detect and manipulate large spin currents, or simply propagate them. One class of such materials is that of topological materials that have chiral spin textures due to strong spin-orbit coupling, with gapless quasi-particles that are robust against perturbations, in particular to disorder.

Among these, topological Weyl semimetals were rapidly identified as a new family of interest to investigate chiral spin transport. Among massive bands, their bulk band structure exhibits linear quasiparticle excitations, called Weyl fermions that have a well-defined spin chirality [Armitage et al., 2018]. Thus, contrary to 3D topological insulators, Weyl semimetals have topological surface states but also gapless topological bulk states. These bulk states come as pairs of Dirac cones of opposite spin chirality, called Weyl cones, related to each other by Fermi arcs that connect their two projected Weyl nodes at the surface. Important for bulk transport properties is that pairs of Weyl nodes are a perfect source or sink of Berry curvature. Each cone having its own chirality, Weyl fermions are expected to induce new effects such as a large intrinsic anomalous Hall effect or a negative magnetoresistance related to the chiral anomaly. The latter results from a quantum anomaly that induces a charge transfer between cones of opposite chirality, for parallel electric (E) and magnetic (B) fields. Since the chiral anomaly only exists if B is applied along E , it is associated to an anisotropic magnetoresistance and, therefore, could also give a contribution to the planar Hall effect.

The anisotropic magnetoresistance and the planar Hall effect were indeed reported for thin films of the type-II Weyl semimetals WTe_2 , for instance. Different groups studied the anisotropic planar hall effect [Li et al., 2019b] or the chiral anomaly

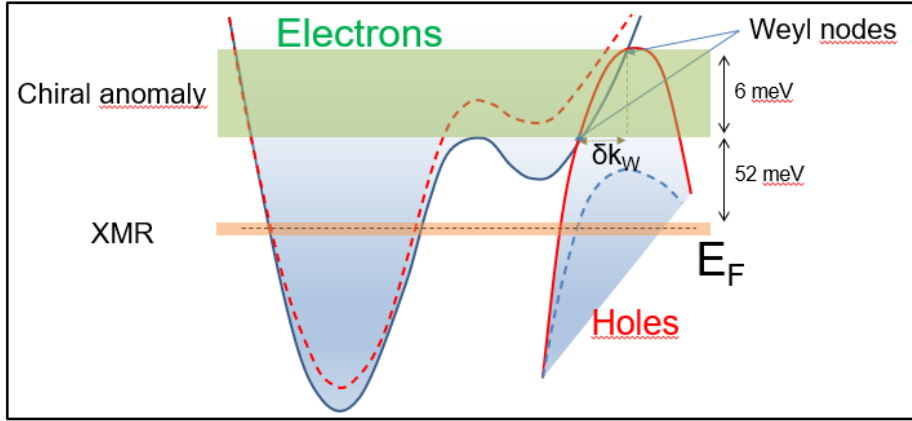


FIGURE 1: Illustration of the band structure of WTe₂ with the Weyl nodes indicated by the two arrows. The spin degeneracies of the conduction and valence bands are lifted by the spin-orbit coupling, leading to two bands slightly shifted in energy (plain and dashed lines). Two important energy levels are indicated in the bandstructure, in orange for perfect compensation ($n = p$), giving rise to two spin nondegenerate electron and hole pockets contributing to the transport and in green where the realization of the chiral anomaly takes place.

[Wang et al., 2016a] [Li et al., 2017b] [Lv et al., 2017] [Zhang et al., 2017]. For very thin samples, below 10 nm, a gradual opening of the band gap appears [Zheng et al., 2016]. In the few or monolayer limit, some recent work revealed the effect of the Berry curvature on the transport properties. The observation of a non-linear anomalous Hall effect was reported [Kang et al., 2019] [Ma et al., 2019] [Wang and Qian, 2019], a quantum spin hall effect was evidenced [Tang et al., 2017] [Fei et al., 2017] [Wu et al., 2018], and canted spin textures were predicted [Garcia et al., 2020]. WTe₂ has a non-centrosymmetric structure with a strong spin-orbit coupling that leads to the prediction of a large spin Hall effect [Zhao et al., 2020]. Several studies focused on the application of the properties of WTe₂ for the development of spin current sources in memory and logic devices [Shi et al., 2019] [Zhao et al., 2020]. Importantly, due to its type II nature, the specific band structure of WTe₂ is made of crossing conduction and valence bands leading to the coexistence of electron and hole pockets, for which a charge compensation is possible. The hole-electron coexistence results in an extremely large magnetoresistance that was evidenced in both bulk [Ali et al., 2014] [Luo et al., 2015] and thin films [Thoutam et al., 2015]. This magnetoresistance is not related to topological properties but is of high interest for extracting transport parameters such as carrier mobilities and densities. For thin nanostructures, a study of the Shubnikov-de Haas oscillations of bulk and thin film reported on a change in the bandstructure for samples in the range of 40 to 10 nm, with an increasing band gap opening [Xiang et al., 2018]. This leads to a change in the carrier densities, but the Fermi energy remains pinned at the near-perfect charge compensation.

Thus, simple considerations based on the simplified band structure, as sketched in figure 1, already raise important questions about the interpretation of transport results in terms of topological properties. First, the Weyl nodes are offset from the charge compensation energy, by about 50 meV. This casts doubts about the observation of both the XMR and the chiral anomaly for a given charge doping. In general, the Fermi energy in WTe_2 is located nearby the charge compensation regime, and the XMR is well evidenced at low temperature. This implies that the observation of the chiral anomaly is unlikely at such a Fermi energy. Another feature related to the extremely large magnetoresistance did not find any origin yet : it was reported that the band structure can be approximated by a two-band model at the perfect compensation, which leads to a quadratic magnetoresistance with no saturation even at high magnetic fields as large as 60 T [Ali et al., 2014]. Nevertheless, a slightly subquadratic law is always reported with no explanation [Thoutam et al., 2015] [Wang et al., 2016b] [Fatemi et al., 2017] [Wang et al., 2019]. Second, even if the Fermi energy could be raised towards the Weyl nodes, the influence of disorder cannot be neglected since inter-node scattering can efficiently suppress the topological contribution to charge transport [Sykora et al., 2020b]. As evidenced in this thesis (chapter 5), the negative magnetoresistance can nevertheless be related to the non trivial topology of the band structure far from the Weyl nodes, beyond the Lifshitz transition.

In this thesis, both the high-field positive XMR and the low-field negative MR are investigated in detail, by studying the magneto-transport properties of disordered WTe_2 nanostructures obtained by different growth techniques, with different degrees of disorder. The manuscript has five chapters. Chapter 1 gives a general introduction to topological concepts, with a review of both the quantum Hall effect and topological insulators. In chapter 2, the topological Weyl semimetal phase is introduced, and its specific transport properties are discussed. In chapter 3, the growth methods, the nanofabrication and the measurement set-up are described in detail. The last two chapters focus on the results obtained during this PhD thesis. Chapter 4 reports on a study of the transport properties of WTe_2 at large magnetic fields and describes the extremely large magnetoresistance in the framework of a multiband model. The influence of the disorder strength and range (short range versus long range) on the extremely large magnetoresistance is then investigated, by comparing the experimental results, obtained with nanostructures of different densities of point defects, to numerical calculations. In chapter 5, the observation of an isotropic negative magnetoresistance is newly interpreted as the influence of the Weyl fermions far away from the Weyl nodes, as evidenced by numerical calculations. Our experimental study gives some robust proof to discard the chiral anomaly as the origin of the negative magnetoresistance in WTe_2 . Instead, the new mechanism

identified in this work reveals that a non-trivial topological contribution to charge transport also exists for a Fermi energy pinned in the charge-compensation regime, even if far from the Weyl nodes, a condition that is indeed realized in WTe_2 .

Chapter 1

INTRODUCTION TO TOPOLOGICAL CONCEPTS

In the 80s, Thouless and Haldane [Kosterlitz and Thouless, 1973] [Haldane, 1983] revolutionized the classification of electronic phases by introducing the concept of topological phases. Contrary to Landau's approach which classified the different phases based on their symmetry breaking in real space and for which an order parameter can be defined, which is finite in the ordered phase and vanishes in the higher-symmetry phase, the identification of different topological phases is based on symmetry considerations in the reciprocal space, which alter the electronic band structures. Due to their topological nature, topological phases are robust against any small perturbation. Although discovered first, the integer quantum Hall effect was more complex to understand because it actually breaks all symmetries. Almost 30 years after the discovery of the quantum hall effect, the concept of topological phases was deeply revisited with the theoretical and experimental discovery of 2D \mathbb{Z}_2 topological insulators (TI), known as the quantum spin Hall phase, shortly followed by their 3D counterpart. Due to their topological nature, these electronic phases are not destroyed by small modifications of their Hamiltonian. In particular, \mathbb{Z}_2 TIs are robust against non-magnetic disorder, so that strong localization is not possible.

In this chapter, some concepts that are necessary to understand the emergence of topological phases in condensed matter are introduced in the first part. These concepts, such as the Berry curvature and the topological invariants are explained in analogy to the topology of 3D surfaces, which is easier to visualize. The classification of the quantum phases of matter in terms of topological invariants is reviewed. In a second part, a brief overview is given of some topological phases in 2D, such as the orbital based QHE or the spin-based QSH, and finally, the case of 3D topological insulators is discussed. The case of Weyl semimetals will be presented in the next chapter.

1.1 Topology of electronic bands

1.1.1 Berry Curvature

The concept of geometrical phase was introduced by Berry in 1984 [Berry, 1984] to understand the adiabatic evolution of the phase in quantum systems. To describe this effect, the evolution of an eigenstate $\psi(t)$ with a phase $\Phi(t)$ of the Hamiltonian \mathcal{H}_λ is considered, controlled by the time-dependent parameter $\lambda = (\lambda_1, \lambda_2, \dots)$. This parameter varies slowly in time along a path \mathcal{P} in the parameter space. According to the adiabatic theorem, the system will remain in the same eigenstate of \mathcal{H} but, its phase evolves after a time t , the wave function can be generally written as:

$$|\psi(t)\rangle \approx e^{i\Phi(t)} |\psi_\lambda(0)\rangle \quad (1.1)$$

The phase Φ has two contributions, the first one is the dynamical phase that is related to the eigenenergy :

$$\Phi_{dyn} = -\frac{1}{\hbar} \int_0^t E_{\lambda(t')}^{(n)} dt' \quad (1.2)$$

The second one is the geometrical one, which is the Berry phase [Berry, 1984]. To calculate the Berry phase, the basis of eigenstates $|\psi_\lambda^{(n)}\rangle$ of the Hamiltonian \mathcal{H}_λ is introduced. The Berry connection [Berry, 1984][Berry, 1989] is defined as :

$$\mathcal{A}_\lambda^{(n)} = i \langle \psi_\lambda^{(n)} | \nabla \psi_\lambda^{(n)} \rangle \quad (1.3)$$

The geometrical phase is then given by :

$$\Phi_{geom} = \int_{\lambda(0)}^{\lambda(t)} \mathcal{A}_\lambda^{(n)} d\lambda \quad (1.4)$$

This phase becomes time independent when the Berry connection is integrated along a closed loop \mathcal{C} for which $\lambda(T) = \lambda(0)$ (figure 1.1).

Introducing the Berry curvature :

$$\Omega_\lambda^{(n)} = \nabla \times \mathcal{A}_\lambda^{(n)} \quad (1.5)$$

and using the Stokes theorem, the Berry phase can be rewritten as :

$$\Phi_{geom} = \iint_{\Sigma} \vec{n} \cdot \vec{\Omega}_\lambda^{(n)} d\lambda \quad (1.6)$$

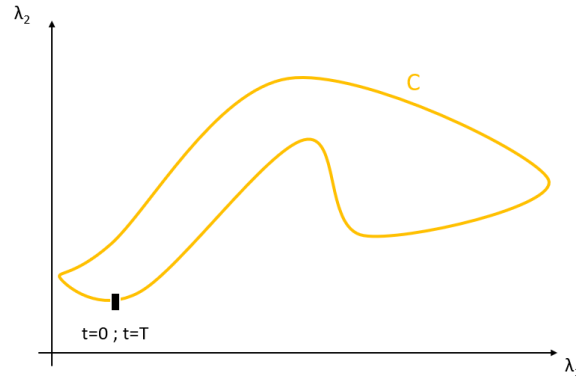


FIGURE 1.1: Path \mathcal{C} in the parameter space followed by the system to acquire a Berry phase

with \vec{n} the normal direction to the surface Σ . The geometric phase is therefore the integration of the Berry curvature on a surface Σ enclosed by the path \mathcal{C} described by the time-dependent parameter.

To better understand this geometric phase, an analogy can be made with a classical system in a time-dependent rotating frame, a Foucault pendulum on Earth. As known, the rotation of the Earth influences the oscillation of a Foucault's pendulum (Coriolis force). After one day, the Earth has done one turn, so that the pendulum is back to its original position. Considering a linear oscillation of the pendulum, the movement remains the same but the rotation plane has changed by an angle θ (similar to the Berry phase) due to the rotation of the Earth [Dalibard, 2016] as shown in figure 1.2.

From a mathematical concept, the next part considers how this Berry curvature is related to the notion of topological invariant, which is used to classify novel quantum states in condensed matter.

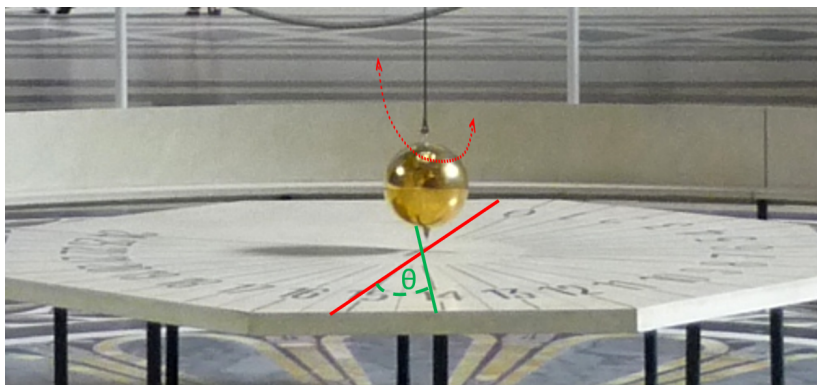


FIGURE 1.2: Foucault's pendulum at the Pantheon in Paris, with red lines showing the plane of the linear rotation and green lines showing the plane of the rotation after 24 hours, θ being the angle between the two planes and corresponding to the geometric phase

1.1.2 Topological invariants

To introduce qualitatively the notion of topological invariant, an analogy with the topology of 3D surfaces is often made. Such objects can be sorted in different classes defined by an integer, the genus g , that represents the number of holes in such 3D surfaces. Considering a mug, a non-trivial 3D surface with a single hole ($g = 1$), it is possible to continuously distort the mug into a donut. However, it is not possible to transform a ball (no hole, $g = 0$) into a donut since they do not have the same genus. Therefore, these two objects belong to different topological classes as shown in figure 1.3.

In condensed matter, a similar description can be made when considering electronic band gaps of Bloch states in a crystal. Thouless and Haldane discovered that band gaps are not all topologically equivalent. One way to understand it is to make the link to the genus presented above. Instead of surfaces in real space, one has to consider surfaces in the reciprocal space, within the Brillouin zone [Ralph, 2020]. For a given band n in a 2D system, the topological invariant is given by the total Berry flux in the Brillouin zone :

$$C_n = \iint_{\text{BZ}} \Omega^{(n)}(k) d^2k \quad (1.7)$$

Because the Berry phase is not single valued (modulo 2π), $C_n = \Phi/2\pi$ is an integer that cannot change smoothly, so that bands are not all topologically equivalent and are distinguished by their topological invariant. Generally, it was shown that every crystal can be characterised by a set of topological invariants, associated to various topological phases that can be classified by considering specific symmetries of the Hamiltonian \mathcal{H} [Chiu et al., 2016]. For example, the Chern number is the first topological invariant defined in the case of the Hall effect.

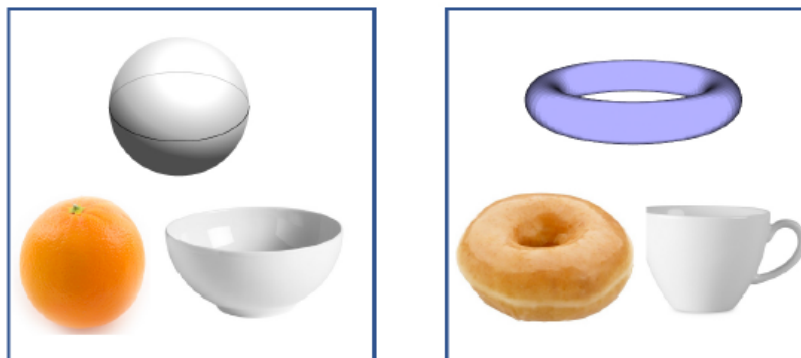


FIGURE 1.3: Comparison of 2 classes of 3D objects (genus equal to 0 and 1). Adapted from [Dalibard, 2016]

1.1.3 Topological classification

Single particle Hamiltonians are classified into ten classes by local and internal symmetries [Altland and Zirnbauer, 1997] that are the time reversal symmetry Θ , the particle hole symmetry Ξ and the sublattice or chiral symmetry Π . Several methods such as homotopy group or K-theory can derive the same tenfold classification [Kitaev, 2009]. Considering a single-particle wave function where the Bloch theorem is respected and the Hamiltonian ("second quantization") has the following form [Ryu et al., 2010] :

$$\mathcal{H} = \sum_k \sum_{i,j} \psi_i^\dagger(k) \mathcal{H}_{i,j}(k) \psi_j(k) \quad (1.8)$$

where the sum over the crystal momentum k is on the full Brillouin zone, i and j denotes the quantum number for the spin and band indices. ψ and ψ^\dagger are the fermion operators of creation and annihilation respectively. $\mathcal{H}_{i,j}$ is a $N \times N$ matrix and is the "first quantization" Hamiltonian. It is assumed that there is no unitary matrix that commutes with the Hamiltonian matrix $\mathcal{H}_{i,j}$: if such a matrix exists, the Hamiltonian \mathcal{H} can be transformed into a block diagonal form and each block can be treated separately. In physics, the two symmetries that play a crucial role are the time reversal symmetry and the particle-hole symmetry. Due to the previous assumption on the Hamiltonian, these two are anti-unitary operators Θ and Ξ respectively that are acting on the Hamiltonian as follow :

$$\Theta \mathcal{H}(k) \Theta^{-1} = \mathcal{H}(-k) \quad \Xi \mathcal{H}(k) \Xi^{-1} = -\mathcal{H}(-k) \quad (1.9)$$

The product of these two operators that anti-commute can also be considered, which defines the chiral operator :

$$\Pi \mathcal{H}(k) \Pi^{-1} = -\mathcal{H}(k) \quad (1.10)$$

Now looking at the square of this three operators, it gives :

$$\Theta^2 = \pm 1, \quad \Xi^2 = \pm 1, \quad \Pi^2 = 1 \quad (1.11)$$

Considering all possible combinations of these symmetries, it was possible to identify 10 inequivalent topological classes as described in figure 1.4. For the first symmetry, the Hamiltonian can either be non time reversal invariant $\Theta = 0$, or time reversal invariant with the anti unitary time-reversal symmetry operator Θ squared to plus the identity operator, in which case $\Theta = +1$, or to minus the identity

operator, in which case $\Theta = -1$. Similarly, there are three possibilities for the particle hole symmetry. With these two symmetries, nine classes are defined. Looking at the chiral symmetry, this symmetry is always guaranteed when the two others are already present but can be independently determined otherwise. This means that for a system without time reversal symmetry $\Theta = 0$ and particle hole symmetry $\Xi = 0$, the chiral symmetry Π can be either 0 or 1. This brings the classification to the ten ways that an Hamiltonian can respond in the absence of interaction between the particles as seen in figure 1.4. The system related to the Hamiltonian can be either trivial (equivalent to vacuum) or non-trivial with the two classes : \mathbb{Z} or \mathbb{Z}_2 . In particular, this classification includes the Quantum Hall effect QHE and the \mathbb{Z}_2 TIs.

Classes	Symmetry			p =	8	1	2	FS1
	θ	Ξ	Π	p =	2	3	4	FS2
AZ	θ	Ξ	Π	d =	1	2	3	Gap systems
A	0	0	0		0	Z	0	
AIII	0	0	1		Z	0	Z	
AI	1	0	0		0	0 ^a	0	
BDI	1	1	1		Z	0	0 ^a	
D	0	1	0		\mathbb{Z}_2^b	Z	0	
DIII	-1	1	1		$\mathbb{Z}_2^{a,b}$	\mathbb{Z}_2^b	Z	
AII	-1	0	0		0	$\mathbb{Z}_2^{a,b}$	\mathbb{Z}_2^b	
CII	-1	-1	1		2Z	0	$\mathbb{Z}_2^{a,b}$	
C	0	-1	0		0	2Z	0	
CI	1	-1	1		0 ^a	0	2Z	

FIGURE 1.4: Classification of topological states in quantum matter. The superscript a means that surface states and stable bulk Fermi surfaces of type FS2 can be protected by a \mathbb{Z} invariant; the superscript b means that \mathbb{Z}_2 protect only FS of dimension 0 at high symmetry points (FS1) and cannot protect FS away from high symmetry points (FS1).

Adapted from [Chiu et al., 2016]

Later developments [Zhao and Wang, 2013][Chiu et al., 2016] that are discussed in the next chapter enriched the classification to take into account gapless metallic and semimetallic topological states. Indeed, the topological invariant in a Dirac or Weyl semimetal over the entire Brillouin Zone is zero but some Fermi surfaces possess a non-trivial topology when the topological invariant is integrated over a restricted area. To take into account this local non-trivial topology, a new parameter needs to be defined which is the codimension $p = d - d_{\text{FS}}$ with d and d_{FS} the dimension of the Brillouin zone and of the Fermi surface respectively. This new parameter allows us to use the same classification for these new materials. Also, two cases have to be distinguished. The first one is if each individual Fermi surface is left invariant by

the non spatial AZ symmetry (symmetry that the Altland Zirnbauer class exhibits) in other words, if the Fermi surface is located at high symmetry points (FS1) such as 2D nodal superconductors with time-reversal symmetry. The other case will be for Fermi surfaces that are off high symmetry points (FS2) like Weyl or Dirac Fermi surfaces.

In the classification and depending on the dimension, the system can be either in a topologically trivial state, equivalent to vacuum, or a non-trivial one equivalent to the group \mathbb{Z} or \mathbb{Z}_2 . For example the QHE corresponds to the class A which is topological in 2D but not anymore in 1D or 3D.

1.2 Quantum Hall effect and Topological Insulators

This section briefly reviews some important phases identified as topologically non-trivial systems, which led to the topological classification of insulators in condensed matter physics. Although the importance of topology in physics was anticipated by Weyl already since mid-20th century, a major breakthrough came with the understanding of the integer quantum Hall effect in terms of band topology in the 1980's [Thouless et al., 1982]. A new impulse was then given by the prediction of \mathbb{Z}_2 topological insulators, both in 2D [Kane and Mele, 2005] [Murakami et al., 2004] and 3D [Fu et al., 2007].

1.2.1 Integer Quantum Hall Effect

When a 2D electron gas is placed under a magnetic field, the motion along closed circular orbits induces quantized values of the wave vector which leads to the formation of Landau levels in the energy spectrum, with an energy $E_n = \hbar\omega_c(n + \frac{1}{2})$ with ω_c the cyclotron frequency ($\omega_c = \frac{eB}{m}$) and n is an integer related to the number of the Landau level. The quantization of the energy spectrum opens gaps in the DOS. Nevertheless, close to the edges, cyclotron orbit cannot be closed, skipping orbits emerge and transport occurs along edge channels (figure 1.5). In that case, the transverse (Hall) conductance is quantized and equal to [Klitzing et al., 1980][Prange and Girvin, 1990] :

$$\sigma_{xy} = N \frac{e^2}{h} \quad (\text{and } \sigma_{xx} = 0) \quad (1.12)$$

The difference between the quantum Hall phase and an ordinary insulator is evidenced by the Kubo formula that reveals that the number of Landau levels is equivalent to the Chern number (the topological invariant in the QHE) [Thouless et al., 1982]. Halperin predicted in 1982 that gapless states appear at the interface

between systems with different Chern numbers [Halperin, 1982]. This demonstrated the topological nature of the edge states at the interface between the 2D gas in the quantum Hall regime and a trivial insulator. Due to its topological origin, the Hall conductance is quantized with a very high precision and this effect is used in the metrology for the determination of the quantum of conductance $\frac{e^2}{h}$.

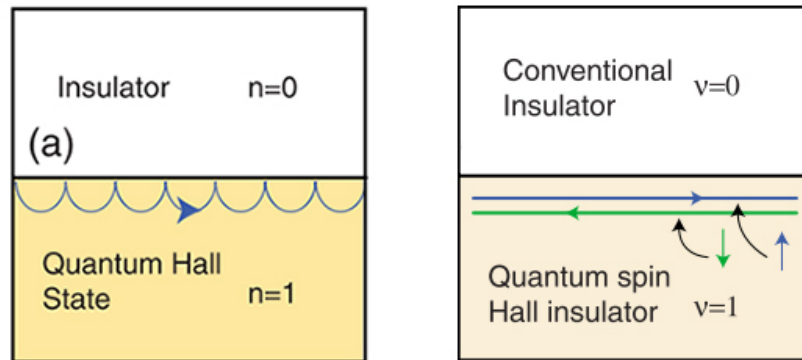


FIGURE 1.5: Representation of the interface between a normal insulator and (a) a Quantum Hall state with the emergence of skipping orbits and (b) a Quantum spin Hall state with the emergence of edge states. Adapted from [Hasan and Kane, 2010]

1.2.2 2D \mathbb{Z}_2 Topological Insulator : Quantum Spin Hall effect

About 25 years later, another breakthrough was the prediction of the quantum spin Hall effect (QSHE) in graphene by Kane and Mele [Kane and Mele, 2005] and in HgCdTe by Murakami et al. [Murakami et al., 2004], where 1D edge states are induced by the presence of a very strong spin-orbit coupling but in absence of any external magnetic field (no time reversal symmetry breaking). This new phase is also known as the 2D topological insulator state (2DTI) and it was indeed rapidly evidenced in HgCdTe quantum wells [König et al., 2007].

The 2D TI state can be seen as two copies of the quantum Hall effect with a lifted spin degeneracy, one considering the edge states for the spin up, the second for the spin down. This lifted spin degeneracy is due to the large spin-orbit coupling and not to the magnetic field. Therefore, whereas a magnetic field is required to break the time reversal symmetry for the QHE, the time reversal symmetry can be restored for the QSHE. This effect was first predicted in graphene in presence of a strong spin-orbit coupling. Nevertheless, it appears to be very difficult to induce a large spin-orbit interaction in graphene (light element) preventing the observation of any QSHE in early studies.

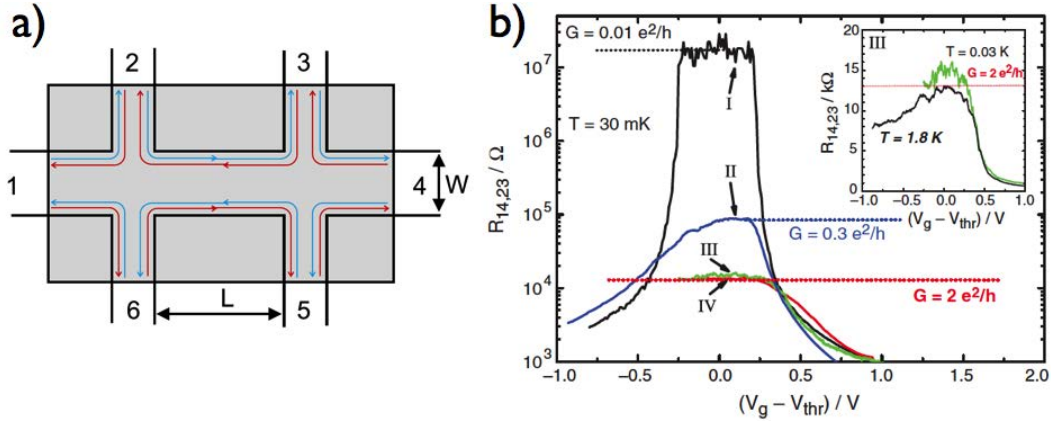


FIGURE 1.6: a) Representation of the edge channel in a 2DTI Hall bar. Adapted from [König et al., 2008]. b) Observation of the edge states quantized conductance (samples III and IV) in a gate voltage study of Hall bar samples with different thicknesses. Adapted from [König et al., 2007]

Despite the impossibility of the realization of the QSHE in graphene, a 2D TI was predicted in 2006 [Bernevig et al., 2006] and evidenced one year later in HgTe based heterostructures [König et al., 2007]. Such CdTe/HgTe/CdTe heterostructures are characterized by a strong spin-orbit coupling and are non magnetic (time reversal symmetry preserved). It was clearly identified that a band inversion occurs in HgTe which leads to the crossing of the valence and conduction band at the edges of the sample, in the vicinity of the interface with the vacuum (or any trivial insulator). Contrary to the chiral QHE state, transport occurs along helical edge modes, with no net charge transport but counter-propagating opposite spin states due to the spin-orbit coupling (see figure 1.5). Due to this spin-momentum locking, the backscattering by a non-magnetic disorder is forbidden since a charge carried by a given edge state cannot be backscattered without flipping its spin, a mechanism which is not allowed in the presence of a non-magnetic disorder (or more generally in the absence of any time reversal symmetry breaking). As a consequence, the edge states are purely ballistic and have a quantized conductance of $G_0 = \frac{2e^2}{h}$ as shown in figure 1.6.

Several issues concerning CdTe/HgTe heterostructures limit the potential applications. Despite the strong expertise of some groups in the growth of materials of interest for application in infrared detector area, the quality and the complexity of the heterostructures required for the QSHE remains extremely challenging. Furthermore, the small energy of the spin-orbit gap for a quantum well with a thickness of 8.5 nm, around 40 meV [König et al., 2008], remains very small for possible room temperature application and those systems can only be measured at low temperature ($T < 2$ K).

Other systems were evidenced as QSH insulator, InAs/GaSb heterostructures [Liu et al., 2008] and very recently monolayers of WTe_2 [Qian et al., 2014][Tang et al.,

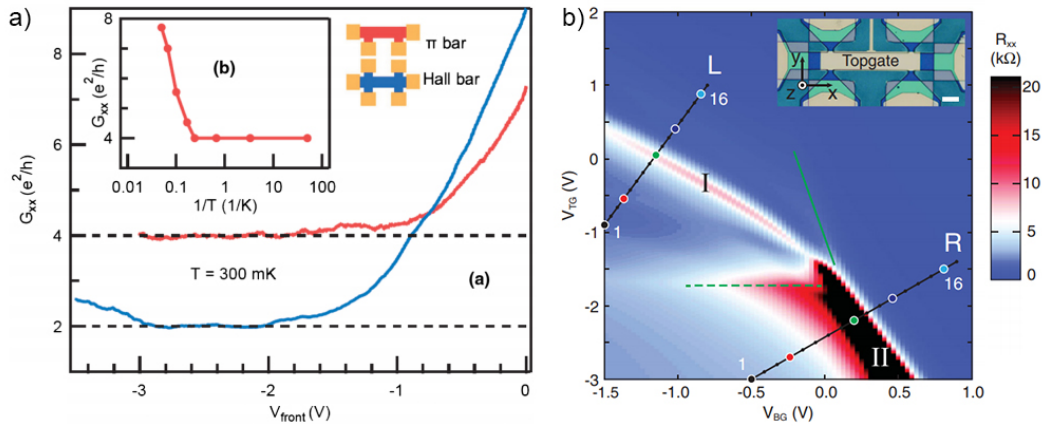


FIGURE 1.7: a) Wide conductance plateaus quantized to $2 e^2/h$ and $4 e^2/h$, respectively, for two device configurations shown in inset, both have length $2 \mu\text{m}$ and width $1 \mu\text{m}$. Adapted from [Du et al., 2015]. b) Four terminal longitudinal resistance (R_{xx}) as a function of the voltage applied on the top and bottom gate measured at 300 mK, showing the phase diagram of the InAs/GaSb. Lines L and R cross the two different gapped regions (resistance peaks), labeled as I (QSHE) and II (trivial insulator). Inset shows the optical image of the Hall bar. The scale bar represents $20 \mu\text{m}$. Adapted from [Qu et al., 2015]

2017][Wu et al., 2018]. For III-V heterostructures, the electron and hole bands are tuned by changing the thickness and doping of the InAs and GaAs layers, which can therefore result in an inverted band structure with topological properties. A dual-gate study indeed showed the possibility to drive such a semiconductor multilayer into a QSH state or a trivial insulator [Qu et al., 2015], as shown in figure 1.7. [Du et al., 2015] reported the observation of quantized plateaus in Pi and Hall bar, at respectively $4 e^2/h$ and $2 e^2/h$ up to 4 K as shown in figure 1.7. Contrary to the case of HgTe QW, the topological state persists with an in-plane magnetic field up to 12 T contrary to what is expected by a single-particle approach. It was recently suggested that the deviation observed from a single particle model might be attributed to some attractive Coulomb interaction between electrons in the InAs layer and holes in the GaSb layer [Du et al., 2017].

Even for this materials, one important limitation is that the band gaps of existing QSH insulators are too small, which limits the operating regime to low temperatures. To overcome these difficulties, new predictions were made to enhance the spin-orbit in graphene [Lara-Avila et al., 2015] [Yang et al., 2011]. As an example, the graphene can be decorated with adatoms, adatoms act as a spin-orbit scattering sources. If an electron from the graphene tunnel to the adatoms and then tunnel back by a spin-independent process, this effect can enhance locally the spin-orbit coupling. The enhancement of the QSH effect was predicted for Indium or Thallium adatoms [Weeks et al., 2011] [Cresti et al., 2014], however, no presence of the QSH effect was reported in transport studies so far [Jia et al., 2015] [Chandni et al., 2015].

Another interesting point is the realization of a QSH in a twisted bilayer of graphene [Finocchiaro et al., 2017]. This twisted structure has a reduced interlayer coupling. It is then possible to set the first layer in the Quantum Hall state $n = 1$ while the other is in the QH state $n = -1$ to construct a pair of helical edge states. Conductance plateaus were indeed observed in this heterostructure for a magnetic field of 1.5 T [Sanchez-Yamagishi et al., 2017]. However, in this approach, the QSH is achieved by applying a large magnetic fields, instead of being induced by SO coupling.

To go further, several groups searched for 2D materials exhibiting a stronger spin-orbit coupling than graphene, leading to a larger gap [Cao and Chen, 2019]. Two classes of materials are showing promising results recently. The first class is that of Xenes (family of graphene) [Zhao and Wang, 2020] with stanene [Deng et al., 2018], bismuthene [Song et al., 2014]; the second one is the TMDC's with WTe_2 [Qian et al., 2014]. The latter family is composed of materials with a large gap such as MoS_2 , MoSe_2 , WS_2 and WSe_2 but are also predicted to have a topological phase transition from QSH to trivial phase by using an electrostatic gate [Das et al., 2020]. Furthermore, they offer more perspectives for applications due to their topological band structure. WTe_2 in monolayer was confirmed to be a QSH insulator [Tang et al., 2017] [Fei et al., 2017]. It has been observed that the QSHE survives up to 100 K [Wu et al., 2018]. Furthermore, as shown in figure 1.8, by tuning its carrier density, this system evolves to a superconducting phase, which is a very promising way to study superconductivity in proximity with topological materials [Fatemi et al., 2018][Sajadi et al., 2018]. Studies of WTe_2 monolayers are not straightforward, since they must be encapsulated in order to avoid surface oxidation, and the QSH state was evidenced by a couple of teams only.

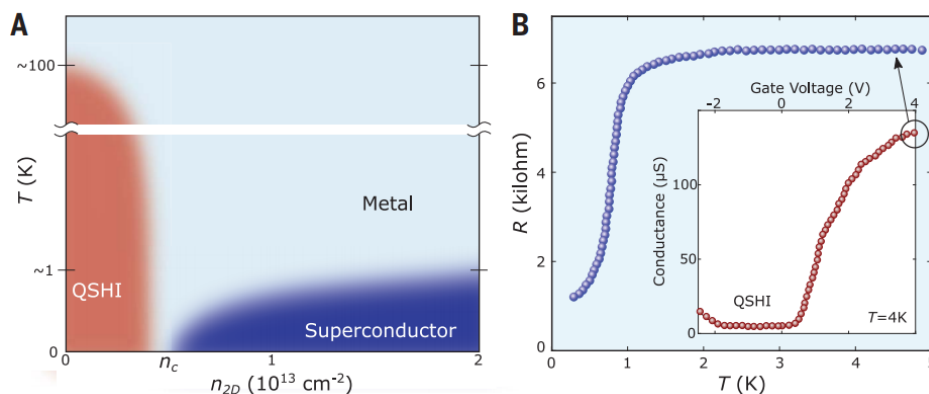


FIGURE 1.8: a) Phase diagram of WTe_2 monolayer as a function of the 2D carrier density, b) Superconducting transition of a WTe_2 monolayer with inset showing the gate-dependent conductance where the observed plateau correspond to the quantum spin Hall state. The arrow show at which gate voltage the transition curve was recorded. Adapted from [Fatemi et al., 2018]

1.2.3 3D \mathbb{Z}_2 Topological Insulator

The works made in the theory and experiment sides on the 2D TI was shortly followed by the generalization of the concept to 3D TIs [Fu et al., 2007]. The first compound identified as a 3D TI was the semiconductor $\text{Bi}_x\text{Sn}_{1-x}$ [Hsieh et al., 2008]. The inversion of the conduction band and the valence band leads to the appearance of surface states at the interface between the 3D TI and a trivial insulator (like the vacuum). Such surfaces states were first measured and characterized by angle resolved emission spectroscopy (ARPES) [Hsieh et al., 2009] [Xia et al., 2009]. With this technique, the surface electronic structure was probed and the presence of the Dirac cone with linear dispersion was clearly evidenced.

Later on, Bi_2Se_3 was investigated and identified as a strong 3D TI [Zhang et al., 2009] [Hsieh et al., 2009][Xia et al., 2009] and it gained a lot of interest. Indeed, due to the stoichiometric composition, this compound could be grown with a much better quality than that of an alloy. Importantly, the band structure of Bi_2Se_3 is an archetype of the band structure of 3D TI surface states with only one single helical Dirac cone located at the middle of the Brillouin zone. Furthermore, the rather large band gap of this family of compounds (Bi_2Se_3 , Bi_2Te_3 , Sb_2Te_3), 300 meV for Bi_2Se_3 and around 170 meV for Bi_2Te_3 , increased greatly their potential for application at room temperature.

Unfortunately in the compound Bi_2Se_3 , the large density of selenium vacancies intrinsically gives a strong electron doping. This shifts the Fermi level energy far in the conduction band and it remains challenging to tune it close to the Dirac point even in ultra-thin layers. More generally, all binary compounds are intrinsically degenerate semiconductors, which makes the investigation of the transport properties of the topological surface states very challenging since the transport properties are usually dominated by bulk properties. In the case of Bi_2Te_3 , the top of the valence band is above the Dirac point, preventing the study of the transport properties related to the topological surface states of low energy. Bi_2Te_3 and Sb_2Te_3 possess a finite bulk conductivity like Bi_2Se_3 , but they have different types of defects (vacancies, antisites), acting as donors or acceptors.

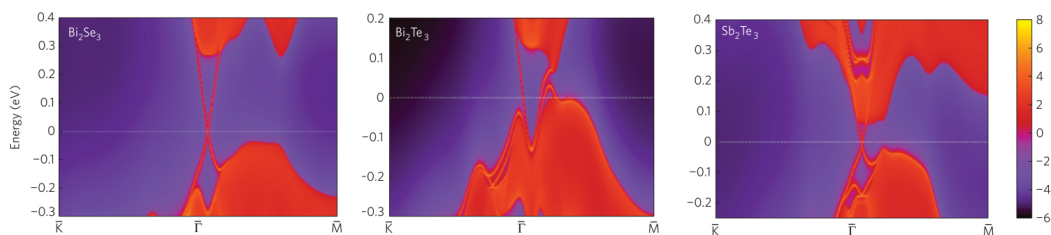


FIGURE 1.9: Band structures from left to right of: Bi_2Se_3 , Bi_2Te_3 , Sb_2Te_3 . Adapted from [Zhang et al., 2009]

Worldwide, several teams have studied ternary or even quaternary compounds of this family, some of which showing some charge compensation. By band structure engineering, they tried to keep a large band gap while reducing the number of carriers. In $(\text{Bi}_{1-x}\text{Sb}_x)_2\text{Te}_3$, the possibility was shown to tune the Fermi energy below (above) the bulk conduction (valence) band edge by controlling the ratio of Bi and Sb. Then by dielectric effect, quantum Hall plateaus were observed for $x = 0.84$ and $x = 0.88$ in the study made by [Yoshimi et al., 2015]. This study proved the feasibility of charge compensation in ternary and quaternary topological insulators.

Importantly, introducing magnetism (or superconductivity) in a 3D topological insulator can induce a non-trivial gap in the 2D surface-state band structure, which leads to the emergence of new quantum phases, such as the QAH discussed in the next chapter. The QAHE was indeed evidenced in diluted magnetic 3D TIs, such as V-doped BST, although the magnetic gap remains rather small (dilution) and intrinsic magnetic disorder limits the operating temperatures [Chang et al., 2013] [Chang et al., 2015] [Grauer et al., 2015] [Peixoto et al., 2016]. More recently, a different strategy was followed, by considering proximity effects in TI/magnet heterostructures in thin films (as shown in figure 1.10) or intrinsic magnetism in Van der Waals-coupled 2D ferromagnets (such as MnBi_2Te_4) [Li et al., 2019a] [Otrokov et al., 2019] [Tan et al., 2020].

As discussed in the next chapter, this research on the QAHE in 2D materials has some connection with 3D Weyl semimetals, another topological phase recently discovered, with spin-chiral Weyl quasiparticles that act as source or sink of Berry curvature.

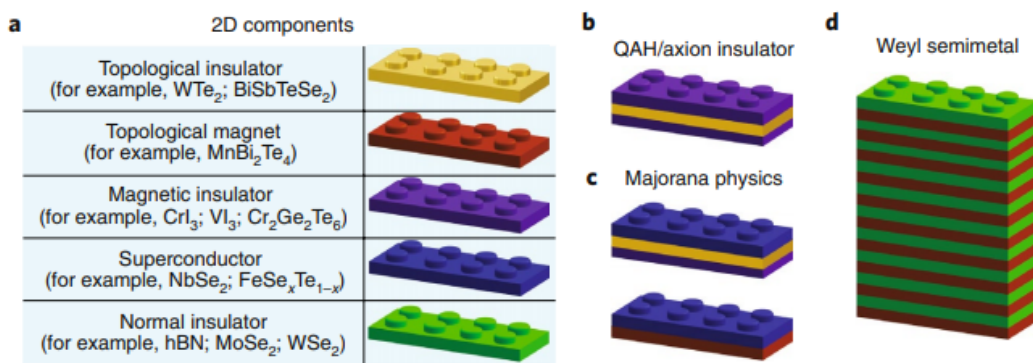


FIGURE 1.10: a, Individual 2D components that can be employed to construct the topological magnet-based heterostructures and superlattices. b, QAH/axion insulator phase in magnetic insulator/TI/magnetic insulator sandwiches. c, Majorana physics in superconductor/TI/magnetic insulator and superconductor/topological magnet heterostructures. d, Weyl semimetal phase in topological magnet/normal insulator superlattices. Adapted from [Chang, 2020]

Chapter 2

TOPOLOGICAL SEMIMETALS

Following the discovery of topological insulators, the last decade has seen a large increase of studies focusing on the topologically non-trivial states of electronic bands. As discussed in the previous chapter, these topological properties are linked to the spectral gap. However, a recent important development in this field has been the theoretical prediction of a topological invariant describing the Fermi surface and the observation of gapless metallic and semimetallic phases that are topologically non-trivial [Matsuura et al., 2013].

This discovery has led the scientific community to predict and observe Dirac and Weyl semimetals, materials for which the low quasiparticle excitation spectra resemble that of the Dirac and Weyl fermions in high-energy physics and that have yet never been observed in this field. These topological semimetals allow us to study important concepts of high-energy physics in condensed-matter systems such as massless fermions breaking parity symmetry, but they are also of interest for potential applications. As explain later in this chapter, Weyl semimetals fermions possess a spin chirality and it is possible to break the conservation law leading to a dominant chirality [Adler, 1969] [Bell and Jackiw, 1969] . In that way, Weyl semimetals can be used as chirality filters in chiraltronics [Grushin and Bardarson, 2017]. Another proposal made by [Hills et al., 2017] was to use a multiple-layer Weyl structure as a medium whose refractive index is negative, so as to focus diverging electrons beams on an extremely small area. This medium could be used in STM measurements to replace the tip, increasing the spatial resolution. Due to the rich variety of crystalline and magnetic structures, topological semimetals are a new platform to discover novel properties related to their band structure, such as the specific electromagnetic response in non-magnetic Weyl semimetals (chiral anomaly) [Zyuzin and Burkov, 2012] or the large anomalous Hall effect in magnetic Weyl semimetals [Burkov, 2014].

In order to introduce this new concept, a simple toy model based on a stack of thin 3D TIs to build a Weyl semimetal phase is reviewed [Burkov, 2015]. In a second

part, the properties of Weyl semimetals are described and some emphasis is put on WTe_2 in the last part. After giving an overview of the state-of-the-art studies, the motivations for this thesis are discussed.

2.1 Construction of Dirac and Weyl Semimetals

The discovery of graphene at the beginning of the 21st century led the scientific community and industries to realize the potential of 2D materials for application in electronics. It followed a strong interest for searching a material that could have the properties of graphene but in three dimensions. For the realization of such properties, a strong spin orbit coupling is required but generally, accidental degeneracies, which can happen in the band structures can be lifted by perturbations. When time reversal symmetry (TRS) and inversion symmetry (IS) holds, some fourfold degenerated band crossing can be protected by the symmetry, leading to the formation of a Dirac semimetals [Armitage et al., 2018]. The band structure is linear close to the Dirac point. In such cases, the system can be described by the Dirac equation formulated in 1928 [Dirac, 1928]. When either the time reversal symmetry or the inversion symmetry is broken, two fold degenerate points which are protected by the topology can emerge in the band structure. A derivation of the Dirac equation by Weyl in the following year described a new kind of fermions that are therefore called Weyl semimetals [Bradlyn et al., 2016]. As shown in figure 2.2, a Dirac semimetal has at least one Dirac cone in its bulk band structure. In the case of a Weyl semimetal, the band structure has at least two pairs of Weyl cones with opposite chiral spin textures, and a topological charge is associated to each node, which describes its spin chirality. As detailed later, these Weyl cones can be tilted and for a strong tilt, a new type of Weyl semimetals with specific properties takes place. Such a new phase is called a type II Weyl semimetal [Soluyanov et al., 2015]. This new phase can appear as an intermediate state between two insulating phases of different topology.

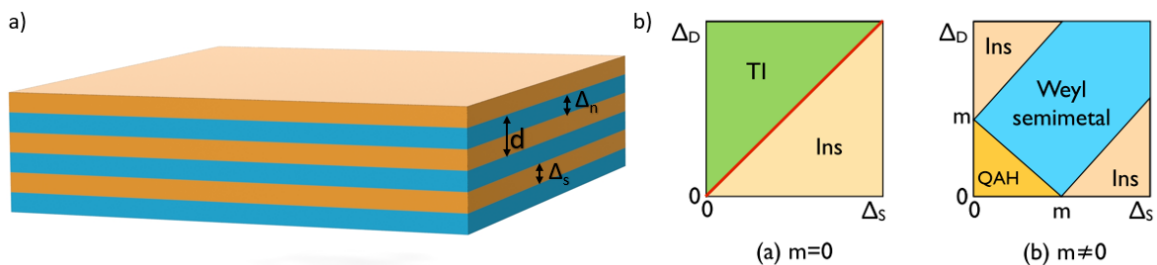


FIGURE 2.1: a) Representation of an heterostructure made of topological insulator layers intercalated with normal insulator layers; b) Phase diagram of the heterostructure for a spin splitting $m = 0$ and $m \neq 0$. Adapted from [Burkov and Balents, 2011]

Construction of a Dirac semimetal

We first recall a simple model to obtain a Weyl semimetal from a stack of a strong 3D TI [Burkov and Balents, 2011]. More specifically, a heterostructure made of topological insulator layers separated by normal insulator layers (NI) can be considered as shown in figure 2.1 . This gives a one dimensionnal stack of 2D gapless states at each interface TI/NI. These interface states are coupled together by tunneling and two different matrix elements can be defined in the Hamiltonian, Δ_S for tunnelling within a TI slab and Δ_N for tunneling through a normal insulator spacer.

Depending on the ratio $\frac{\Delta_S}{\Delta_N}$, this system can be described as either a 3D TI or a normal insulator. By computing the index \mathbb{Z}_2 by the method of Fu and Kane[Fu and Kane, 2007], Burkov and Balents have demonstrated that for $\Delta_S < \Delta_N$, the heterostructure is a strong 3D TI while for $\Delta_S > \Delta_N$, this is a normal insulator, which are rather intuitive results in the limits ($\Delta_S \ll \Delta_N$) and ($\Delta_S \gg \Delta_N$) indeed. Now considering the transition point $\Delta_S = \Delta_N$, the gap closes and the heterostructures becomes a Dirac semimetal if TRS and IS are not broken. The band crossing is 4-fold degenerate but the Dirac cone is not stable resulting in a gap opening. For a Dirac semimetal, it is however possible to obtain a stable metallic phase by adding another spatial symmetry, so as to separate Dirac nodes in momentum space. A possible way is to involve some uniaxial rotation symmetry, like in Cd_3As_2 [Wang et al., 2013], or to consider non-symmorphic space groups[Young et al., 2012].

Construction of a Weyl semimetal

Any deviation from $\Delta_S = \Delta_N$ leads to the annihilation of the Dirac node. To produce a topologically stable phase with 3D Dirac or Weyl nodes, the nodes have to be separated in momentum space. As already mentionned, either the TRS or the IS must be broken in order to have a Weyl topological semimetal and we consider now the case of TI layers doped with magnetic impurities (time reversal symmetry breaking)[Burkov and Balents, 2011]. These magnetic impurities induce a spin splitting of the surface states of magnitude m . Two important values of m define the finite region of the phase diagram of this system (figure 2.1 b)) : $m_{c1}^2 = (\Delta_S - \Delta_N)^2$ and $m_{c2}^2 = (\Delta_S + \Delta_N)^2$. For a small spin splitting $m < m_{c1}$, the system is a stack of QAH insulators uncoupled to each other. Increasing the magnitude of the spin splitting, the coupling between magnetically doped TI layers increases and the system becomes gapless with the apparition of a Dirac cone for $m = m_{c1}$. For $m > m_{c1}$, this Dirac cone splits into two Weyl nodes with opposite chiralities. When the time reversal symmetry is broken and the inversion symmetry is present, there is only one pair of Weyl nodes, at $+k$ and $-k$, having an opposite spin chirality. This

splitting increases while the magnitude of m increases. At a magnitude of m_{c2} , the two Weyl nodes reach the edges of the BZ and annihilate, which bring the system into an insulating phase.

If the inversion symmetry is broken as in WTe_2 for instance, the TRS converts a Weyl node at $+k$ into an associated Weyl node with same chirality at $-k$. Since the net chirality must vanish, another pair of Weyl nodes exist with opposite chiralities leading to a total number of Weyl nodes of four. More complicated models were done for the case of a Weyl semimetal breaking the inversion symmetry [Murakami and Kuga, 2008] [Halász and Balents, 2012] [Murakami et al., 2017]. In all cases, Weyl nodes are topologically stable and cannot be removed without pair annihilation. The chirality or equivalently, the topological charge of a Weyl node can be understood as a source or sink of the Berry flux, named magnetic monopole or antimonopole depending on the chirality [Jia et al., 2016]. Two Weyl nodes of different chirality are connected to each other by Fermi arcs that appear at the surface of the materials and have a \mathbb{Z}_2 invariant that ensures the topological protection. The next section will describe the properties related to these two specificities of Weyl semimetals.

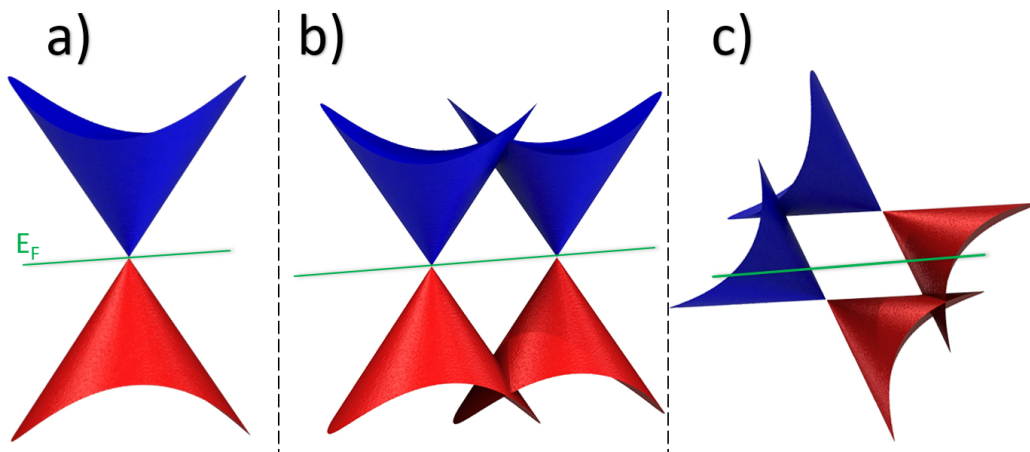


FIGURE 2.2: Schematic of different band structure in topological semimetal, from left to right : Dirac Semimetal, Weyl type I and type II semimetal

Type I and type II Weyl Semimetal

By generalizing the Dirac equation, it was shown [Soluyanov et al., 2015] that Weyl nodes can be tilted such that at a given energy, above or below the Weyl node, the Fermi energy intersects both the electron and valence bands, so that the Fermi surface is constituted by electron and hole pockets that touch each other at the Weyl nodes (figure 2.2).

Considering the most general k -linear Hamiltonian of a Weyl node :

$$H(k) = v \cdot k + \sum_{i,j}^3 k_i A_{ij} \sigma_j \quad (2.1)$$

where A is a 3×3 matrix and σ 's are the Pauli matrices. The Fermi surface for the chemical potential μ can be obtained by solving the equations $\epsilon_{\pm} = \mu$, where

$$\epsilon_{\pm} = v \cdot k + \sqrt{\sum_{i,j} k_i [AA^T]_{ij} k_j} = T(k) + U(k) \quad (2.2)$$

are the two eigenvalues of the Hamiltonian. $T(k)$ and $U(k)$ can be seen as the kinetic and potential components of the energy spectrum. By squaring equation 2.2, the Fermi surface can be described by the quadratic equation :

$$\sum_{i,j} k_i ([AA^T]_{ij} - v_i v_j) k_j + 2\mu v \cdot k - \mu^2 = 0 \quad (2.3)$$

Applying the classification of all possible quadric surfaces [Maxwell et al., 1953] to equation 2.3, it was reported that there are only two possible types of Weyl points for a Fermi energy at the Weyl node [Soluyanov et al., 2015]: type-I has a point-like Fermi surface, and type-II has an open Fermi surface with a zero-gap electron and valence bands structure. The latter results from the tilt of Weyl cones, as induced by the linear term in momentum $T(k)$ which breaks the Lorentz invariance of Weyl fermions in quantum field theory. This was previously considered unimportant before the work of Soluyanov lead to a refined classification of distinct Fermi surfaces. The tilt of the Weyl cone leads to specific transport properties such as a chiral anomaly associated with a transport response that depends on the direction of the electric field, a modified anomalous Hall effect, and new quantum oscillations due to momentum Klein tunneling [Soluyanov et al., 2015] [Menon and Basu, 2020] [O'Brien et al., 2016].

2.2 Transport properties of Topological Semimetals

This part reviews the specific transport properties of quasiparticles in Weyl semimetals. First, the identification of their topological nature is introduced. Second, their bulk transport properties are reviewed, considering two aspects of the band structure:

- the spin-chiral texture of Weyl quasiparticles;
- the partial electron-hole charge compensation.

2.2.1 Discovery and Fermi arcs

The initial attempts to search for Weyl materials were based on the fine tuning of alloys composition or on the magnetic ordering to break TRS [Wan et al., 2011][Bulmash et al., 2014]. In 2015, the prediction of TaAs as a Weyl semimetal due to the lack of inversion symmetry[Huang et al., 2015a] was soon followed by the experimental observation of the specific Weyl band structure [Lv et al., 2015][Weng et al., 2015][Xu et al., 2015].

As for the 3D topological insulators, ARPES was an important tool to unveil the Fermi arcs that appear at the surface of Weyl semimetals as seen in figure 2.3. These Fermi arcs have a crescent shape of two curves that meet at their end points. These end points coincide with the projection of the Weyl nodes on the surface and they are connected by two chiral edge states appearing on the surface band structure. Apart from topological surface states, Weyl semimetals also have specific bulk quasiparticles, which can result in a large transverse or longitudinal magneto-resistance.

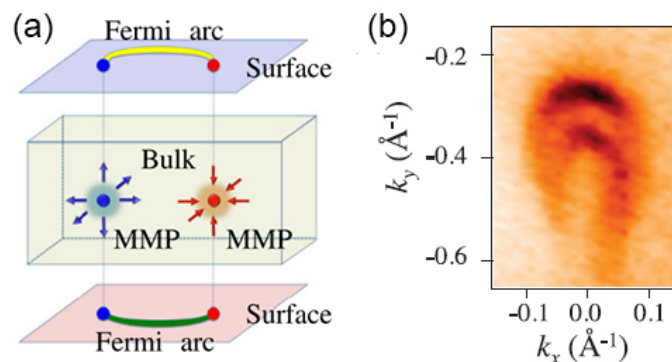


FIGURE 2.3: a) Representation of a Weyl semimetal with Fermi arcs on its surface connecting projections of two Weyl nodes with opposite chirality. A Weyl node behaves as a magnetic monopole (MMP) in momentum space and its chirality corresponds to the charge of the MMP [Lv et al., 2015]; b) ARPES Fermi surface map of the crescent Fermi arcs measured with incident photon energy of 90 eV. Adapted from [Xu et al., 2015]

2.2.2 Anomalous Hall Effect

Another manifestation of the non trivial topology of the band structure of magnetic Weyl semimetals, of interest for spintronics devices, is the very large intrinsic Anomalous Hall Effect (AHE), induced by the maximized Berry curvature. This effect requires both magnetic polarization and spin orbit coupling and leads to a transverse voltage without any external magnetic field, contrary to the standard Hall effect. In magnetic Weyl semimetals, the intrinsic contribution to the anomalous Hall effect is directly related to the separation of the two Weyl nodes and the anomalous

Hall conductivity is given by [Armitage et al., 2018]:

$$\sigma_{xy} = \frac{e^2}{\pi h} k_0 \quad (2.4)$$

where k_0 depends on the magnetization of the material and is related to the distance q separating the two Weyl nodes to the center of the Brillouin Zone in momentum space by the expression :

$$q = \pi/d \pm k_0 \quad (2.5)$$

$$k_0 = \frac{1}{d} \arccos \left(\frac{\Delta_S^2 + \Delta_N^2 - m^2}{2\Delta_S\Delta_N} \right) \quad (2.6)$$

Δ_S , Δ_N , d and m being the parameters related to the toy model for a Weyl semimetal with time reversal invariant described above in the section 2.1. Some prediction has been made that a strong AHE could appear in a non collinear antiferromagnetic Weyl semimetal [Burkov, 2014]. Antiferromagnets offer many advantages compared to ferromagnets [Sürgers, 2018]. They do not have stray magnetic fields, could reduce the switching currents and improve a lot the speed due to faster spin dynamics related to their shorter spin-lattice relaxation time compare to ferromagnets. As an example shown in figure 2.4, Mn_3Ge is a non-collinear Weyl antiferromagnet [Kiyohara et al., 2016] where an anomalous Hall conductivity was measured with $\sigma_{xz} = 80 \Omega^{-1}\text{cm}^{-1}$ at room temperature and $380 \Omega^{-1}\text{cm}^{-1}$ at 5 K.

Considering the case of a ferromagnetic Weyl semimetal, a giant AHE was indeed reported for a large magnetization in Heusler compounds [Liu et al., 2018].

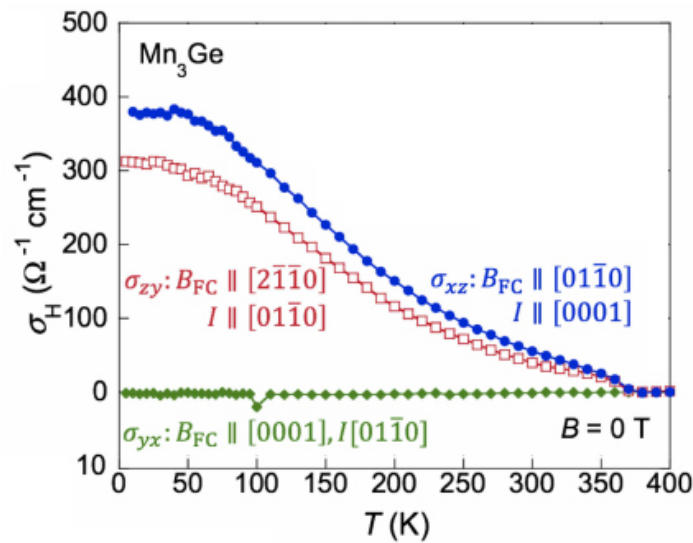


FIGURE 2.4: Temperature dependence of the anomalous Hall effect under zero field in Mn_3Ge after field-cooling in a magnetic field $B_{FC} = 7$ T from 400 K down to 5 K. Adapted from [Kiyohara et al., 2016]

In $\text{Co}_3\text{Sn}_2\text{S}_2$, the anomalous Hall conductivity reaches $1130 \Omega^{-1}\text{cm}^{-1}$. An important parameter to consider is the anomalous Hall angle, which is the ratio of the anomalous Hall conductivity to the longitudinal conductivity. In the case of $\text{Co}_3\text{Sn}_2\text{S}_2$, the anomalous Hall angle reaches up to 20% at 100 K with an anomalous Hall conductivity around $1000 \Omega^{-1}\text{cm}^{-1}$.

As shown on the figure 2.5, Mn_3Ge shows the strongest anomalous Hall conductivity for an antiferromagnet. Similarly, for ferromagnetic materials, $\text{Co}_3\text{Sn}_2\text{S}_2$ has the largest anomalous Hall angle ever measured. This point out that ferromagnetic and antiferromagnetic Weyl semimetals could be important for applications if their robust properties can be evidenced above room temperature. In all cases, these large responses are a direct signature of the dominant intrinsic contribution to the AHE and the maximized Berry curvature of Weyl quasiparticles.

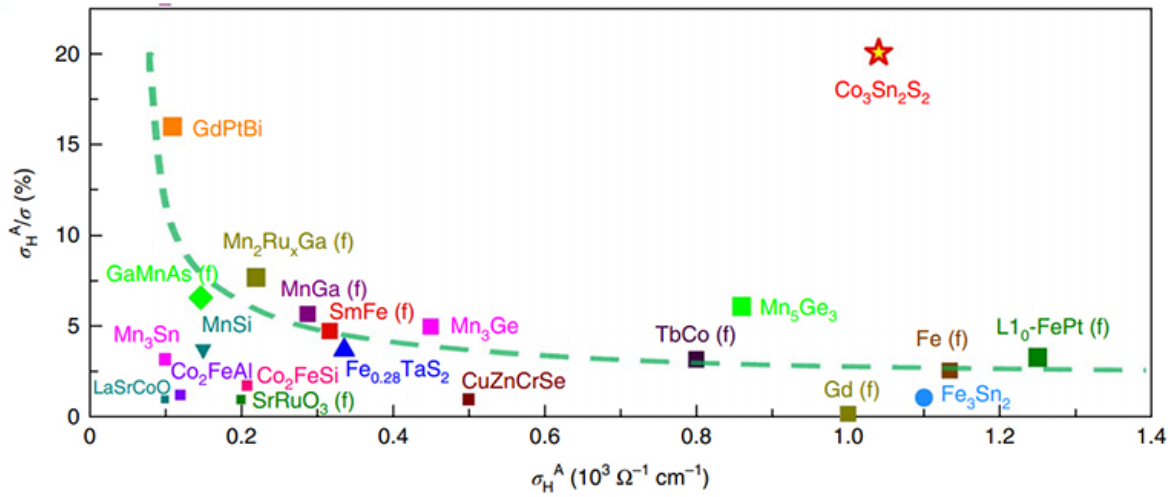


FIGURE 2.5: Comparison of the anomalous Hall angle as a function of the anomalous Hall conductivity in different materials, (f) is for measurements made on thin-film materials. The dashed line is a guide to the eye. Adapted from [Liu et al., 2018]

2.2.3 Extremely Large Magnetoresistance

In some non-magnetic Weyl semimetals, the longitudinal resistance can be strongly modified by a perpendicular magnetic field, and an extremely large MR was reported, as found for NbP [Shekhar et al., 2015] (see figure 2.6). For this material, the perpendicular MR can reach up to 1 million percent at $B = 30$ T and at very low temperature without any indication of saturation. The origin of this extremely large magnetoresistance is the electron-hole compensation also observed in other Weyl semimetals including WTe_2 [Ali et al., 2014] [Shekhar et al., 2015] [Gao et al., 2017].

The simplest way to describe the magnetoresistance of a charge compensated semimetal is to consider first a single electron band and a single hole band. The

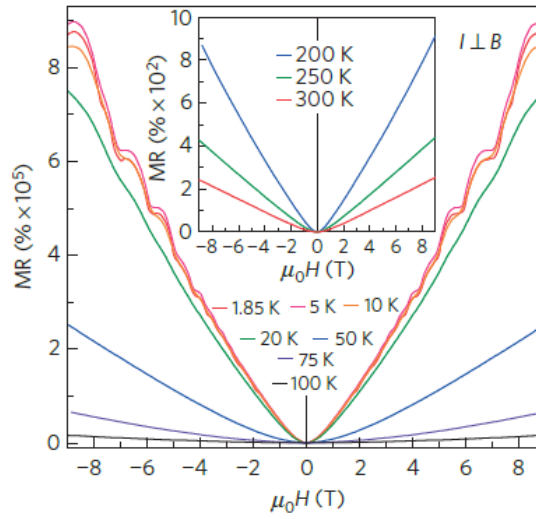


FIGURE 2.6: Perpendicular magnetoresistance of NbP measured at different temperatures up to 9 T. The inset shows the magnetoresistance at higher temperatures. Adapted from [Shekhar et al., 2015].

following equations describe the magnetoresistance for this 2-band model [Chambers, 1990] :

$$\begin{aligned} \rho_{xx} &= \frac{1}{e} \frac{(n_e \mu_e + n_h \mu_h) + (n_e \mu_e \mu_h^2 + n_h \mu_h \mu_e^2) B^2}{(n_e \mu_e + n_h \mu_h)^2 + \mu_e^2 \mu_h^2 (n_h - n_e)^2 B^2} \\ \rho_{xy} &= \frac{B}{e} \frac{(n_h \mu_h^2 - n_e \mu_e^2) + \mu_e^2 \mu_h^2 (n_h - n_e) B^2}{(n_e \mu_e + n_h \mu_h)^2 + \mu_e^2 \mu_h^2 (n_h - n_e)^2 B^2} \end{aligned} \quad (2.7)$$

Considering the case of charge compensation ($n_h = n_e$), equations 2.7 show that the MR is quadratic in B , without saturation, and that the Hall effect becomes linear in B . The amplitude of the longitudinal MR is maximized at the charge compensation, as confirmed by experiments [Fatemi et al., 2017] [Wang et al., 2019]. Nevertheless, experiments also reported some deviation from the quadratic law [Thoutam et al., 2015] [Wang et al., 2016b] [Fatemi et al., 2017] [Wang et al., 2019], which cannot be explained in a simple two-band model. We note that a large magnetoresistance was also reported in topological semimetals that were not at the compensation so that the charge compensation cannot be the unique source of very large magnetoresistance in such materials [Liang et al., 2015].

As discussed in this thesis, to better understand the XMR, it is important to consider the influence of both disorder (mobilities) and multi-band transport (more than two bands). This will be detailed in the study of WTe_2 nanostructures presented in chapter 4. We also note here that, in the complex band structure of Weyl semimetals, Weyl nodes are usually not located at the energy for which the charge compensation is realized.

2.2.4 Chiral Anomaly

Since Weyl cones emerge by pairs of opposite spin chirality, the overall net chirality vanishes. However, if an electromagnetic field is applied with E parallel to B , the number of charge of a given chirality is not conserved anymore contrary to the total charge : Weyl nodes act as source and sink of electrons leading to a valley polarization. This is the so-called chiral anomaly [Nielsen and Ninomiya, 1983] in which the finite electric field creates a non-equilibrium charge flow between pairs of Weyl cones of opposite chirality if it is aligned along the magnetic field. Hence, charges are pumped from one Weyl cone to another leading to different effective chemical potentials as shown in figure 2.7. In a steady state, this charge pumping process is damped by inter-Weyl cone scattering with an inter-cone relaxation time τ_{int} [Son and Spivak, 2013], thus limiting the amplitude of the chiral anomaly.

In this case, a difference in the chemical potential of paired cones will appear leading to a chiral current : $j \propto E \times B \tau_{\text{int}}$. [Zyuzin and Burkov, 2012] [Son and Spivak, 2013] Therefore when a magnetic field is applied along the current in a WSM, this additional chiral current leads to a negative magnetoresistance as observed in TaAs in figure 2.7. An important point to notice is that the chiral charge pumping does not vanish if the current and the magnetic field are misaligned. The observation of the negative MR becomes difficult when the standard positive orbital MR component becomes more important than that related to the chiral anomaly. Therefore, if a negative MR is rapidly becoming positive with the field orientation, this could suggest that it rather originates from another mechanism : the current jetting.

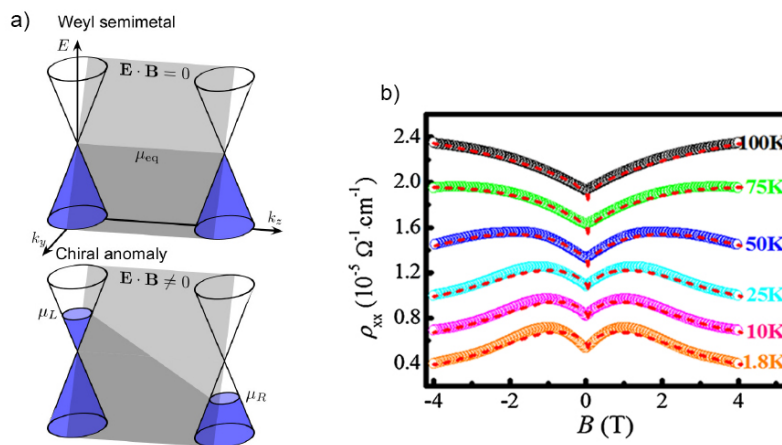


FIGURE 2.7: a) Representation of two Weyl nodes of different chirality separated in momentum space. Applying an electric and magnetic field, parallel to each other, charge carrier are pumped from one cone to the other leading to unbalanced chemical potential $\mu_L \neq \mu_R$. Adapted from [Behrends et al., 2016] ; b) Observation of the negative longitudinal magnetoresistance in TaAs. Adapted from [Huang et al., 2015b].

In that case, materials with a large anisotropic resistance are considered, in which the current flows along the high-conductance direction. If the current is not injected homogeneously (as in point contact measurements or in case of irregular sample shapes), the distribution of the current inside the sample is not homogeneous. The equipotential lines are highly distorted and thus, the current forms jets [Pippard, 1989]. In DSM and WSM and in the case of the search for the chiral anomaly, this effect produces an intrinsic conductivity anisotropy which produces inhomogeneous current distributions that distort the longitudinal magnetoresistance profile. This implies that a negative magnetoresistance related to the current jetting can appear in these material for an electric field and magnetic field parallel to each other as shown by two groups [Liang et al., 2018][dos Reis et al., 2016].

In type II WSM, given the strongly tilted Weyl cones, two cases have to be considered [Sharma et al., 2017]. The chiral anomaly becomes anisotropic in the quantum limit, where $\tau\omega_c \gg 1$, with τ the transport relaxation time and ω_c the cyclotron frequency. In the classical limit, the negative longitudinal magnetoresistance becomes isotropic similar to type I Weyl semimetals. This property is discussed in the next chapter, focusing on the anisotropic chiral anomaly in WTe_2 .

2.3 WTe_2 : a type II Weyl semimetal

WTe_2 is a transition metal dichalcogenide (TMDC). It belongs to a family of layered materials MX_2 (with $M = W$ or Mo , $X = S, Se, Te$). Like $MoTe_2$, WTe_2 is predicted to be a non-centrosymmetric Weyl semimetal of type II with 8 Weyl nodes [Soluyanov et al., 2015]. Pairs of tilted Weyl cones are located slightly above the Fermi level energy, with nodes at 52 and 58 meV, all four pairs being related to each other by crystal symmetries. Due to the small Van der Waals interaction between the layers, this material can be exfoliated. In this section, the band structure of WTe_2 is first described, in connection to the observation of an extremely large magnetoresistance. Then the signatures reported so far of a type II Weyl semimetal in transport measurements are reviewed.

2.3.1 Band structure

As revealed by ARPES measurements at room temperature [Pletikosić et al., 2014] [Jiang et al., 2015] [Das et al., 2019], WTe_2 has large electron pockets in the Brillouin zone. Upon cooldown, a Lifshitz transition, which corresponds to a change of the Fermi surface topology, is observed at $T \approx 150$ K without any structural transition [Wu et al., 2015]. This transition is caused by a shift of the chemical potential

that leads to the appearance of hole pockets below this temperature. Between 150 K and 70 K, the size of these electron pockets is reduced and that of hole pockets grows. At lower temperature, the magnetoresistance varies as a power-law of the applied magnetic field, with the so-called Kohler's exponent very close to two (quadratic behavior) [Zhao et al., 2015]. This indicates that the extremely large magnetoresistance is not due to a metal-insulator transition but rather to some charge compensation mechanism. The Kohler's scaling breaks between 70 and 140 K which is coherent with the fact that electrons dominate at higher temperatures.

From a structural point of view, the band structure change that takes place at about $T \approx 150$ K is related to the reduction of the crystal lattice parameter upon cooldown. As a consequence, it was shown by density functional theory calculations that Weyl nodes appear below around 70 K and, for a given pair, the distance between Weyl nodes of opposite chirality in momentum space increases as the temperature is lowered [Lv et al., 2017]. At lower temperatures (below about 50 K), a significant reduction of the electron pockets occurs which leads to a nearly perfect compensation between electron and hole pockets, as reported in transport measurement studies [Ali et al., 2014] [Luo et al., 2015].

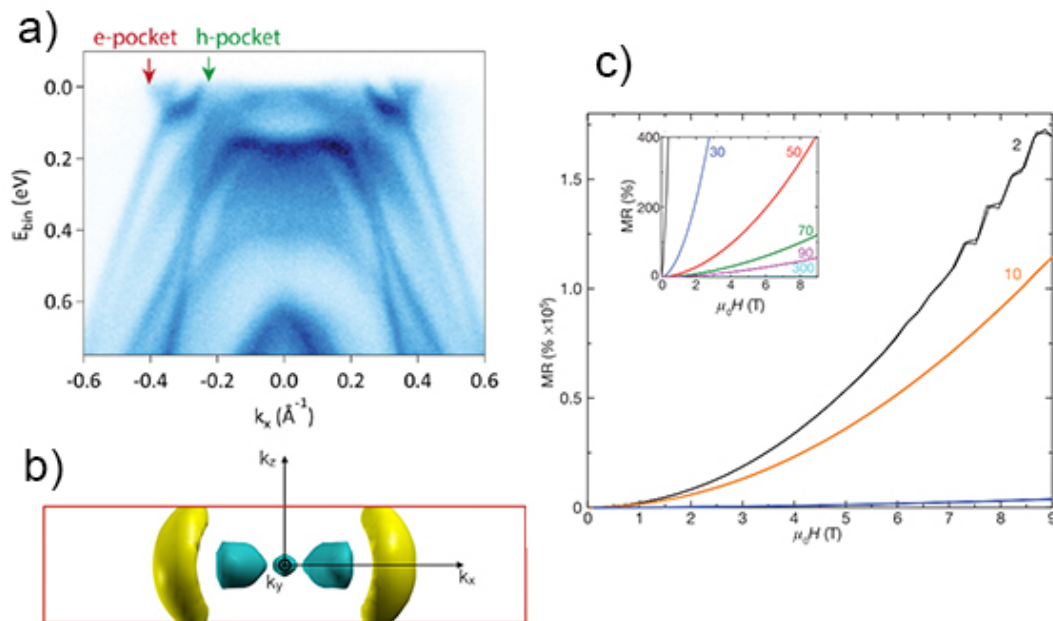


FIGURE 2.8: a) Band dispersion of WTe_2 along the X- Γ -X direction which is the direction of Te-W-Te chains measured by high resolution ARPES. At both sides of the Brillouin zone, electrons and holes pockets are observed as point out by the arrows. Adapted from [Das et al., 2019] b) Simulated Fermi surface of WTe_2 showing the electron (yellow) and hole (blue) pockets along X- Γ -X. Adapted from [Ali et al., 2014] c) XMR with the current along the a-axis (W-W chains) as a function of the magnetic field along the c-axis of the WTe_2 structure at different temperature. Adapted from [Ali et al., 2014].

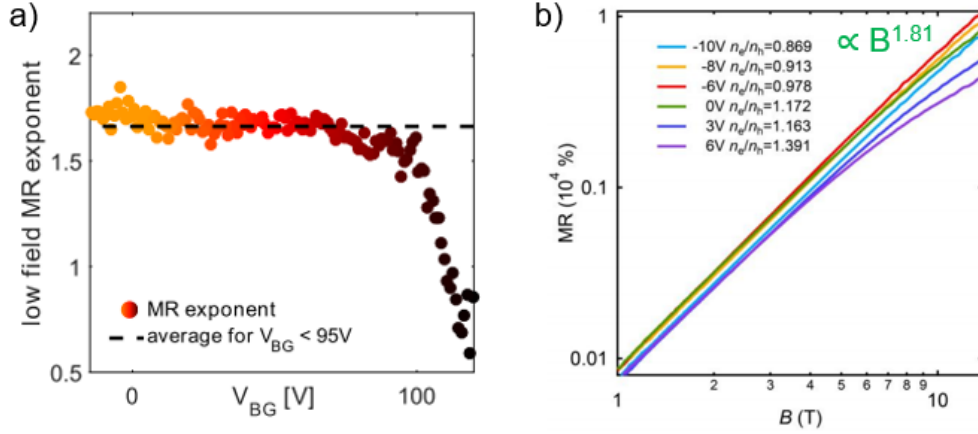


FIGURE 2.9: a) The fitted exponent of the MR power law for B in the range of [0.4, 1.5] T as a function of gate voltage. The limits were chosen to avoid the high relative noise at low fields ($B < 0.2$ T) and onset of saturation at high field. Adapted from [Fatemi et al., 2017]. b) MR versus B with log-log plot at different gate voltages. Adapted from Supplementary [Wang et al., 2019]

As a consequence, like other Weyl semimetals, WTe_2 shows an anisotropic and extremely large magnetoresistance (for a magnetic field applied along the out-of-plane direction) which is explained by the electron-hole compensation [Ali et al., 2014] [Luo et al., 2015]. Although WTe_2 has two independent pairs of electrons pockets and two independent pairs of holes pockets, the two-band model already mentioned in Sec. 2.2.3 is a reasonable approximation to describe the system at first. For a perpendicular induction of 9 T, the maximum magnetoresistance reported in this material is as high as 175 000 % at 2 K [Ali et al., 2014]. However, as already mentioned, the Koehler's exponent is systematically found smaller than two. This subquadratic behavior was reported in several studies without any explanation about its origin [Thoutam et al., 2015] [Wang et al., 2016b] [Fatemi et al., 2017] [Wang et al., 2019]. Using an electric gate, the power law exponent was analysed with respect to the position of the Fermi level energy [Fatemi et al., 2017] [Wang et al., 2019]. It was shown that the subquadratic origin is not coming from a shift of the ratio n_e/n_h as shown in figure 2.9. A detailed study of the subquadratic MR behavior as well as the relation between the nature of the disorder and the MR will be the subject of the chapter 4.

As for the rest of this chapter, we will focus on the different features observed in the WTe_2 magnetoresistance depending on the crystal structure axis along which the electric and magnetic fields are applied. Experimentally, the out-of-plane XMR makes challenging the measurement and observation of other features and some special care regarding the orientation between the crystal and the magnetic field has to be taken.

2.3.2 Indication of Weyl orbits due to the Fermi arcs

WTe₂ was the first material suggested to be a type II Weyl semimetal [Soluyanov et al., 2015]. However, due to the proximity of Weyl nodes of WTe₂ in momentum space, ARPES measurements do not have the resolution to separate them [Wang et al., 2016a].

A study made by [Potter et al., 2014] showed that specific magnetic quantum oscillations should arise due to the Fermi Arcs in thin films of WSM. Considering an electron of momentum k_z moving along the Fermi arcs from a chiral node to another, it can then propagate within the bulk, from one surface to another, via a gapless chiral Landau mode, and reconnect to the initial surface in a similar way (propagation along the opposite surface Fermi arc and through a bulk Landau mode). This defines a loop, as shown in figure 2.10, which is different from conventional closed cyclotron orbits in real space. As for Shubnikov-de Haas oscillations, if a magnetic field is applied, quantum interference leads to the formation of quantized energy levels. For a constructive interference, a Landau level takes place. When a Landau level crosses the Fermi level, a peak occurs in the density of states leading to $1/B$ periodic oscillations as for SdHO related to bulk cyclotron orbits. Such oscillations related to these Fermi arcs based orbitals, called Weyl orbits, can be evidenced by studying the

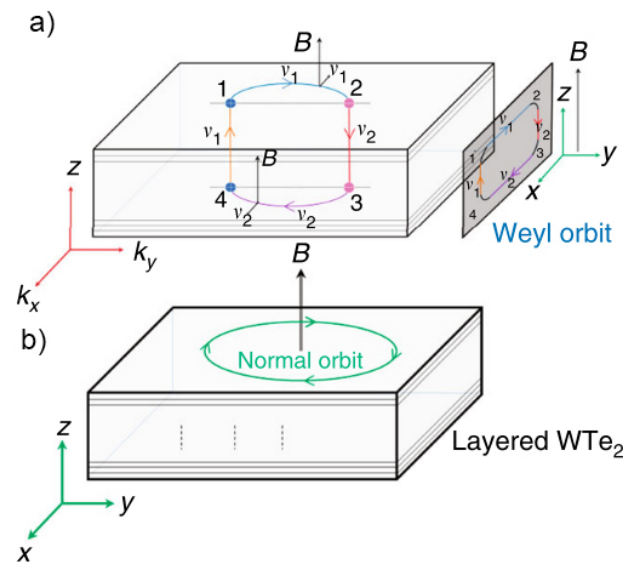


FIGURE 2.10: a) Fermi-arc-induced Weyl orbit in a thin WTe₂ nanoribbon, in which the magnetic field is along the z -axis (or c -) axis. This Weyl orbit is formed by connecting two bulk paths along the z -direction through the zeroth chiral bulk Landau level (LL) and two Fermi arcs in the momentum space, on both the top and bottom surfaces. The trajectory of the Weyl orbit in real space is in the xz plane, and the Weyl orbit is plotted in a combination of real space and momentum space. b) Conventional quantum oscillation orbit. Adapted from [Li et al., 2017b]

variation of the $1/B$ periodic oscillations amplitude while reducing the doping or the size of the system [Potter et al., 2014]. If the Fermi energy is pinned at the Weyl nodes, only oscillations from the Weyl orbit can appear. Upon doping, the surface and the bulk oscillations are both present. In that case, one can roughly compare the ratio of bulk-to-surface oscillations amplitudes to the ratio of bulk to surface density of states.

In the paper of [Li et al., 2017b], the authors claimed to have observed the Weyl orbit in WTe_2 proving hence the existence of Weyl nodes in the material. Indeed, by increasing the thickness, the amplitude of the Weyl orbit oscillations decreases as compared to that of Shubnikov-de Haas oscillations due to an electron pocket.

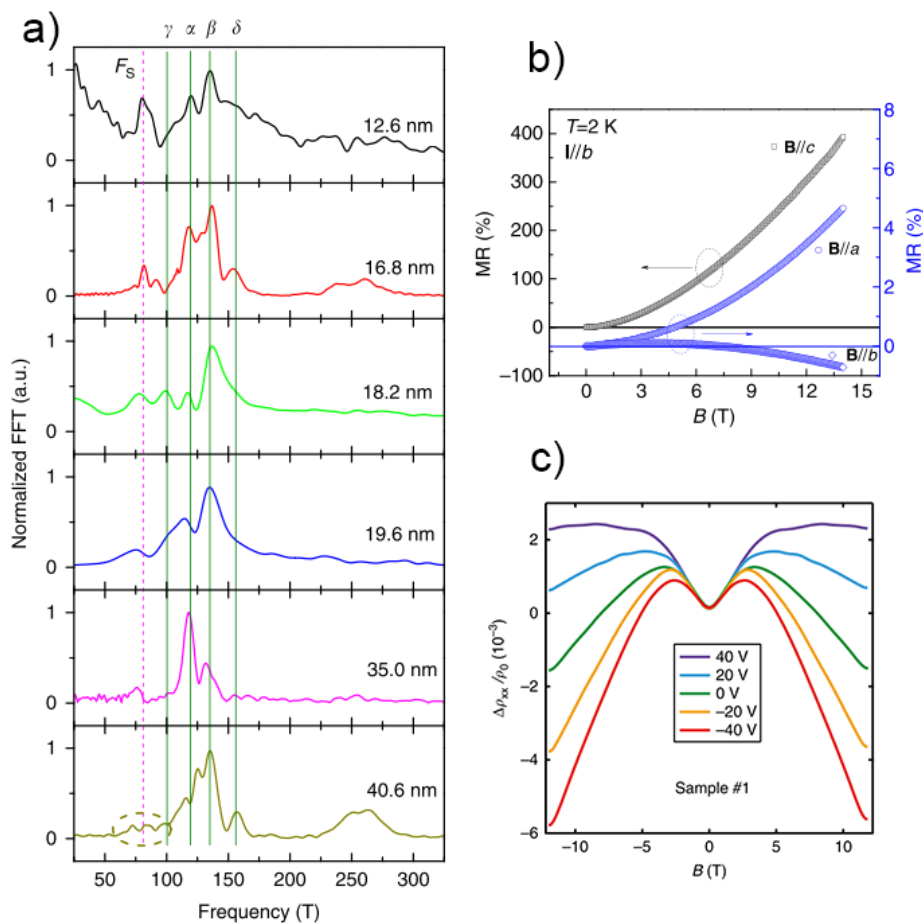


FIGURE 2.11: a) Evolution of the Weyl orbit frequency as a function of the thickness of WTe_2 . Adapted from [Li et al., 2017b] b) MR as a function of the magnetic field B along the different crystalline axis with a current along the b direction. Observation of a negative longitudinal MR when the electric field E and the magnetic field B are parallel to the b -axis. Adapted from [Lv et al., 2017] c) Relative resistance as a function of B while B and E are parallel to the b -axis for different potential on the dielectric gate. This measurement shows the tunability of this effect while the chemical potential is shifted with respect to the Weyl node. Adapted from [Wang et al., 2016a]

authors also reported on the presence of a uniaxial negative longitudinal magnetoresistance NLMR with parallel electric and magnetic fields, oriented along the b-axis. This anisotropy of the chiral anomaly, already reported by [Wang et al., 2016a], has been suggested to be a strong evidence of the type-II nature of these Weyl semimetals.

2.3.3 Type-II nature

In a type I WSM, the chiral anomaly is present in any direction as long as the electric field and the magnetic field are parallel to each other [Zyuzin and Burkov, 2012]. In a type II WSM, the chiral anomaly response is not isotropic anymore so that, in order to see the NLMR, the magnetic field has to be applied in the direction along which the kinetic energy of the fermions is larger than their potential energy [Soluyanov et al., 2015]. Therefore, the magnetic field and the electric field have to be applied along the tilted-cone axis. In WTe_2 , the NLMR was observed up to 30 K when the magnetic and electric field were applied along the b-axis, whereas a positive MR was found when applied along the a axis [Wang et al., 2016a][Li et al., 2017b]. The longitudinal magnetoresistance can be tuned from negative to positive by electrostatic gate effect as shown in figure 2.11 b). A dependence of this effect as a function of the thickness of the sample further revealed that the NLMR disappeared for samples thicker than 40 nm, probably due to a shift of the chemical potential away from the Weyl nodes or due to a change of the band structure. Indeed, a study of the Shubnikov-de Haas oscillations for different sample thicknesses showed that the electron bands are pushed to higher energies while the hole bands are pushed to lower energies, for samples in the range of 40 to 10 nm, as compared to the bulk band structure [Xiang et al., 2018]. For samples thinner than 10 nm, the NLMR disappears. In this case, the possibility that the band crossing vanishes was related to a gradual band gap opening [Li et al., 2017b].

However, it has been predicted and observed that an isotropic NLMR can occur, due to the chiral anomaly in type II Weyl semimetal [Sharma et al., 2017][Lv et al., 2017]. Indeed, two cases have to be considered, depending on the transport regime. The different regimes are defined by the product of the cyclotron frequency ω_c and the relaxation time τ , with either $\omega_c\tau \gg 1$, (quantum regime) [Argyres and Adams, 1956] or $\omega_c\tau \ll 1$ (classical regime). In WTe_2 , it has been found that in the quantum regime, the NLMR induced by the chiral anomaly is only present with the magnetic field along the b axis [Wang et al., 2016a] contrary to the classical regime where this effect does not depend on the magnetic field axis. Indeed, the study of [Lv et al., 2017] revealed an isotropic chiral anomaly in the classical regime with single crystals

of $WTe_{1.98}$ grown by CVT. Yet, the measured sample seems to be in the cross-over regime, $\omega_c \tau = 0.51$.

We remark that an important issue for WTe_2 , overlooked in the literature, is that the Fermi energy is well below the Weyl nodes. The XMR measured for an out-of-plane magnetic field (along the c-axis) is attributed to a charge compensation, a regime that sets the position of the Fermi energy at more than 50 meV below the Weyl nodes. This casts doubts on the exact nature of the NLMR observed and it should discard the mechanism based on the chiral anomaly. In the experiments of Lv et al, the authors claims that Te vacancies act as donors. Hence the shift of the Fermi level towards the Weyl nodes [Lv et al., 2017]. Nevertheless, some questions remain, due to the large perpendicular magnetoresistance observed in this material. On the one hand, the study by Li et al. [Li et al., 2017b] showed an anisotropic negative MR in exfoliated nanostructures, which also exhibit a large XMR, as expected at the compensation for very disordered structures. On the other hand, the studies made by the group of Zhang [Zhang et al., 2017] and the group of Wang [Wang et al., 2016a] with nanostructures grown by CVD or obtained by exfoliation respectively, did not show any high perpendicular magnetoresistance. Despite the fact that no information about the position of the Fermi level energy was given in these works, a large deviation from the charge compensation is very unlikely. Even if a large amount of Te vacancies could be invoked in these studies, the interpretation of the negative MR in terms of the chiral anomaly mechanism remains questionable. Our results clearly contradict this conclusion.

In Chapter 5, we report on an isotropic NLMR in WTe_2 that can be ascribed to a Lifshitz transition at very low temperature as confirmed by numerical simulations. Interestingly, our results can be interpreted in the framework of Weyl physics far from the Weyl nodes.

2.3.4 Planar Hall effect

In 2.3.3, the negative anisotropic MR was discussed in terms of the chiral anomaly. If the anisotropy in the longitudinal resistivity is related to the chiral anomaly, it was predicted that it should induce a finite planar-Hall effect [Nandy et al., 2017].

The planar Hall effect was first observed in ferromagnets, for which the Hall resistance was found to depend on the in-plane magnetic field, being directly related to the anisotropic magneto-resistance [Ky, 1968]. The Hall resistance becomes larger when the current flows parallel to the magnetization vector than when it flows perpendicular to it. In a non-magnetic Weyl system, there is no magnetization vector

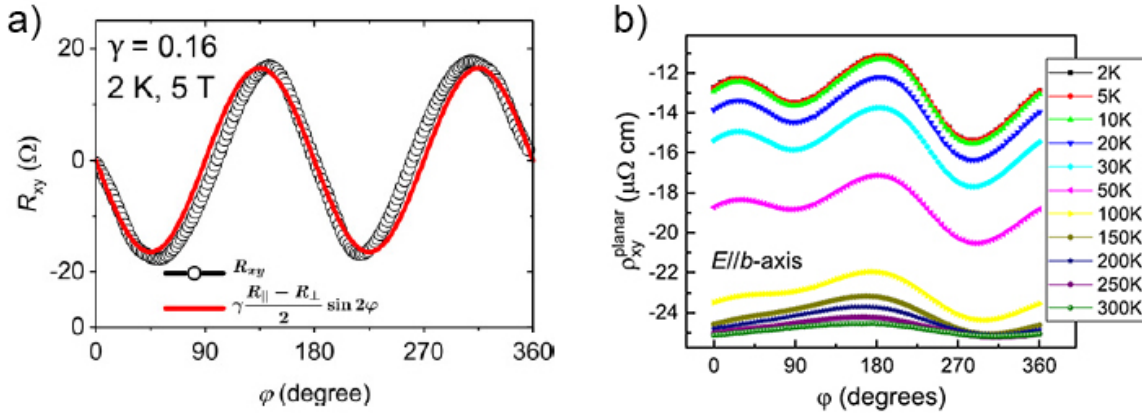


FIGURE 2.12: Comparison of the Planar Hall effect in a) Cd_3As_2 (Dirac semimetal) in a structure of 600 nm (Adapted from [Li et al., 2018]) and in b) WTe_2 with a current in the b -axis direction and a magnetic field of 14 T (Adapted from [Li et al., 2019b]).

and the planar Hall effect is a consequence of the finite Berry curvature and could be related to the chiral anomaly [Nandy et al., 2017] [Li et al., 2019b]. As for the NLMR, this effect is different depending on the type of Weyl semimetal considered. As for MoTe_2 [Liang et al., 2019], studies in WTe_2 have shown that a strong orbital magnetoresistance (OMR) is present in the material, possibly giving some difficulties to clearly evidence the non-trivial origin of the planar Hall effect of this material [Li et al., 2019b]. Another difficulty is related to the very small amplitude of the effect, as compared to other semimetals, as shown for Cd_3As_2 in figure 2.12. Nevertheless, Li et al. claimed to have measured the signature of an anisotropic planar Hall effect that could not be only explained by the OMR effect but could be attributed to the chiral anomaly in type II Weyl semimetal of WTe_2 .

As discussed in this chapter, experimental studies of the low-field magneto-transport properties of WTe_2 nanostructures are rather controversial. In some cases, it remains unclear whether these properties are related to the non-trivial topology of the band structure or not. This calls for a better understanding of charge transport for a Fermi energy close to the compensation regime, taking disorder and the multi-band nature of the band structure into account. In particular, we will show in Chapter 5 that high-energy Weyl quasiparticles (far below the Weyl nodes) contribute to an isotropic negative MR at low field and very low temperature, different from the mechanism related to the chiral anomaly for low-energy Weyl fermions.

CRYSTAL GROWTH AND EXPERIMENTAL TECHNIQUES

A major breakthrough for the investigation of charge transport properties has been the discovery of the liquefaction of ^4He by Kamerling Ohnes in 1908, which gave the possibility to study the groundstate and the low excitation regime of materials at low temperatures. During a cool down to liquid He temperature, the resistivity of metals decreases drastically to very small values. To keep a good signal-to-noise ratio at low temperature, the voltage across the sample needs to be maximized. To this aim, it is possible either to increase the current or to increase the resistance by increasing the geometric aspect ratio (nanofabrication) and/or by reducing the sample thickness. In particular, an important step toward the fabrication of high quality ultra-thin nanostructures was the discovery of graphene by Novoselov and Geim in 2004 and their development of the mechanical exfoliation method, a technique that is now applied to a wide class of Van der Waals materials. In addition to this top-down technique, the bottom-up growth of high-quality thin films and nanostructures has been considerably developed, with different growth methods (Molecular beam epitaxy, chemical vapor deposition, vapor transport, etc.) that allows for some comparative studies of a given material with different carrier densities or mobilities. In this work, two methods were used to obtain WTe_2 nanostructures, either exfoliated from a large single crystal or grown by chemical vapor transport, with point defects only and different degrees of disorder.

In the first section of this chapter, the crystal structure of WTe_2 is briefly described, and the two different methods are presented. In order to obtain thin nanostructures, two strategies were followed. First, a bottom-up approach was achieved by the direct growth of WTe_2 nanosheets on an Yttria-Stabilized-Zirconia (YSZ) substrate. Second a top-down approach consisting in the mechanical exfoliation of a large single crystal obtained by a flux-growth method was realized, and nanostructures were transferred onto a Si/SiO_2 substrate. A comparison of the transport properties of nanostructures obtained by these two different methods is given in Chapter 4. In the

next section, the nanofabrication process is described and the different steps of fabrication for each type of nanostructures are presented. In the last section, the principle of operation of a ^3He - ^4He dilution refrigerator is explained and our measurement setup for low-noise electrical measurements is presented.

3.1 Growth of WTe_2

3.1.1 Crystal structure

WTe_2 is a transition metal dichalcogenide (TMDC), with a 2D base unit MX_2 where M is a transition metal (W, Mo) and X is a chalcogen atom (Te, Se, S). This family of compounds is polytypic and the materials can be crystallized in different structures 1H, 1T, 1T' and 1T_d as shown in figure 3.1 a) [Qian et al., 2014] (1T' and 1T_d are different only in their 3D representation). The most-studied structure up to now is the 1H structure which is a stack of three planes of 2D hexagonally packed atoms, X-M-X in the space group P6m2. In the 1T structure this three planes form a rhombohedral stacking, space group P3m2. The 1T structure for the TMDCs MX_2 is unstable and undergoes a lattice distortion in the x direction leading to the 1T' non-centrosymmetric structure consisting of 1D zigzag chains along the y direction with space group P2m/1. 1T' and 1T_d appear to be different from a stacking point of view,

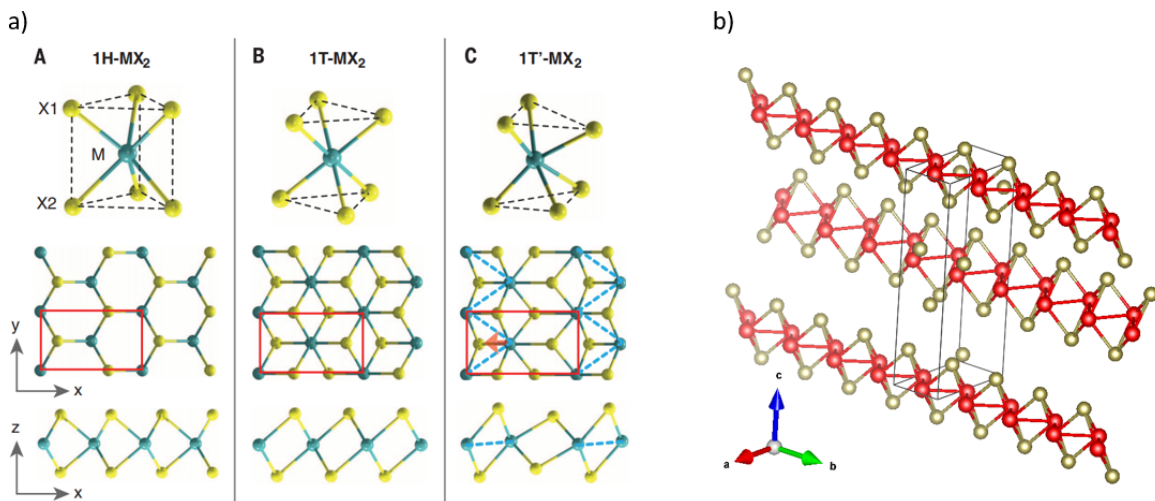


FIGURE 3.1: a) Atomistic structures of transition metal dichalcogenides MX_2 . M stands for (W, Mo) and X stands for (Te, Se, S). (A) 1H- MX_2 with P6m2 space group. (B) 1T- MX_2 with P3m2 space group. (C) 1T'- MX_2 , distorted 1T- MX_2 , where the distorted M atoms form 1D zigzag chains indicated by the dashed blue line. The 2D unit cell is indicated by red rectangles. Adapted from [Qian et al., 2014] b) Non-centrosymmetric crystal structure of WTe_2 (group 31 : Pmn2₁) showing a cross section of the 2D planes, with zigzag chains of W atoms (red) surrounded by Te chalcogen atoms (yellow). Between the two figures, x corresponds to the a-axis, y to the b-axis and z to the c-axis.

$1T'$ being monoclinic while $1T_d$ is orthorhombic with space group $Pmn2_1$. This latter structure is that we have interest in for WTe_2 in this work. For this crystal structure, WTe_2 exhibits type II Weyl nodes that are not present in the other structures.

WTe_2 has a base unit layer made of a plane of W metal atoms with covalent bonds to two surrounding planes of Te chalcogen atoms. This tungsten dichalcogenide unit block stacks with weak Van-der Waals bonds along the c -axis, thus giving the possibility to thin a bulk layered crystal down to the monolayer. The zig-zag distortion of the W - W chains along the a -axis of the orthorhombic unit cell makes the compound structurally one-dimensional and, as explained in subsection 3.1.2, gives a needle-shape to the bulk single crystals.

3.1.2 Chemical Vapor Transport Growth

Growth Principle

Chemical vapour transport (CVT) is a process where a condensed phase also called reactant, undergoes a sublimation process in a high-temperature zone, and then propagates to a lower-temperature area (sometimes in presence of a transport agent) where a deposition process results in the formation of crystals. The set-up consists of a two-zone furnace (source T_2 and sink T_1 , $T_2 > T_1$), the reactant and transport agent being sealed in a quartz ampoule. The various parameters that must be optimized for a successful CVT are the growth temperature, the mass of materials in the source, the choice of the transport agent, the position of the wafer and the growth time. Transport is governed by two processes : convection and diffusion. The optimization of the growth parameter for each chemical system is crucial to get the optimal geometry (size and thickness of the structures) and density of structures.

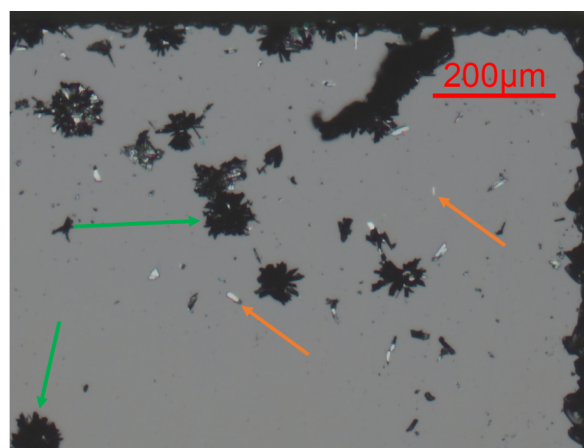


FIGURE 3.2: Optical image of a YSZ substrate after CVT growth showing nanosheets (orange arrows) and clusters (green arrows) of WTe_2 randomly distributed on its surface

Nanostructures of WTe_2 were prepared by Felix Hansen in the group of Silke Hampel at the IFW Dresden. Some results are briefly reviewed below, and more details can be found in [Hansen et al., 2020] or will be published in the PhD thesis of Felix Hansen.

For the chemical vapor transport growth of WTe_2 , all chemicals were purchased from Alfa Aesar (USA) with purities $> 99.9\%$. The tungsten powder was reduced in a hydrogen stream for 24 h before using it, so as to reduce surface oxidation, and then stored in a glovebox under Argon atmosphere. To avoid any contamination and oxidation, all preparation steps are performed in an Argon-atmosphere glove box. The main transport agent is $TeBr_2$ that comes from the decomposition of $TeBr_4$. W is added as a metal powder and some metal powder of Te is added, in order to reach a final stoichiometric composition, which is 1:2:0.16 (W:Te:Br). Mixed powders are inserted into a two-chamber silica ampoule. The Yttrium-stabilized Zirconia substrates (CRYSTALTECH GmbH, $3 \times 5 \text{ mm}^2$) are placed in the tube, which is pumped down to 10^{-3} mbar and sealed. We note here that the growth onto a Si/SiO₂ wafer was not successful. The closed silica ampoules were then heated in a two-zone furnace and placed within a temperature-gradient zone, between 675°C (min. T_1) and 725°C (max. T_2), during a reaction time $t = 10$ h. After the growth, the ampoules were quenched to room temperature starting from the source side to avoid further deposition on the substrate, and they were finally opened in the glove box. Details on the growth by CVT of our samples can be found in the article [Hansen et al., 2020]. On the YSZ substrates, isolated nanosheets coexist with some clusters (dendrites) of WTe_2 as shown on figure 3.2.

Characterization of nanosheets

To confirm the crystal stoichiometry, the composition was first measured by energy-dispersive X-ray (EDX) as shown on figure 3.3. The EDX were performed using a "FEI Nova NanoSEM" (FEI, Japan) scanning electron microscope (back scattering electron detector; 30 kV) with an attached "AMETEK Quanta 200/400" (AMETEK, USA) EDX (30 kV) unit and the software "EDXGenesis". This analysis was made on a thick cluster in order not to detect peak from the YSZ substrate, the nanostructures being too thin otherwise. From the indexation of the peaks of W and Te with their respective intensities, the software calculates the composition of the structure, finding 34% of W and 66% of Te. A comparison of the nanosheet with the cluster was made by using polarized Raman spectroscopy with a "T64000 Spectrometer" (Horiba Jobin Yvon, USA). The laser used in the Raman device was a linear polarized "Torus Laser" ($\lambda = 532 \text{ nm}$, $P = 3 \text{ mW}$, spot size $\approx 1 \mu\text{m}^2$). The polarization of the laser was turned

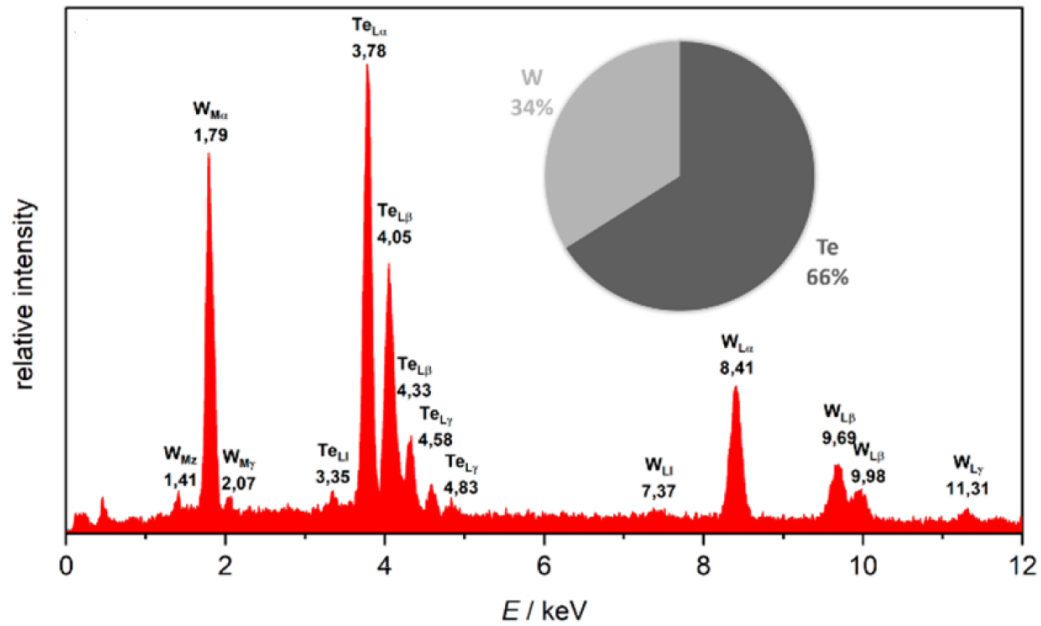


FIGURE 3.3: EDX measurement (30 kV) of a bulky crystal cluster showing the composition expected for WTe_2 . Adapted from [Hansen et al., 2020]

in 15° steps during the measurement to measure both structures. The measurement and comparison made on the nanostructure and the cluster indicated in figure 3.4 a), show that the average measurement over all polarizing angles of WTe_2 nanocrystal is similar to the measurement of the cluster and confirms therefore the WTe_2 crystal stoichiometry of the nanosheet.

The Raman spectra also confirms the crystallinity of the WTe_2 nanosheet. In the case of Raman signal collected in backscattered geometry and if the incident light is perpendicular to the ab plane, only A_1 and A_2 symmetry modes are active

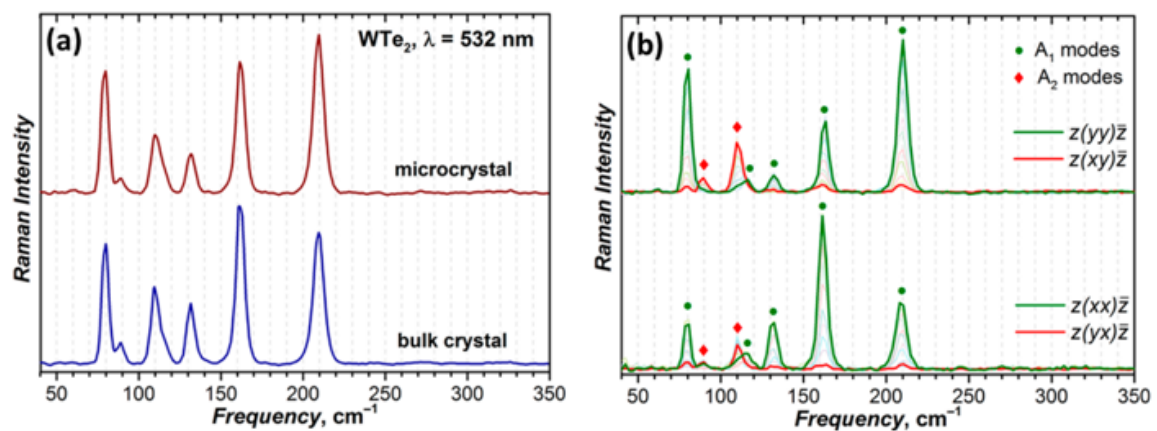


FIGURE 3.4: a) Comparison of Raman spectra measured on a bulk crystal and a nanosheet, b) Raman spectra of a nanosheet as a function of the frequency for different polarizing angle. Adapted from [Hansen et al., 2020]

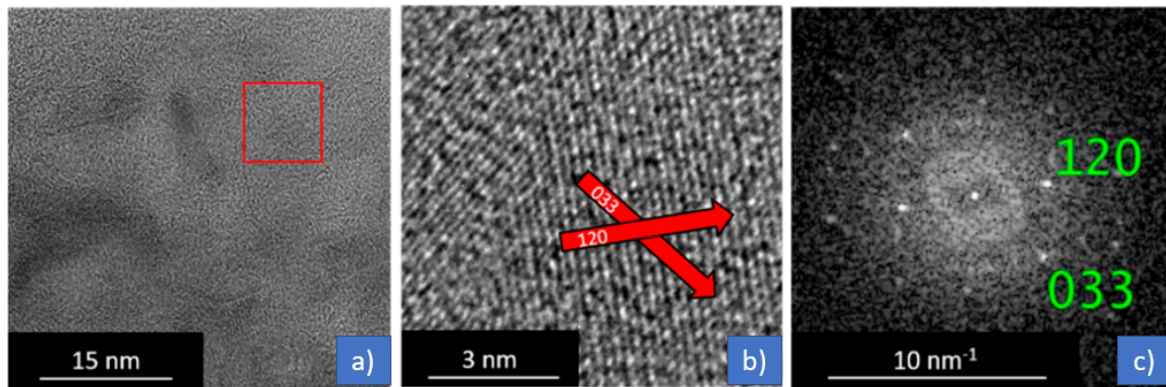


FIGURE 3.5: a) High resolution TEM image taken at the edge of a nanoflake, revealing the atomic crystalline structure; b) zoom-in of the region marked by a red square in a) with lattice planes identified by red arrows and assigned to the Miller-indices of $1T_d$ -WTe₂; c) Fourier transform of b) showing reflections corresponding to the indexed lattice planes. Adapted from [Hansen et al., 2020]

in Raman spectra of WTe₂ single crystal [Kong et al., 2015]. Moreover, the different Raman tensors of A1 and A2 leads to a different geometry of the polarization plane of the incident light and detected light, at which these modes can be best observed. Thus, A1 and A2 modes are active for certain angles of the laser polarization plane in single crystal, which will not be the case for not well-ordered or polycrystalline sample. As shown on figure 3.4 b, the nanostructure is showing the mode A1 and A2 for two different angles of polarization, confirming the single crystallinity of the flake. Last but not least, to verify and confirm the orthorhombic crystal structure (space group Pmn21) of WTe₂, aberration-corrected high-resolution transmission electron microscopy (HR-TEM) was also performed with selected area electron diffraction (SAED) as shown on figure 3.5.

3.1.3 Flux Growth

Growth Principle

Bulk single crystals of WTe₂ were grown via the self-flux method [Tachibana, 2017]. A flux, also called a solvent, is used to dissolve a solute in a solution. The sealed crucible where the solute can be found, is placed into an electric resistance furnace. The crucible is kept at very high temperature for a moderate time, during which the content melts completely and becomes a uniform solution. The temperature is then lowered at a certain rate per hour. The solute becomes less soluble as the temperature decreases, eventually reaching a point of supersaturation, a condition where the concentration of the solute exceeds the solubility of the solution. Then, a number of microscopic nuclei of the material begin to form in the solution. With a further

decrease in temperature, additional solute particles are attached to the nuclei, layer upon layer, in an orderly array, eventually growing into visible crystals. After the desired temperature is reached, the furnace is shut off and the crucible is cooled to room temperature in a fast quench. Once the crucible is removed from the furnace, the solidified flux can be dissolved in hot dilute nitric acid for several days or, instead, quickly removed when the hot flux remains liquid.

Single-crystalline WTe_2 were grown by Grigory Shipunov at the IFW Dresden, in the group of Saicharan Aswartham. More details on the crystal growth and characterization of these macrocrystals will be published in the PhD thesis of Grigory Shipunov. To prepare the solute of WTe_2 , 0.5 g of tungsten powder (Alfa Aesar, 99.95%, 200+325-mesh) were mixed with 10 g of tellurium powder (Alfa Aesar, 99.999%, 18-mesh), grinded to homogeneity and put into a canfield crucible set made of alumina. The crucible was in turn sealed in quartz ampoule under vacuum. The setup was heated up to 1000°C , after which it was cooled to 800°C during 160 hours. Afterwards, it was taken out of the furnace and quickly centrifuged to separate the liquid Te flux from the WTe_2 crystals. As shown in figure 3.6, needle-shape large single crystals were obtained, with clearly visible facets.

Characterization of bulk single crystal

These crystals were characterized by energy-dispersive X-ray spectroscopy for the compositional analysis and by X-ray diffraction for the structural analysis. As an example, the crystal shown in the right panel of figure 3.6 has a uniform composition (34% W, 66% Te), as obtained from EDX spectra, all over its homogenous surface.

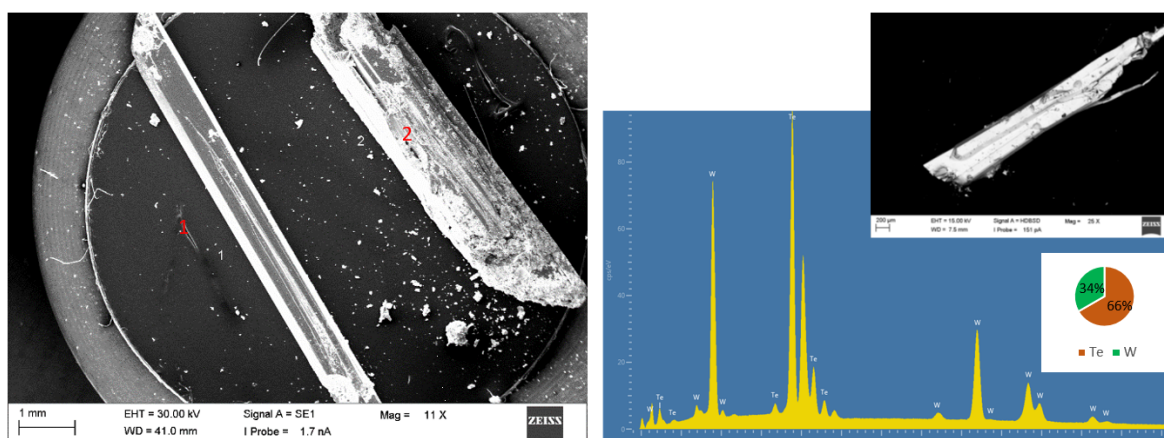


FIGURE 3.6: Left panel : SEM image of a WTe_2 cleaved macrocrystal from Te-flux growth, right panel : EDX spectrum of a WTe_2 cleaved macrocrystal (in inset, scale bar 200 μm) showing the good stoichiometry for WTe_2 .

Further, the structural characterization was performed by single-crystal X-ray diffraction, which confirmed the crystal structure of WTe_2 , as reported in the NIST Inorganic Crystal Structure Database ICSD No. 73323, [Mar et al., 1992]).

3.2 Nanostructures of WTe_2

In this work, three devices were investigated in detail. Two nanostructures were obtained by CVT with a thicknesses of 50 nm (sample S1) and 70 nm (sample S2, bottom left flake of figure 3.9). A third one was prepared by mechanical exfoliation, with a thickness of 100 nm and having a hall-bar shape (sample S3, figure 3.8). Besides, two other samples were also studied prior to this work : another exfoliated flake, with a thickness of 70 nm and an aspect ratio close to one (sample S4, see [Sykora et al., 2020b]), and a large bulk crystal (sample S5).

3.2.1 Exfoliation and search of nanostructures

Exfoliation

In 2004, Novoselov and Geim managed to isolate for the first time graphene flake, a monolayer of graphite [Novoselov et al., 2004]. To do so, they used a simple and robust technique called mechanical exfoliation, based on scotch tape technique. This technique has contributed to the rise of the nowadays very active field of 2D materials, and is applicable to the wide range of Van der Waals materials.

The principle of mechanical exfoliation relies on the properties of Van der Waals materials. In these materials, the crystallographic structure is made of strong covalent bonds within a quasi-2D plane, whereas there is a weak Van der Waals interaction between neighbouring planes. The material can therefore be seen as a pile of 2D layers, which can be easily cleaved so as to separate them. Exfoliation is the general

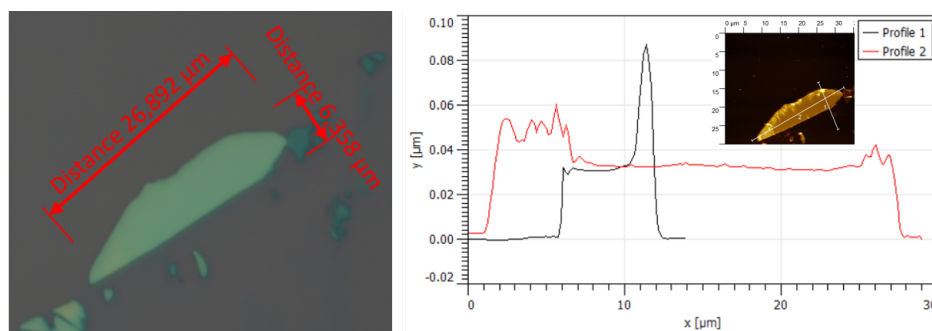


FIGURE 3.7: Optical image of a WTe_2 nanostructure with a thickness of 30 nm and the AFM measurement of the structure with 2 different profiles

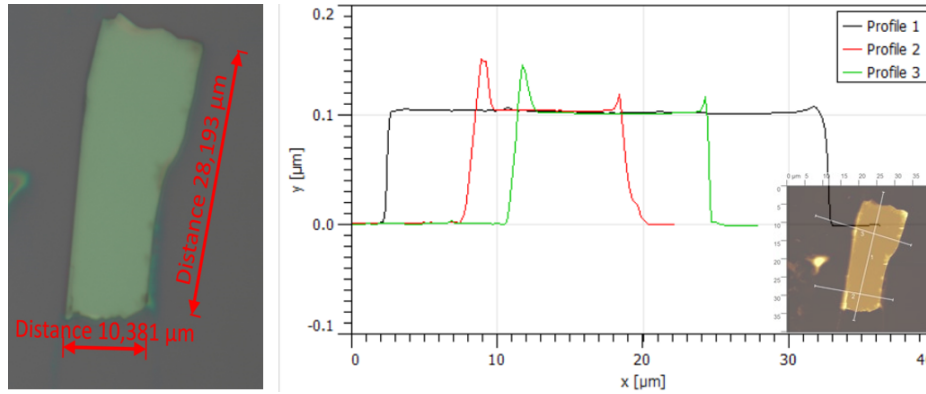


FIGURE 3.8: Optical image of the sample S3 and the AFM measurement of the structure with 3 different profiles

process consisting in separating these layers from one another, while keeping their in-plane bonds intact. Different methods of exfoliation exist but only the mechanical exfoliation was used to thin down WTe_2 . An important aspect is the choice of the substrate. As for other Van-der Waals materials, the thickness of the SiO_2 allows us to roughly determine the thicknesses of the flakes thanks to the color contrast of the nanostructures in optical microscope imaging. Green colored flakes correspond to rather thin structures as shown by the example of a 30 nm thick flake (figure 3.7), a thickness that was measured by atomic force microscopy (AFM). Another sample of a 100 nm thick flake and its height profile measured by AFM is shown in figure 3.8. This nanostructure (S3) was connected by electron beam lithography as described later.

Search of nanostructures

Considering the change of the band structure below 50 nm [Xiang et al., 2018], we focused on the search of exfoliated nanostructures with a thickness in the 50 nm-100 nm range, being large enough to be contacted by EBL patterning and metal lift off. Depending on their color on SiO_2 , it was possible to find such thin flakes as describe above, and to focus on flakes with a reasonable in-plane aspect ratio that

	Substrate 1	Substrate 2
15 nm	0	2
Between 50 and 75 nm	2	0
Between 75 and 100 nm	6	1
Between 100 and 150 nm	10	0
Above 150 nm	10	1

TABLE 3.1: Thickness distribution of WTe_2 nanostructures grown by CVT on 2 different YSZ substrates

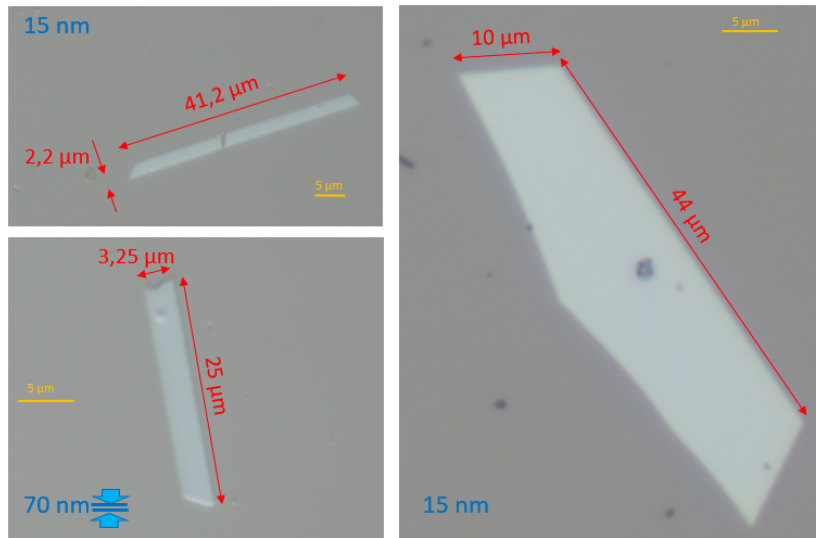


FIGURE 3.9: Optical images of three WTe_2 nanostructures grown by CVT with their respective dimensions (in-plane in red, thickness in blue).

could allow the nanofabrication of ohmic contacts in a Hall-bar geometry.

For nanostructures grown by vapor transport on YSZ substrates, no color contrast could help us to distinguish thinner flakes from thicker ones, due to the absence of light interference as in Si/SiO₂ substrate. A careful investigation, based on combined optical microscope and AFM imaging, allowed us to identify several nanostructures. The thickness distribution of the nanostructures identified on two substrates is given in table 3.1. Contrary to exfoliated flakes, nanostructures grown by CVT have well-defined edge orientation, corresponding to specific crystal axes, and they can have atomic-flat surfaces, possibly with some dirt formed during the rapid quench (local clusters of Te at the surface only).

3.2.2 Nanofabrication

To realize ohmic contacts on individual nanostructures, some standard clean-room techniques were used and the general processing scheme is sketched in figure 3.10. First, an electron beam lithography process (EBL) is realized in order to create a mask into a thin layer of poly(methyl methacrylate) (PMMA), a positive electron-sensitive resist, after development in MIBK/IPA. Prior to the ebeam evaporation of metal, the sample is shortly etched by ion beam etching in order to improve the transparency of the contacts. Following the metal deposition, the resist is removed in acetone, which leaves the metal contacts only in the patterned areas. Finally, the sample is fixed with silver paste onto a non-magnetic leaded ceramic chip carrier from Kyocera, and the contacts are connected by aluminium wire bonding. The different steps of the process are described below in more details. Between the different steps of

exfoliation, nanopatterning or measurement, the sample was kept in a dessicator to limit oxidation and aging of the sample. The different final devices are shown in figure 3.11.

For the nanofabrication on SiO_2 , a standard EBL process of PMMA is performed. A first step of spincoating PMMA at 4000 rpm for a thickness of 350 nm is followed by a baking process during 3 mn at $150^\circ C$ on a hot plate. Then the substrate is inserted into a scanning electron microscope (SEM) modified with an EBL unit from Neomicra and a pattern is exposed. High-energy electrons with an acceleration voltage of 30 kV will break the polymer chains during the exposure. A dose test was made before on a bare Si/SiO_2 substrate. To know the clear dose, which corresponds to the minimal dose to fully develop PMMA in the exposed areas. With our setup, a dose of $300 \mu C.cm^{-2}$ was used to expose PMMA on Si substrates, a value that is chosen slightly above the clear dose, so as to avoid any issue related to a possible defocusing of the beam.

After exposure, the resist was developed for 90 s in a solution of MIBK (Methyl isobutyl ketone) distilled in IPA (isopropanol) for a ratio of 1 MIBK for 3 IPA. The surface of WTe_2 is sensitive to oxidation in air [Woods et al., 2017]. However, this oxidation is limited to the few first atomic layers, on a length scale that is much smaller than the thickness of the nanostructures investigated in this work. Still, in order to have good ohmic contact a small ion beam etching by argon is made in-situ in the metal evaporator from Plassys (MEB550S). Then, the metal deposition was made, where a thin layer of chromium (around 10 nm) is deposited followed by a

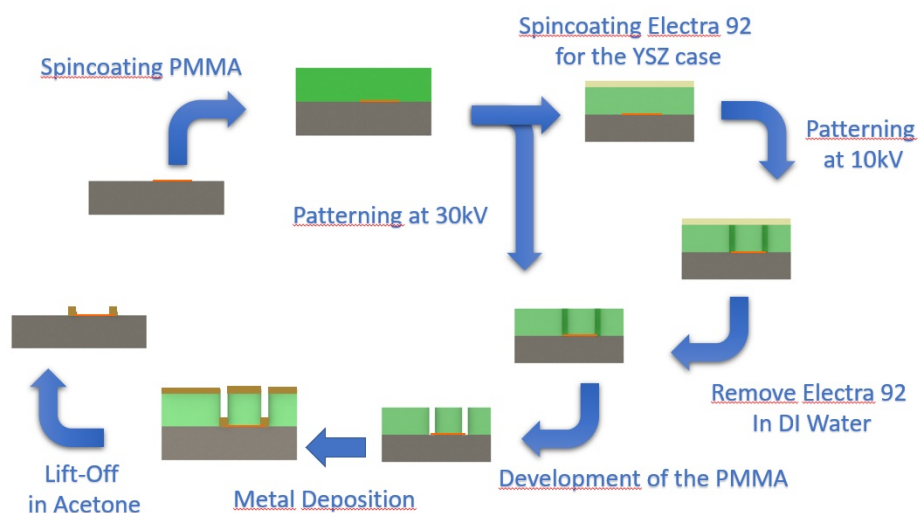


FIGURE 3.10: Nanofabrication process, step by step on SiO_2/Si and YSZ substrates. In the latter case, an additional step is needed, so as to avoid charging effects during the e-beam exposure.

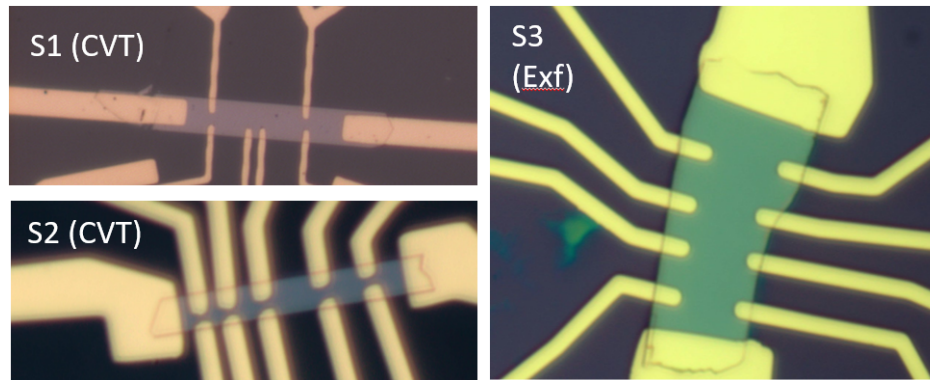


FIGURE 3.11: Optical images of CVT and exfoliated nanostructures connected,
 S1 (CVT, $50 \text{ nm} \times 30 \mu\text{m} \times 8 \mu\text{m}$),
 S2 (CVT, $70 \text{ nm} \times 25 \mu\text{m} \times 3.2 \mu\text{m}$),
 S3 (exfoliated, $100 \text{ nm} \times 28 \mu\text{m} \times 10.3 \mu\text{m}$)

layer of 90 nm of gold. The layer of chromium act as an adhesion layer for gold on silicon oxide. Finally, the metal lift-off process is made with acetone, a solvent that removes the PMMA mask.

With insulating YSZ substrates, the EBL process is not as trivial as for Si/SiO₂ substrates. Due to a surface charging effect, the local deflection of the beam results in a distorted pattern. Moreover, the clear dose of PMMA is much more lower than the one found for the process on Si/SiO₂ substrates. To dissipate the charge and get rid of the distortion, another resist layer was added to the EBL process. On top of the PMMA, a conductive layer is spincoated (Electra 92 from Allresist) and during the EBL process, a clamp was put on a side of the sample to drain the charges to the ground.

However, this does not solve the problem of overexposure of PMMA since the energy loss of the electron beam occurs mostly in the resist, with a significant lateral broadening due to some interaction within the substrate. A way to overcome this issue was found by decreasing the beam acceleration from 30 kV to 10 kV. This decreases the interaction volume of the electron beam, and therefore reduces the influence of the substrate. After exposure, a first remover is used for the conductive layer : deionized water for the case of the Electra 92. Then the development of the PMMA layer is made and the process follows as described before.

3.3 Cryogenics and low noise measurement techniques

Magneto-transport measurements were first performed from room temperature down to about 2K by using a variable-temperature insert (Oxford compact VTI), fitted into a 1-12 T 2D vector magnet. This allowed us to study the magneto-resistance, both

in the high-field regime (large positive XMR) and in the low-field regime (no signature of the chiral anomaly). This temperature range corresponds to the range where these effects were reported. In addition, we used a ^3He - ^4He dilution refrigerator, fitted into a 2-2-6 T 3D vector magnet, to evidence a low-field isotropic magneto-resistance at very low temperature ($T \geq 100\text{mK}$) that is related to a novel mechanism due to the presence of Weyl nodes in the band structure as described in chapter 5.

3.3.1 ^3He - ^4He dilution refrigerator system

Very-low temperatures can be obtained with a ^3He - ^4He dilution refrigerator, which uses the endothermic process of the diffusion of ^3He into ^4He (entropy increase) in a close circuit [White and Meeson, 2002][De Waele, 2011]. The principle of a dilution fridge refrigerator is described below and a schematic of the instrument with its different elements is shown in figure 3.12. First, by using a 1 K pot (adiabatic expansion of pumped ^4He) in thermal contact to the upper part of the dilution unit in the condenser, it is possible to liquefy the ^3He - ^4He mixture to a temperature of 1.2 K. Then the lower stage of the dilution unit is further cooled down to about 700 mK by passing the mixture through different impedances, where the liquid separates into two phases, an ^3He -rich phase floating over a ^3He -poor phase (^4He -rich). The interface between the two phases is located in the lowest part of the dilution unit called the mixing chamber. The cooling power below 700 mK results from the diffusion of ^3He from the rich to the poor phase in the mixing chamber (increase of entropy, equivalent to a heat pumping or a decrease of temperature). This requires the circulation of ^3He in order to operate continuously the refrigerator. Therefore, the liquid-gas interface of the ^3He -poor phase is adjusted to be located in an upper chamber called the still from which the mixture is pumped out. Due to the lower vapor pressure of ^3He , mostly ^3He evaporates, so that it can be pumped out and be reinjected in the refrigerator loop through the condenser ensuring hence a steady state with a permanent flow of ^3He . In order to increase the efficiency of the refrigerator, continuous and discrete thermal exchangers are installed between the cold part and the hot flow of mixture. This improves the cooldown of the mixture on the way to the mixing chamber and reciprocally, it will warm up the mixture on the way to the still, increasing the temperature of the still, the pumping of ^3He and therefore the related efficiency of the setup. This system can reach temperatures as low as 6 mK for the lowest electronic temperature reported [Iftikhar et al., 2016].

The ^3He - ^4He dilution refrigerator used in this work is a commercial Kelvinox 300 dilution unit from Oxford instruments built in 1992. The cooling power is 100 μW at 100 mK, and it has a temperature base of 45 mK. The refrigerator temperature

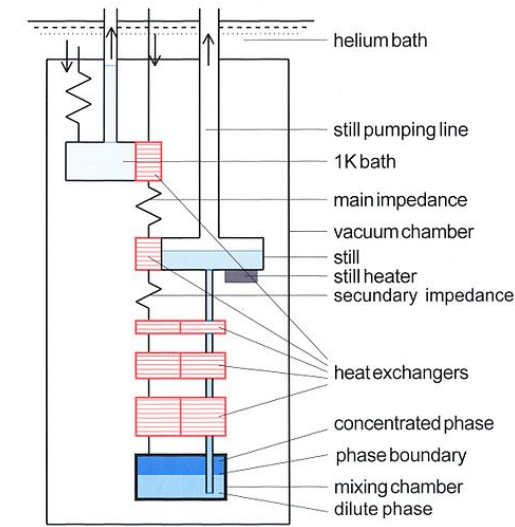


FIGURE 3.12: Schematic of a dilution fridge, adapted from [De Waele, 2011]

can be controlled by an home-made PID loop, using a Yokogawa voltage source to heat a resistor installed on the mixing chamber. The thermometers mount on the sample cold fingers are a RuOx resistance calibrated between 10 mK to 800 mK and a cernox resistance calibrated between 1.2 K and 300 K.

In transport measurement, a challenging aspect is the electronic temperature of the quasi-particle in the measured sample. Indeed, because of a strongly reduced electron-phonon coupling (usually below 1K), it is possible that a non-equilibrium appears between the temperature of the lattice and that of the electrons, since the energy relaxation rate of the electrons is strongly reduced. As a result, the electronic temperature can be much higher than the value given by the nearby thermometer. The cooling of the electrons is then best achieved by a good electrical wiring, which needs to be well anchored to the heat exchangers and is made with constantan wires in order to filter some incoming electrical noise and reduce heat coming from the room temperature stage. Moreover, the voltage applied to the sample must remain small, following the rough rule that $eV \leq k_B T_{\text{cryo}}$. Ultimately, the temperature is given by the sample itself, as inferred for instance from the temperature dependence of quantum transport phenomena. In the case of this dilution refrigerator, the electronic base temperature is roughly around 100 mK when the cryostat base temperature is 50 mK. The dilution unit is inserted in a cryostat fitted with a 3D vector magnet 6-2-2 T.

3.3.2 Low noise electrical measurements

Due to the low resistivity of the semimetals at very low temperature, it is important to consider two factors to measure their transport properties accurately by either

increasing the signal or reducing the noise. First, the geometrical factor can be optimized (to increase the signal). This can be done in two ways. In thin nanostructures, the square resistance $R_{\text{sq}} = \rho/t$, where t is the thickness, is increased. Also, a large in-plane aspect ratio L/W gives a larger sample resistance $R = R_{\text{sq}} \times L/W$. Second, we use lock-in amplifiers to obtain a good signal-to-noise ratio (reduction of the noise), with signals that can be as low as 10 μV (equivalent electronic temperature of 100 mK). A lock-in amplifier delivers a sine-wave signal at a given frequency and can then measure an input signal at the same frequency. This synchronous detection allows us to get rid of a large part of the noise and parasitic signals. Still, since the AC lock-in amplifiers have a lowest input noise for a charge impedance of about 1 kOhm, it can be needed either to increase the sample resistance or to use an impedance adapter, such as the SR554 from Standford Research. For our measurements, we used a current-polarization configuration, for which the lock-in voltage output is applied to a polarization resistance of 100 k Ω or 1 M Ω that is much larger than the sample resistance connected in a series.

The data are collected by a home-made Labview-program on the computer that is communicating with all the different instruments via serial or parallel ports. This Labview program was implemented as a multi-menu virtual instrument, so as to allow the user to choose a versatile measurement scheme (vector magnetic-field sweeps, temperature dependence, etc.). During my thesis, I took over the project, I improved its front-panel, and added new functionalities to a final version that is now used for all the different setups of the group.

With these setups, we conducted different studies. First, a comparative study of the XMR up to 12 T was performed in nanostructures with different degrees of disorder. The goal was to investigate the possible influence of the point-defect structural disorder on the subquadratic law. This comparative study led to the development of a multi-band model to take into account the complexity of the band structure, and the analysis was further supported by ab-initio calculations made by S. Sykora. Second, we studied the low-field MR, which was reported by different groups as the signature of the chiral anomaly whereas the transport conditions (position of the Fermi level, disorder) are not favorable to realize this effect in nearly charge-compensated WTe_2 . Questions raised by this initial study led us to investigate the very-low temperature regime. We gave evidence for a new effect due to the non-trivial topology of a Weyl semimetal inducing an isotropic negative longitudinal magnetoresistance that exists when the Fermi energy is far away from the Weyl nodes.

EXTREME MAGNETORESISTANCE : BAND STRUCTURE AND DISORDER

4.1 Motivation

As discussed in the chapter 2, WTe_2 is a material with rich properties, some of which being related to its topologically non-trivial band structure, such as the planar Hall effect and the anisotropic chiral anomaly. Importantly, the band structure of WTe_2 exhibits not only Weyl points but also trivial bands, all of which can be coupled to another through a static disorder. A legitimate question is : can this coupling within topological bands or between topological and non-topological bands reduce the topological response in this material. In a previous work [Sykora et al., 2020b], such a coupling was revealed by investigating the transport properties of an exfoliated nanostructure of WTe_2 (sample S4) and the impact of disorder on the inter-cone scattering of Weyl quasiparticles was evidenced. Based on a fine analysis of Shubnikov-de Haas oscillations combined with that of longitudinal and Hall magnetoresistances, the quantum life time and the transport time were measured and a theoretical model allowed us to relate their ratio to the disorder correlation length, giving some direct information on the coupling between the electronic bands. This mixing of Weyl quasiparticles of opposite spin chirality or the coupling between trivial and non trivial bands thus results in the suppression of topologically nontrivial properties.

Obviously, disorder also influences trivial transport properties. Yet, as explained before, the Hall and longitudinal magnetoresistance of WTe_2 can be rather well described by a two-band model, and the XMR amplitude is often used as a measure of the charge imbalance and average mobilities. Nevertheless, most studies reported a deviation from the two-band model and a subquadratic longitudinal magnetoresistance was systematically observed [Thoutam et al., 2015] [Wang et al.,

2016b] [Fatemi et al., 2017] [Wang et al., 2019]. This cannot be simply attributed to a deviation from the full charge compensation but rather to a deviation from the two-band model itself since no saturation is observed even at high temperature. Such a deviation can be expected since the real band structure was found to have two electron pockets and two hole pockets. In addition, the influence of carrier mobilities should be considered as well. Besides, it remains unclear whether disorder strongly influences this subquadratic power-law behavior of the XMR or not. Here, by comparing samples grown by different methods, leading to very different densities of impurities, we quantitatively investigate the effect of the disorder degree on the magnetotransport properties and we study the correlation between the subquadratic longitudinal magnetoresistance and the disorder strength. In addition to the exfoliated sample S4, we measured three other samples, two grown by vapor transport (S1 and S2), and one mechanically exfoliated (S3) from a macrocrystal and compared our results to those measured in a macroscopic crystal (S5).

In this chapter, the transport properties of more or less disordered nanostructures are studied in perpendicular magnetic fields as large as 12 T. Analysing the extremely large magnetoresistance within a two-band model, the average charge carrier densities and mobilities for electrons and holes are extracted. Then, by analysing the Shubnikov-de Haas oscillations, we refine our fitting parameters in the framework of a multi-band model. Considering only three bands, we compare our results to the transport properties of a previously studied exfoliated nanostructure S4 and a bulk single crystal S5 with the highest crystal quality we measured so far. Based on this comparative study, we attribute the subquadratic behavior of the longitudinal magnetoresistance to the multiband nature of the system. Then, generalizing the two-band model to a n -band model and considering numerical calculations based on the real band structure, we unveil the role of the disorder in the deviation from the two-band model and give a fully coherent understanding of the multiband transport properties of disordered WTe_2 structures.

4.2 Temperature dependence of the longitudinal resistivity

All samples show a metallic behavior while cooling down to helium liquid temperature as shown in figure 4.1 for the samples S2 and S3. The residual-resistivity ratio $RRR = R(300\text{ K})/R(4.2\text{ K})$ of the CVT-grown sample S1 is 23. This rather small ratio indicates a strong disorder in the nanostructure. The CVT grown sample S2 has a higher value of 40. The sample S3, exfoliated from a macrocrystal grown by Te-flux,

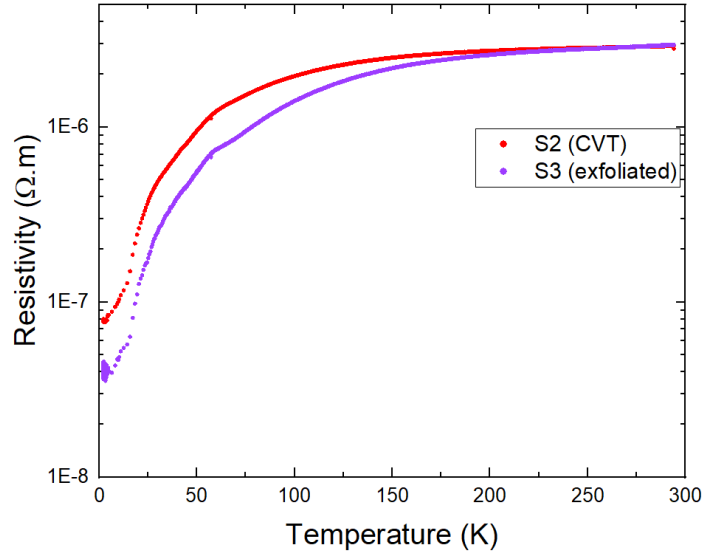


FIGURE 4.1: Temperature dependence of the longitudinal resistivity of the nanostructures S2 and S3.

gives a value of 80. These results therefore reveal the different strength of disorder in our samples. CVT grown samples seem to have higher densities of point defects than macroscopic crystals. Different informations for each sample such as the RRR , the thickness, the MR at 6 and 12 T and the exponent of the power law (extracted from linear fit between 1 and 6 T) are summarized in table 4.1.

4.3 Extreme magneto-resistance

4.3.1 Simple analysis of the experimental results

Within the two-band model described in chapter 2, the magnetoresistance is directly influenced by the disorder through the mobilities μ_e and μ_h . Hence, for a fully compensated system, the quadratic magnetoresistance is directly proportionnal to the mobilities.

$$\rho_{xx} = \frac{1}{e} \frac{n_e \mu_e + n_h \mu_h + (n_e \mu_h + n_h \mu_e) \mu_e \mu_h B^2}{(n_e \mu_e + n_h \mu_h)^2} \quad (4.1)$$

This model also captures that a deviation from charge compensation results in a saturation of the MR in high fields, which limits its maximal amplitude. The validity of this simple approach is roughly confirmed by our experimental results. For a magnetic field applied out-of-plane, the magnetoresistance at 6 T is relatively small and equal to 440 % for the sample S1, which is coherent with its low RRR value. The sample S2, having a larger RRR value, shows an XMR of 1500 % at 6 T and 4600 %

Sample	t (nm)	RRR	MR (%) at 6 T	MR (%) at 12 T	α
S1 (CVT)	50	23	440%		1.78
S2 (CVT)	70	40	1500%	4600%	1.64
S3 (exfoliated)	100	80	4300%	16000%	1.82
S4 (exfoliated)	70	80	6400%		1.81
S5 (macrocrystal)	/	185	19000%	73775%	1.84

TABLE 4.1: Thickness, RRR , magnetoresistance and Kohler's exponent α of the different samples measured.

at 12 T. These values remain smaller than those obtained with S3, the exfoliated structure with a higher RRR , with 4300 % at 6 T and 16000 % at 12 T. Although this trend is in good qualitative agreement with expectations from the two-band model, it is already visible that our results do not exactly follow the μ^2 dependence as the amplitude decreases for a reduced mobility (smaller RRR).

We present below the two-band model analysis of the transport results for the samples S1, S2 and S3. Contrary to others, the strongly disordered structure S1 does not show any Shubnikov-de Haas oscillations up to 6 T. Nevertheless, an analysis of the longitudinal and Hall resistivity by the two band-model already gives us informations about the average carrier densities and mobilities. In order to analyse correctly our data and to avoid some mistake due to a misalignment of the contacts on the nanostructure, the Hall resistivity is anti-symmetrized and the longitudinal resistivity is symmetrized. Because of the lack of Shubnikov-de Haas oscillations, all charge densities were unknown and no parameter was fixed in the fit with the two-band model. To have a relevant analysis, we analysed the longitudinal

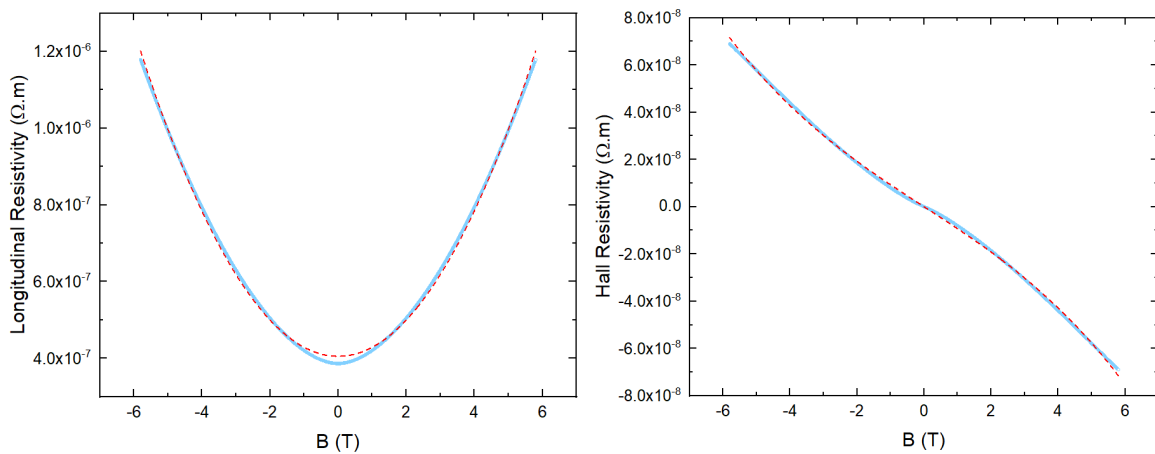


FIGURE 4.2: Longitudinal (left) and Hall (right) resistivity as a function of a perpendicular magnetic field measured at 4.2 K for S1 and a current $I = 10\mu\text{A}$. The red dashed line on both graph are the two-band model fits with $n_e = 3.24 \times 10^{19} \text{ cm}^{-3}$, $n_h = 3.13 \times 10^{19} \text{ cm}^{-3}$, $\mu_e = 0.25 \text{ m}^2/\text{V.s}$ and $\mu_h = 0.23 \text{ m}^2/\text{V.s}$.

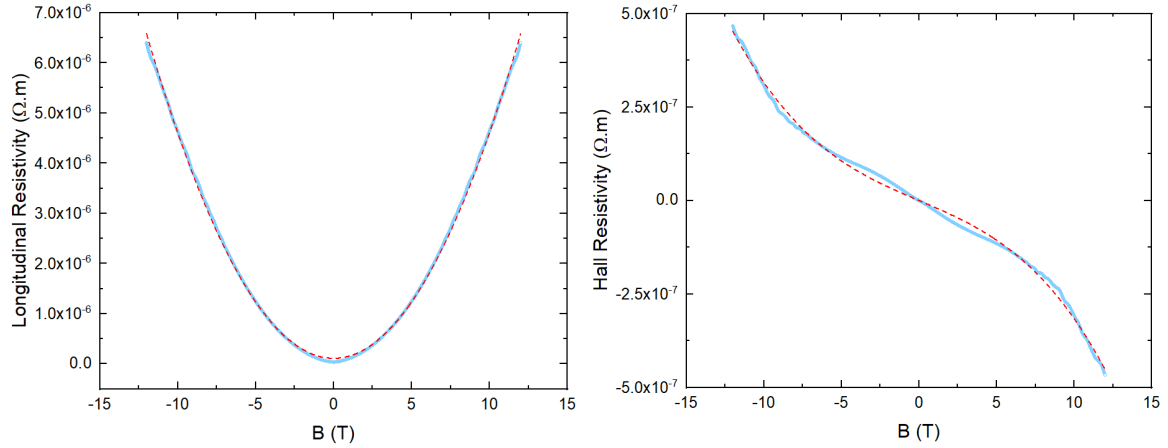


FIGURE 4.3: Longitudinal (left) and Hall (right) resistivity as a function of a perpendicular magnetic field measured at 4.2 K for S3 and a current $I = 10\mu\text{A}$. The red dashed line on both graph are the two-band model fits with $n_e = 4.38 \times 10^{19} \text{ cm}^{-3}$, $n_h = 4.33 \times 10^{19} \text{ cm}^{-3}$, $\mu_e = 0.71 \text{ m}^2/\text{V.s}$ and $\mu_h = 0.56 \text{ m}^2/\text{V.s}$.

and Hall signal in a global fit with the equations 2.7. The fit gives us very similar mobilities for holes and electrons, 0.23 and 0.25 $\text{m}^2/\text{V.s}$ respectively (figure 4.2). The hole carrier density ($3.13 \times 10^{19} \text{ cm}^{-3}$) is found slightly larger than the electron density ($3.24 \times 10^{19} \text{ cm}^{-3}$). Nevertheless, the ratio is still close to unity and the rather low magnetoresistance cannot be attributed to the partial charge compensation but rather to a reduced mobility. A small deviation between the fit and the experimental data measured can be observed in the figure 4.2. This deviation occurs in both the longitudinal and the Hall resistivity and is likely due to the multiband character of the system, which has four bands (two holes and two electron subbands). The more robust analysis of the transport properties based on a multi-band model will be discussed in section 4.4.1).

Samples S2 and S3 were studied with an out-of-plane magnetic field up to 12 T. As shown in figure 4.3 for sample S3 and like for sample S1, the fit of the longitudinal and Hall resistivity by the two-band model is not in perfect agreement with the measurements, and visible deviations in the fit of the Hall data are clearly visible. Still, this first rough analysis remains a rather good approximation, giving values for electron and hole mobilities of 0.71 and 0.56 $\text{m}^2/\text{V.s}$ respectively. These values are significantly larger than those found for S1, as expected for a smaller degree of disorder. The carrier densities are $4.38 \times 10^{19} \text{ cm}^{-3}$ for electrons and $4.33 \times 10^{19} \text{ cm}^{-3}$ for holes. It is again larger than the values found for sample S1.

Several points need to be considered to understand this difference between S1 or S4 [Sykora et al., 2020b] that both can be fitted by the two-band model with a good agreement, giving carrier densities around $3 \times 10^{19} \text{ cm}^{-3}$ and S3 that shows

Samples	Two-band model with longitudinal resistivity			Two-band model with $\delta R/R$			
	S1	S3 up to 12 T	S3 up to 6 T	S1	S3 up to 12T	S3 up to 6 T	S4
$\mu_h(\text{m}^2/\text{V.s})$	0.23	0.56	0.67	0.34	0.99	0.97	1.14
$\mu_e(\text{m}^2/\text{V.s})$	0.25	0.71	1.07	0.37	1.17	1.26	1.86
$n_h(10^{19}\text{cm}^{-3})$	3.13	4.33	5.41	3.00	3.31	3.15	3.05
$n_e(10^{19}\text{cm}^{-3})$	3.24	4.38	5.48	3.04	3.32	3.16	3.01

TABLE 4.2: Carrier densities and mobilities for different two-band model fit of the relative resistance, longitudinal and Hall resistivity of S1, S3 and S4

stronger deviations from the two-band model and higher carrier densities. First, S1 and S4 were both measured up to 6 T whereas S3 was investigated under magnetic fields up to 12 T. Secondly, in order to get rid of any geometry dependence for the nanostructure S4, we fit the relative resistivity $(R(B)-R(0))/R(0)$ instead of the resistivity. By taking into consideration these two points, other fits were done for S1 and S3 showing similar carrier densities. The fitting parameters are summarized in the table 4.2, and the different fit for the data measured on the sample S3 with a comparison of the residue can be found in appendix A. To conclude, the analysis of the data in the framework of the two-band model leads to a good agreement between the theory and the experimental data for a magnetic field up to 6 T and to some consistent values of the charges densities and mobilities. Nevertheless, this approach appears not to be well adapted to an analysis over a broader magnetic field range (up to 12 T) where the data cannot be fitted very accurately and where the parameters extracted from the fit lead to inconsistent values. This points out that more bands need to be considered to describe the transport properties of WTe_2 in order to perform a quantitative analysis of the measurements. To go beyond the two-band model and to extract reliable transport properties from the multiband model, we first need to determine the charge densities associated to the different charge pockets from quantum oscillations of the resistivity in large magnetic fields.

4.3.2 Refinement based on the Shubnikov-de Haas measurements

Due to the formation of Landau levels, clear oscillations of the longitudinal resistance are observed in high magnetic fields, as evidenced in samples S2 and S3 (see figure 4.4). After removing a smooth background and plotting the residual resistance as a function of the inverse of the magnetic field (figure 4.5), these Shubnikov-de Haas oscillations can be assigned to different electronic bands, each population being related to a given peak in the fast-Fourier transform (FFT) of the oscillations. Due to the limited field range, FFT peaks related to the different charge pockets are best

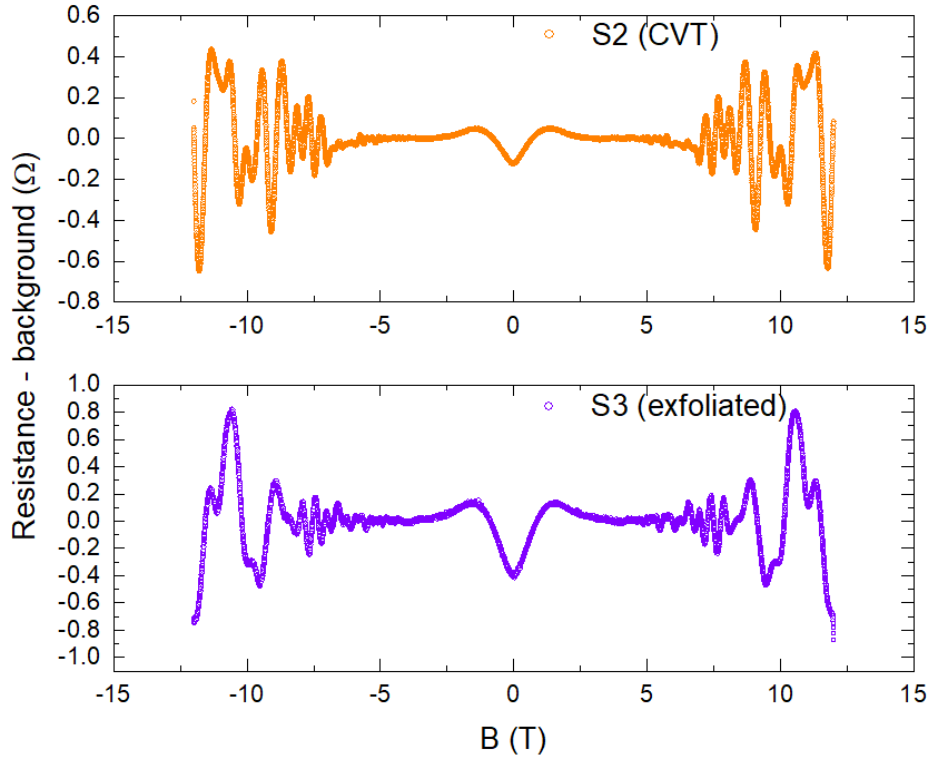


FIGURE 4.4: Resistance with the background removed as a function of the magnetic field up to 12 T showing clear Shubnikov-de Haas oscillations.

identified by comparing the results obtained for different pairs of contacts, allowing us to clearly identify all four bands, as shown in Fig.4.4 for the S3 sample.

Four FFT peaks are observed at the frequencies 87 T, 122 T, 135 T and 168 T. A peak at 50 T is also present but is not observed for all pair of contacts. It probably corresponds to a limitation of the FFT analysis in a limited field range, and we therefore exclude it from our analysis. Due to their proximity, the peaks at 122 T and 135 T are hard to distinguish from each other. Using the Blackman window, which has the lowest secondary sidelobes and reduces the peak broadening in a finite field range, it is possible to identify these two nearby peaks, despite the finite field window. These two frequencies correspond to the two electron pockets also measured in S4 [Sykora et al., 2020b]. The peak at 168 T is smaller in amplitude, which might be due to a lower carrier mobility or a large effective mass. Together with the peak at 87 T, these frequencies correspond to the two hole pockets. This analysis gives the carrier densities of all four bands, which can then be fixed in the multi-band model discussed later. However, because the two electron pockets are very close to each other, a reasonable approximation is to consider an effective three-band model with a single electron pocket accounting for the two electron pockets expected by theoretical band calculation. This approximation describe the transport properties accurately.

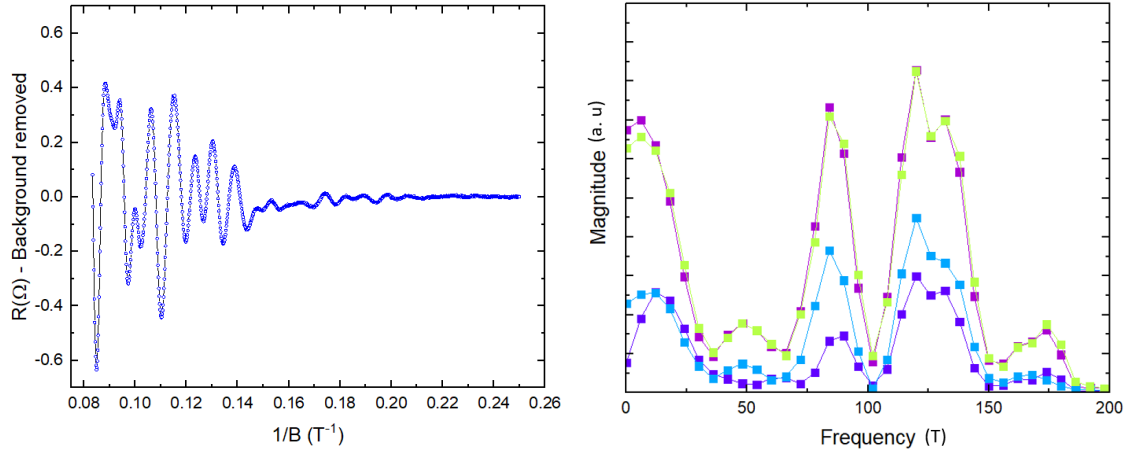


FIGURE 4.5: Left panel : Shubnikov-de Haas oscillations measured in the longitudinal resistivity of the sample S3, Right panel : FFT analysis of the different pairs of contacts for S3 using a blackman window, the green and purple curve corresponding to the oscillations of the longitudinal resistivity for a positive and negative magnetic field respectively, the blue and the dark purple curve, for two different pairs of Hall contacts and a positive magnetic field. Four peaks are clearly seen after the threshold due to the background, at 87, 122, 135 and 168 T.

The frequencies of the quantum oscillations are related to the cross section of Fermi surfaces \mathcal{A}_k in the k_{\parallel} plane, perpendicular to the applied magnetic field, by the Onsager relation :

$$f = \frac{h}{4\pi^2 e} \mathcal{A}_k = \frac{h}{4\pi e} k_{\parallel}^2 \quad (4.2)$$

where k_{\parallel} is the value of an effective in-plane Fermi wave vector assuming an isotropic in-plane band structure. In order to calculate the charge density associated to a given pocket, the value of the out-of-plane Fermi wave vector k_{\perp} is also required, assuming an ellipsoidal shape of the the Fermi pockets. However, k_{\perp} values cannot be inferred from magneto-transport measurements since no in-plane SdHO was measured. Following the approach developed by Sykora et al., we used band structure calculations to determine values of k_{\perp} and to calculate the carrier densities, for each band, for a fixed Fermi level deduced from the experimental k_{\parallel} values . For all samples studied, differences in k_{\parallel} are small, so that we use the value of k_{\perp} previously determined in [Sykora et al., 2020b] to calculate the four carrier densities.

The peak at 87 T corresponds to a small pocket of holes with a carrier density n_{h_1} of $4.82 \times 10^{18} \text{ cm}^{-3}$. The second hole pocket, much larger, has a carrier density n_{h_2} of $10.17 \times 10^{18} \text{ cm}^{-3}$. The two pockets of electrons have carrier densities close to each other at $n_{e_1} = 7.13 \times 10^{18} \text{ cm}^{-3}$ and $n_{e_2} = 7.89 \times 10^{18} \text{ cm}^{-3}$. As explained before, the small difference in electron carrier densities associated to the fact that these two electron pockets being close to another in the Brillouin zone [Ali et al., 2014], makes the approximation of a single electron band reasonable. The total carrier density is

obtained by adding the densities of the four pockets, taking into account their spins and valley degeneracies, g_s and g_v . The spin degeneracy in the band structure is lifted, so that $g_s = 1$, but a valley degeneracy remains with $g_v = 2$ for all pockets. This results in $n_e = g_s g_v n_{e1} + g_s g_v n_{e2} = 30.1 \times 10^{18} \text{ cm}^{-3}$ and $n_h = 2n_{h1} + 2n_{h2} = 30 \times 10^{18} \text{ cm}^{-3}$. This leads to a ratio n_e/n_h very close to unity, which confirms that the non-saturating behavior of the XMR in the studied magnetic field range is associated to a nearly perfect charge compensation. Finally, we remark that the values of carrier densities, inferred from the analysis of SdHO are in very good agreement with the densities extracted from the analysis of $\delta R/R_0$ within the framework of the two-band model (section 4.3.1).

4.3.3 Comparative study

To compare our samples, a plot of $\delta R(B)/R$ is shown in figure 4.6 on a logarithmic-logarithmic scale. For sample S5, the measurements were made up to 15 T, with a magnetoresistance of $1.2 \times 10^5 \%$ at 2 K. All five samples studied in this work show a subquadratic law B^α (with $\alpha < 2$), similar to other reports in the literature [Thoutam et al., 2015] [Wang et al., 2016b] [Fatemi et al., 2017] [Wang et al., 2019]. To have a relevant comparison, the fits were done between 1 T and 6 T. We notice that on a

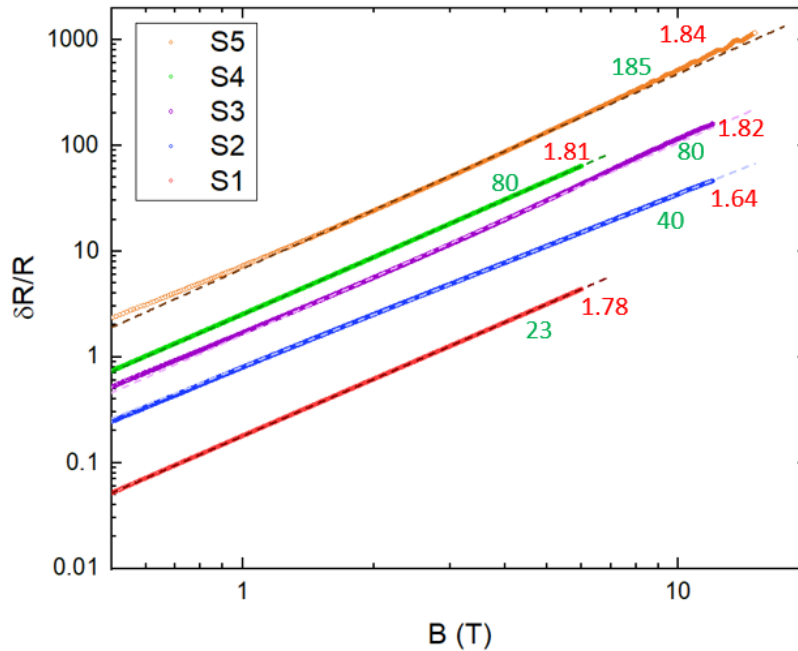


FIGURE 4.6: Magnetoresistance as a function of the magnetic field in logarithmic scale for five different samples, the RRR value for each sample is in green, the power law coefficient α is in red. The dashed lines are the power law fit made between 1 and 6 T associated to each magnetoresistance.

logarithmic-logarithmic scale, all the samples do not present a perfect power law behavior.

As seen in figure 4.6, there is no direct correlation between the RRR value and the exponent α of the power law, with a common value alpha ≈ 1.8 for all samples but S2. This value for α was also observed by others [Thoutam et al., 2015] [Wang et al., 2019], and our results show that this behavior is not directly related to the degree of disorder. Rather, this could be a signature of a multi-band transport, even for a perfect charge compensation.

4.4 Multi-band model

4.4.1 Formalism

As shown before, the two-band model fails to reproduce both the XMR and the Hall resistance, particularly in large magnetic fields, even if a deviation from perfect charge compensation is considered.

In order to take into account an arbitrary number of bands, we extend the two-band model to a more realistic n -band model with $n \in \mathbb{N}$ and $n \geq 2$. When n bands contribute to the transport, the total conductance tensor $\hat{\sigma}$ is the sum of all the $\hat{\sigma}_i$ of the different bands i :

$$\hat{\sigma} = \sum_i \hat{\sigma}_i = \sum_i \frac{(-1)^{v_i} \sigma_i}{1 + \mu_i^2 B^2} \begin{pmatrix} 1 & \mu_i B \\ -\mu_i B & 1 \end{pmatrix}, \quad (4.3)$$

where $v_i = 0$ for holes and $v_i = 1$ for electrons and $\sigma_i = en_i \mu_i$. The resistivity tensor is given by $\hat{\rho} = \hat{\sigma}^{-1}$ and, after some algebra, one can show that:

$$\rho_{xx} = \frac{\sum_i \sigma_i \prod_{j \neq i} (1 + \mu_j^2 B^2)}{\sum_i \left[\sigma_i^2 \prod_{j \neq i} (1 - \mu_j^2 B^2) + \sum_{j \neq i} \sigma_i \sigma_j (1 + (-1)^{v_i + v_j} \mu_i \mu_j B^2) \prod_{k \neq i, j} (1 + \mu_k^2 B^2) \right]}, \quad (4.4)$$

$$\rho_{xy} = B \frac{\sum_i (-1)^{v_i} \mu_i \sigma_i \prod_{j \neq i} (1 + \mu_j^2 B^2)}{\sum_i \left[\sigma_i^2 \prod_{j \neq i} (1 - \mu_j^2 B^2) + \sum_{j \neq i} \sigma_i \sigma_j (1 + (-1)^{v_i + v_j} \mu_i \mu_j B^2) \prod_{k \neq i, j} (1 + \mu_k^2 B^2) \right]}. \quad (4.5)$$

These expressions are complex polynomial fractions of the magnetic field and of microscopic parameters (carrier density n_i and mobility μ_i for each band i). They

can be written in the more compact form

$$\rho_{xx} = \frac{\sum_i a_i B^{2(i-1)}}{\sum_i c_i B^{2(i-1)}}, \quad (4.6)$$

$$\rho_{xy} = B \frac{\sum_i d_i B^{2(i-1)}}{\sum_i c_i B^{2(i-1)}}, \quad (4.7)$$

where the a_i, c_i and d_i are complex functions of the mobility, the charge density and the index v_i of each band. The numerator of ρ_{xx} and the common denominator of ρ_{xx} and ρ_{xy} are polynomials with only even orders of B whereas the numerator of ρ_{xy} has only odd orders of B . Despite their complexity, the coefficients corresponding to the low field limit (a_1, c_1 and d_1) and the high field limit (a_n, c_n and d_n) can be easily extracted out of Eq. (4.4) and Eq. (4.5). We have

$$a_1 = \sum_i \sigma_i, \quad (4.8)$$

$$c_1 = \left(\sum_i \sigma_i \right)^2, \quad (4.9)$$

$$d_1 = \sum_i (-1)^{v_i} \mu_i \sigma_i, \quad (4.10)$$

$$a_n = e \left(\sum_i \frac{n_i}{\mu_i} \right) \left(\prod_i \mu_i^2 \right), \quad (4.11)$$

$$c_n = e^2 \left(\sum_i (-1)^{v_i} n_i \right)^2 \left(\prod_i \mu_i^2 \right), \quad (4.12)$$

$$d_n = e \left(\sum_i (-1)^{v_i} n_i \right) \left(\prod_i \mu_i^2 \right). \quad (4.13)$$

As a result, in the fully compensated case (i.e. $\sum_i (-1)^{v_i} n_i = 0$), the coefficient c_n and d_n vanish and the longitudinal magnetoresistivity shows a quadratic behaviour at very large field with no saturation whereas the Hall magnetoresistivity follows a linear behaviour. In the low field limit, we have $\rho_{xx} \propto (\sum_i \sigma_i)^{-1}$.

4.4.2 From a two-band to a three-band model

Before we consider this model applied to two hole bands and a single average electron band, let us briefly discuss the deviation from the quadratic behavior in the two-band model. In this model, a deviation from the full compensation can result in both the subquadratic longitudinal MR and the non-linear Hall resistivity. However, these magnetic field dependences do not reproduce the experimental results. For

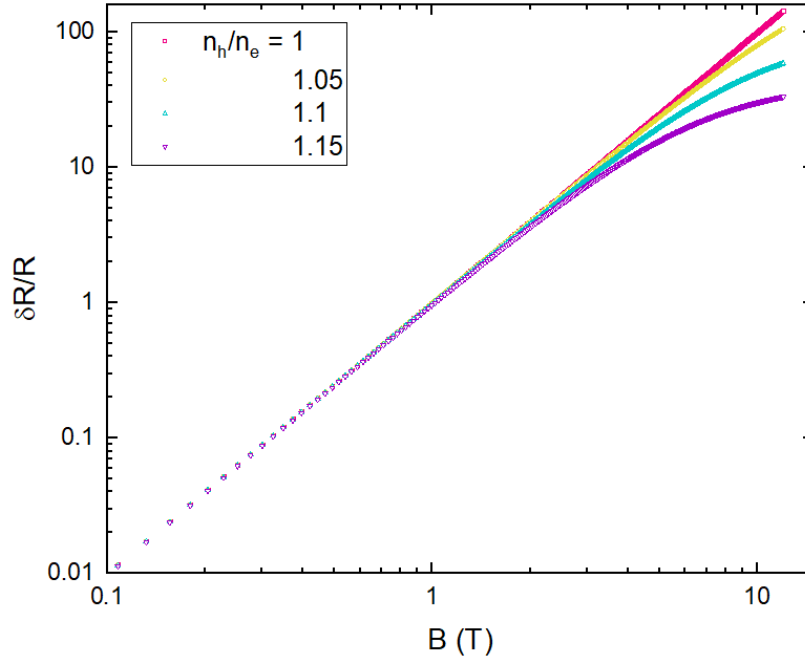


FIGURE 4.7: Longitudinal resistivity as a function of a perpendicular magnetic field in a two-band model for different ratio n_h/n_e . We took $\mu_h = \mu_e = 1 \text{ m}^2/\text{V.s}$ and shift the carrier densities starting from $n_h=n_e=3 \times 10^{19} \text{ cm}^{-3}$.

instance, the magnetoresistance does not follow a power law dependence for a non compensated system in the two-band model. As an example, let us consider first the simple case $\mu_e=\mu_h$. For a ratio n_h/n_e different from unity, the longitudinal MR follows a quadratic behavior until the term in B^2 at the denominator becomes dominant. This crossover from a quadratic behavior at low fields to a saturation at high magnetic fields happens at :

$$B_{sat} = \frac{1}{\mu} \left| \frac{n_e + n_h}{n_e - n_h} \right| \quad (4.14)$$

and can be associated with a continuous evolution of the value of $\alpha(B)$ that progressively decreases from the value $\alpha = 2$ (figure 4.7) to $\alpha = 0$ at $B > B_{sat}$. This situation is clearly different from the subquadracity with a constant power-law exponent over a broad magnetic field range, as observed in the majority of the studies of WTe_2 . We also remark that studies of WTe_2 using an electrostatic gate reported such a subquadratic law even at the perfect compensation [Wang et al., 2019]. Therefore, the two-band model fails to reproduce the subquadratic XMR as well as the Hall magnetoresistance.

Using the three-band model, our analysis gives some more quantitative information. In order to get rid of any issues related to the geometry of the sample, we again consider the $\delta R(B)/R_0$ instead of $R(B)$ below. To reproduce the subquadratic behavior, it is possible to tune the three mobilities focusing first on the longitudinal

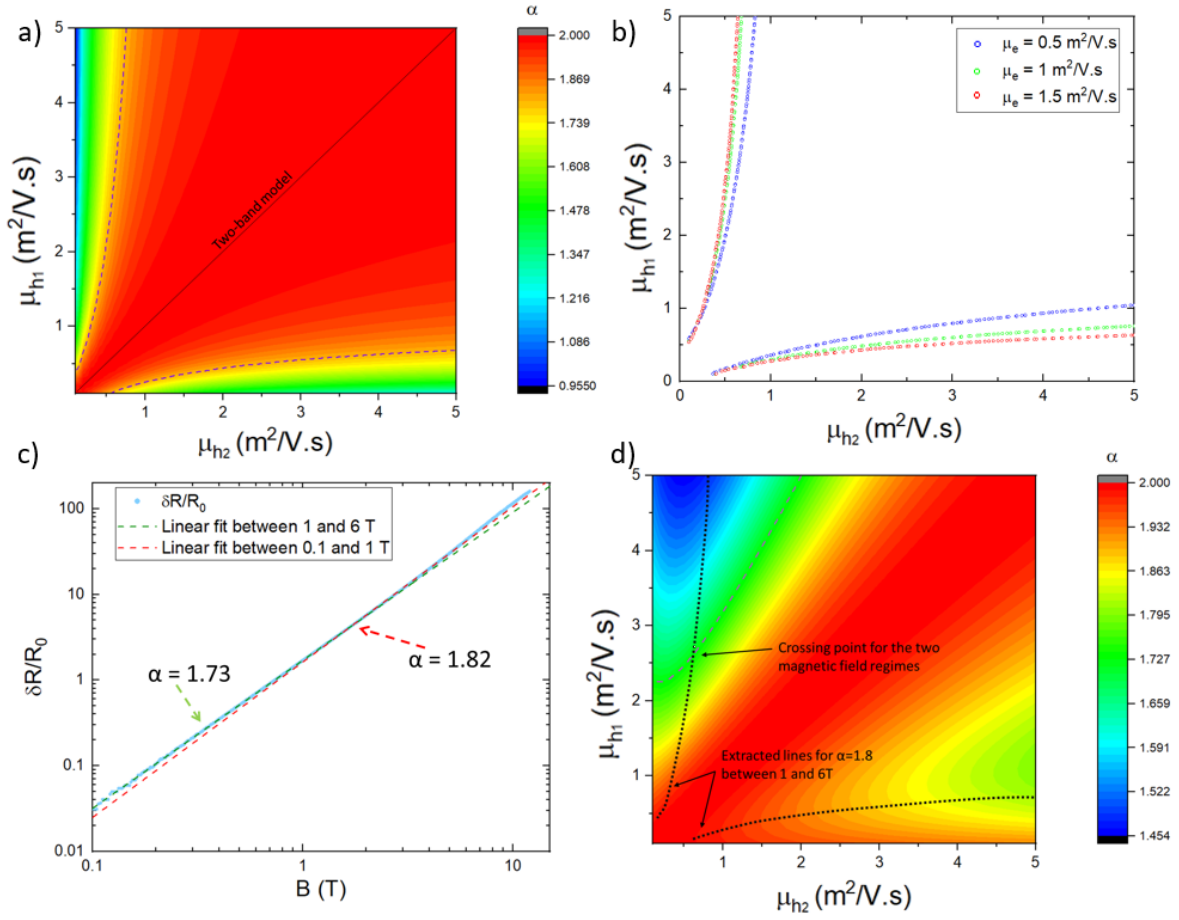


FIGURE 4.8: In the framework of a three-band model : a) mapping of the power law exponent α , extracted from a linear fit with B in the range of 1 to 6 T, and for the mobility of the electron band fixed at $1 \text{ m}^2/\text{V.s}$, as a function of the two hole mobilities. We used $n_e = 3.01 \times 10^{19} \text{ cm}^{-3}$, $n_{h_1} = 9.64 \times 10^{18} \text{ cm}^{-3}$ and $n_{h_2} = 2.03 \times 10^{19} \text{ cm}^{-3}$. The purple dashed line correspond to a power law of 1.8. b) Contour lines for a power-law exponent $\alpha = 1.8$ between 1 and 6 T, as calculated for three different values of the average electron mobility $\mu_e = 0.5, 1$ and $1.5 \text{ m}^2/\text{V.s}$; c) $\delta R(B)/R_0$ as a function of the magnetic field on a logarithmic-logarithmic scale for two linear fits, between 0.1 and 1 T giving a power law of 1.65 and between 1 and 6 T giving a power law of 1.82; d) Mapping of the power law exponent α , extracted from a linear fit with B in the range of 0.1 to 1 T, and for the mobility of the electron band fixed at $1 \text{ m}^2/\text{V.s}$, as a function of the two hole mobilities, the carrier densities being the same as for a). The purple dashed line correspond to a power law of 1.65 and extracted points from the contour line of a) show a crossing point corresponding to fit parameters for the longitudinal magnetoresistivity.

MR only in the fully compensated three-band model and fixing the values of the different carrier densities to those inferred from the previous analysis of SdH oscillations. A systematic determination and mapping of the power law exponent as a function of the hole mobilities can be done by fixing the electron mobility and by calculating the magnetoresistance in the three-band model between 1 and 6 T for different values of the hole mobilities and by fitting the result to a power law. Since we are considering $\delta R(B)/R_0$ and not R , this method is straightforward.

Indeed, $\delta R(B)/R_0$ is a function of $n_e, n_{h_1}, n_{h_2}, \mu_{h_1}/\mu_e, \mu_{h_2}/\mu_e$ and $B\mu_e$, but μ_e can be fixed to any arbitrary value, with little influence on the power-law exponent since it mainly acts as a scaling factor to the magnetic field. As shown in figure 4.8 a), the power law is either quadratic or subquadratic if the hole mobilities are respectively similar or very different. The two purple dashed lines in the graph correspond to a power-law exponent $\alpha = 1.8$, measured roughly in our samples. As shown on figure 4.8 b), little influence of the mobility μ_e on the power law coefficient is observed. Nevertheless, from this analysis, a full set of possible pair of (μ_{h_1}, μ_{h_2}) that give an exponent α in good agreement with the experimental data is now possible. To reduce this list, it is possible to fit the low magnetic field part, $B < 1$ T of the $\delta R(B)/R_0$ (figure 4.8 c)) and calculate the exponent α for this range of the magnetic field (4.8 d)). This approach allows us to determine which hole band has the largest mobility (in the sample S3, the hole band with the small carrier density) and to have approximate values for the different mobilities by considering now the only pair that corresponds to the crossing point of the exponent in the low field regime and the one in the large field limit ($1 \text{ T} < B < 6 \text{ T}$). This fit based on a three-band model and taking carrier densities inferred from Shubnikov-de Haas oscillations, reproduces the XMR very well for $\mu_{h_1} = 2.55 \text{ m}^2/\text{V.s}$ and $\mu_{h_2} = 0.55 \text{ m}^2/\text{V.s}$, the mobilities corresponding to the crossing point in figure 4.9, and that reproduce very well the power law behavior taking $\mu_e = 1.2 \text{ m}^2/\text{V.s}$ to fit the data $\delta R(B)/R_0$ at best.

Up to this point, we have neglected the information given by the Hall signal. From an experimental point of view, we note that the penetration of the contact in the flake might be responsible for a reduction of the measured Hall voltage due to

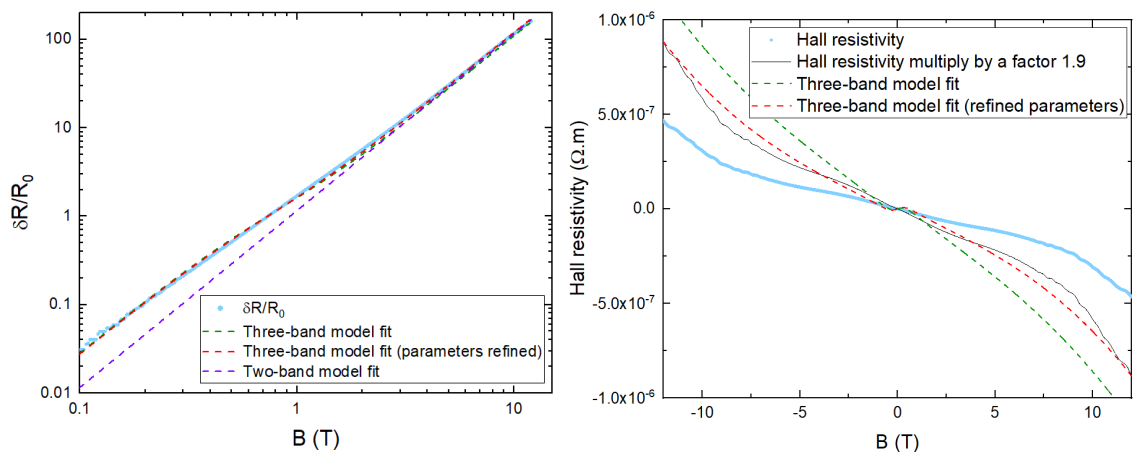


FIGURE 4.9: Three-band model fit for the relative magnetoresistance and the Hall resistivity of the sample S3 with $n_e = 3.01 \cdot 10^{19} \text{ cm}^{-3}$, $\mu_e = 1.15 \text{ m}^2/\text{V.s}$, $n_{h_1} = 9.64 \cdot 10^{18} \text{ cm}^{-3}$, $\mu_{h_1} = 2.6 \text{ m}^2/\text{V.s}$, $n_{h_2} = 2.034 \cdot 10^{19} \text{ cm}^{-3}$, $\mu_{h_2} = 0.65 \text{ m}^2/\text{V.s}$. The data are in blue and the fits correspond to the red dashed line. A multiplication of the Hall resistivity by a factor 1.9 was also done to better compare the fit to the data.

current that flows in the contacts so that only qualitative comparison can be done. Hence, the three-band model taking the carrier densities extracted from the SdHO and considering the triplet of mobilities deduce previously from the longitudinal resistivity analysis leads to a difference in amplitude with the experimental data, likely due to the penetration of the contacts. Nevertheless, the shape of the Hall resistivity curve and the three-band model fit show qualitative agreement. It is even possible to refine the mobilities found above to better fit the shape of the Hall, keeping a very good agreement for $\delta R(B)/R_0$. Best agreement is found for $\mu_e = 1.15 \text{ m}^2/\text{V.s}$, $\mu_{h_1} = 2.6 \text{ m}^2/\text{V.s}$ and $\mu_{h_2} = 0.65 \text{ m}^2/\text{V.s}$. A multiplication of the Hall resistivity measured by a factor 1.9 in order to adjust the amplitude of the experimental data to the three-band model shows that the agreement between the two is not perfect and that four bands are probably needed to have a better agreement. Nevertheless, the three-band model is able to reproduce very accurately the magnetoresistance and its different power law regimes over a broad range of magnetic fields and even for charge densities that are fixed by the SdHO. Our analysis clearly shows that such a behavior can be related to a difference in the two hole-carrier mobilities.

In the next section, numerical simulations are used to go beyond the three-band model and relate the power law coefficient directly to the microscopic nature of the disorder. Interestingly, and contrary to experimental studies, numerical simulations allow us to investigate independently the influence of the amplitude of the disorder and of its correlation length on the magnetoresistance and more particularly on the deviation to the quadraticity in the almost compensated regime.

4.5 Numerical simulations

Our experimental results can be compared with the results of numerical simulations considering the exact band structure of WTe_2 . This method was already presented in our previous work where we focused on different transport properties such as the transport time and the quantum life of the quasi-particles [Sykora et al., 2020b]. New comparison of the calculated MR with our data sheds light on the role of the disorder on the XMR.

4.5.1 Projective renormalization method

As already mentioned before, numerical simulations considering both a disordered structure and the exact band structure of WTe_2 should be able to reproduce and capture most of the transport properties at low temperature. In this context, a fruitful collaboration with the theoretician Steffen Sykora (TU Dresden) allows us to calculate

the different transport properties of WTe₂ from the Weyl Hamiltonian solved using the projective renormalization method that was used already in a prior work [Sykora et al., 2020a]. The band structure model is taken from first principle calculation [McCormick et al., 2017]. In this subsection, we detail the method used to calculate the different transport quantity that are reported in the next subsection.

We first consider a minimal Hamiltonian of a disordered Weyl semimetal [McCormick et al., 2017] with two terms, one corresponding to a Weyl Hamiltonian, the other to a finite disorder in momentum space.

$$\mathcal{H} = \sum_{k,\alpha,\beta} c_{k,\alpha}^\dagger [\hat{H}_k]_{\alpha,\beta} c_{k,\beta} + \sum_{k,k',\alpha,\beta} (c_{k,\alpha}^\dagger [\hat{V}_{k,k'}]_{\alpha,\beta} c_{k',\beta} + h.c.) \quad (4.15)$$

where $c_{k,\alpha}^{(\dagger)}$ are annihilation (creation) operators of an electron at momentum k in an orbital α . The term \hat{H}_k corresponds to the kinetic energy that can be written :

$$\hat{H}_k = \sum_{i=0,1,2,3} \epsilon_{i,k} \hat{\sigma}_i \quad (4.16)$$

with $\hat{\sigma}_i$ the i th Pauli matrix for $i = 1,2,3$ whose indices correspond to an orbital degree of freedom and $\hat{\sigma}_0$, the 2×2 identity matrix. If such an Hamiltonian has at least two points around which the Hamiltonian is described locally by :

$$\hat{H}_{WP}(k) = \sum_{i=1,2,3} \gamma_i k_i \hat{\sigma}_0 + \sum_{i,j=1,2,3} k_i A_{i,j} \quad (4.17)$$

it describes a Weyl semimetal with nodes of chirality $\Xi = \det(A_{ij})$.

The scattering by disorder is introduced in the second term by a gaussian correlated scalar disorder such that :

$$[\hat{V}_{k,k'}]_{\alpha,\beta} = \delta_{\alpha,\beta} V e^{-2\xi^2 |k-k'|^2} \quad (4.18)$$

From that, the Weyl Hamiltonian including the band structure need to be diagonalized. New fermion operators are introduced to diagonalize the Weyl Hamiltonian without disorder and the eigenenergies associated to these new operators include all the information related to the band structure.

$$a_{k,\alpha} = \sum_{\beta} [\hat{D}_k]_{\alpha,\beta} c_{k,\beta} \quad (4.19)$$

The Hamiltonian is then treated in two part, an unperturbed part \mathcal{H}_0 and a perturbation \mathcal{H}_1 :

$$\mathcal{H} = \mathcal{H}_0 + \mathcal{H}_1 = \sum_{\alpha} E_{k,\alpha} a_{k,\alpha}^\dagger a_{k,\alpha} + \sum_{k,k',\alpha,\beta} (a_{k,\alpha}^\dagger [\hat{D}_k \hat{V}_{k,k'} \hat{D}_{k'}^{-1}]_{\alpha,\beta} a_{k',\beta} + h.c.), \quad (4.20)$$

the first term is containing the band structure component while the second term is the effective scattering between the bands. As explained above, \mathcal{H}_0 is diagonal in the base constituted by the new fermion operators. Then, the projective renormalization method is applied : the scattering term is integrated by unitary transformation in order to write \mathcal{H} as an effective diagonal Hamiltonian $\tilde{\mathcal{H}}$ where $\tilde{\mathcal{H}}$ and \mathcal{H} are related together through the unitary transformation :

$$\tilde{\mathcal{H}} = e^X \mathcal{H} e^{-X} = \sum_{\alpha} \tilde{E}_{k,\alpha} \tilde{a}_{k,\alpha}^{\dagger} \tilde{a}_{k,\alpha} \quad (4.21)$$

$$\text{with } \tilde{a}_{k,\alpha}^{\dagger} = e^X a_{k,\alpha}^{\dagger} e^{-X} \quad (4.22)$$

defining the new fermions operators and X being the generator that satisfies $X^{\dagger} = -X$. X can be related to the $a_{k,\alpha}$ operators as well as to the eigenvalues of the non disordered system \mathcal{H}_0 and to the disorder by :

$$X = \sum_{k,k',\alpha,\beta} (a_{k,\alpha}^{\dagger} A_{k,k'}^{\alpha,\beta} a_{k',\beta} - h.c.) \quad (4.23)$$

$$\text{with } A_{k,k'}^{\alpha,\beta} = \frac{1}{2} \arctan\left(\frac{2[\hat{V}_{k,k'}]_{\alpha,\beta}}{E_{k,\alpha} - E_{k',\beta}}\right) \quad (4.24)$$

The important point is that since \mathcal{H} and $\tilde{\mathcal{H}}$ are connected through a unitary transformation, they have the same eigenvalues. Therefore, any transport property can be calculated equivalently from \mathcal{H} or $\tilde{\mathcal{H}}$ (since in principle $\langle a_{k,\alpha}^{\dagger} a_{k',\beta} \rangle_{\mathcal{H}} = \langle \tilde{a}_{k,\alpha}^{\dagger} \tilde{a}_{k',\beta} \rangle_{\tilde{\mathcal{H}}}$). We hence take advantage of the diagonal nature of $\tilde{\mathcal{H}}$ to determine the transport properties such as the conductivity σ_{xx} of the material as well as any other transport parameters. σ_{xx} is related to the current density operator j_x and so to the $\tilde{a}_{k,\alpha}$ operators through :

$$j_x = \frac{1}{V} \sum_{\alpha} \sum_{k,q} e^{iqx} \frac{\hbar k}{m} \tilde{a}_{k-\frac{q}{2},\alpha}^{\dagger} \tilde{a}_{k+\frac{q}{2},\alpha} \quad (4.25)$$

$$\sigma_{xx} = \langle j_x j_x \rangle = \frac{\text{Tr}(j_x j_x e^{-\beta \tilde{\mathcal{H}}})}{e^{-\beta \tilde{\mathcal{H}}}} \quad (4.26)$$

with $\beta = k_B T$ (k_B being the Boltzmann constant), term that capture the temperature dependence of the resistivity. For the case of the magnetic field dependence, a Zeeman term is added in the Hamiltonian and another diagonalization process is done that defines new fermion operators that depend now on the magnetic field.

4.5.2 Results

In the three-band model analysis previously discussed, we evidenced that the sub-quadratic law finds its origin in the large difference of the carrier mobilities among the different pockets. Besides, we also showed that the power-law exponent can be nearly field-independent on some large field range, but also that it can vary at small or high fields, as a consequence of multi-band transport. To better understand these specific properties, the results are compared to numerical calculations considering tunable parameters of the scattering potential (amplitude, correlation length).

These calculations lead us to determine the exponent of the power-law as a function of the amplitude of the disorder V and its correlation length ξ . As shown in figure 4.10, the exponent of the power-law α is showing some non-monothonic behavior as a function of the parameters of the potential disorder, the quadratic law being recovered for both very large or very small amplitudes and correlation lengths. In the multi-band model, a change in the power law is expected when the quadratic field contribution becomes larger than one in the $1+\mu_i^2 B^2$ terms of the numerator of the longitudinal resistivity (Eq. 4.4) or when a given term of the polynomial of the denominator dominates over the other terms in Eq. 4.6. If these conditions are easily related to a simple expression of the magnetic fields for the numerator ($B = 1/\mu_i$), the change of slope due to the denominator corresponds to a magnetic field that is related

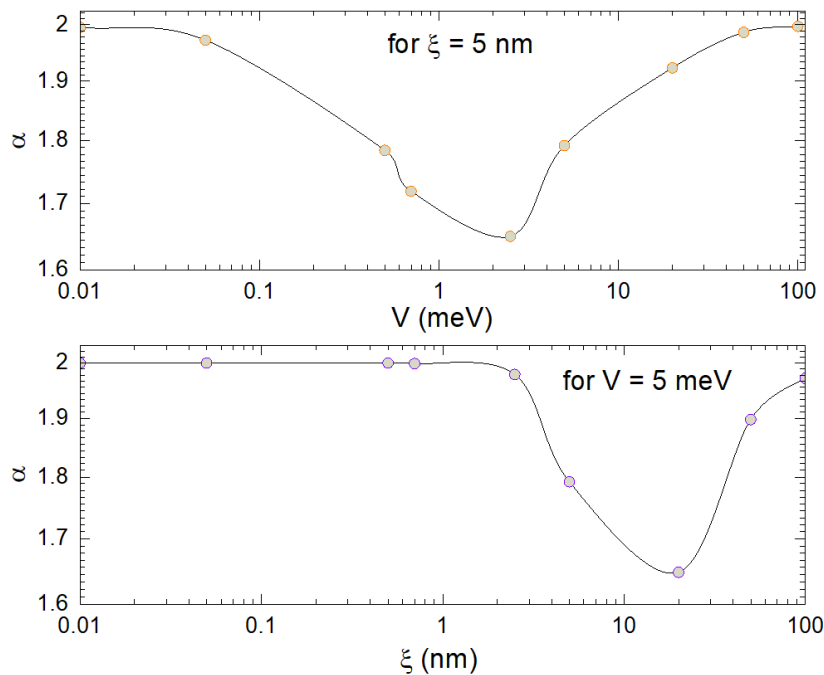


FIGURE 4.10: Coefficient α of the power-law, top : as a function of the amplitude of the disorder for a correlation length $\xi = 5$ nm; bottom : as a function of the correlation length of the disorder for an amplitude of the disorder $V = 5$ meV. The line is a guide for the eye.

to the c_i coefficient in Eq. 4.6 and is therefore a complex function of the different mobilities and densities. Nevertheless, in the three-band model and assuming a full compensation, we can easily determine the different terms of the denominator and we have :

$$\begin{aligned}
c_1 &= (\sigma_{h_1} + \sigma_{h_2} + \sigma_e)^2 \\
c_2 &= (\mu_{h_1}\sigma_{h_2} + \mu_{h_2}\sigma_{h_1})^2 + (\mu_{h_1}\sigma_e - \mu_e\sigma_{h_1})^2 \\
&\quad + (\mu_{h_2}\sigma_e - \mu_e\sigma_{h_2})^2 + 2\sigma_{h_1}\sigma_{h_2}\sigma_e \left(\frac{\mu_e^2}{\sigma_e} - \frac{\mu_{h_1}^2}{\sigma_{h_1}} - \frac{\mu_{h_2}^2}{\sigma_{h_2}} \right) \\
c_3 &= 0 \quad (\text{full compensation})
\end{aligned}$$

where $\sigma = en\mu$ is the conductivity of a given pocket. Therefore, the quadratic term will take over the constant term for :

$$B^* \geq \frac{\sigma_{h_1} + \sigma_{h_2} + \sigma_e}{\sqrt{c_2}} \quad (4.27)$$

In the full compensated three band model, changes in the exponent of the magnetoresistance power law take place at $B = 1/\mu_{h_1}, 1/\mu_{h_2}, 1/\mu_e$ and $B = B^*$. This will result in the presence of singularities in the logarithmic-logarithmic representation of the MR with the appearance of different power-law regimes. Because all the charge pockets have parameters of the same order of magnitude these different power law regimes overlap each other and the change in the power law exponent remains rather small.

Hence for a very small disorder, we have $B \gg 1/\mu_i$ and $B \gg B^*$, the higher order terms dominate both the numerator and the denominator for small magnetic field leading to a quadratic behavior. In the case of a very large disorder and considering the expanded form of the longitudinal resistivity, the magnetic field terms of higher order become negligible and only the MR is given by the B^2 term of the numerator.

In the strong disorder regime (large disorder amplitude or short correlation length), we note that the multi-band model might not be valid anymore. Indeed, this approach assumes that the different bands are independent and not coupled to each other. This requires that intraband scattering strongly dominates over interband scattering, an assumption that is not satisfied in the strong disorder regime. Interestingly, numerical simulations that include interband scattering, show that in the strong disorder regime, a quadratic power law is recovered as in the simple case of a two-band structure. Finally, between the weak and strong disorder regime, a deviation from

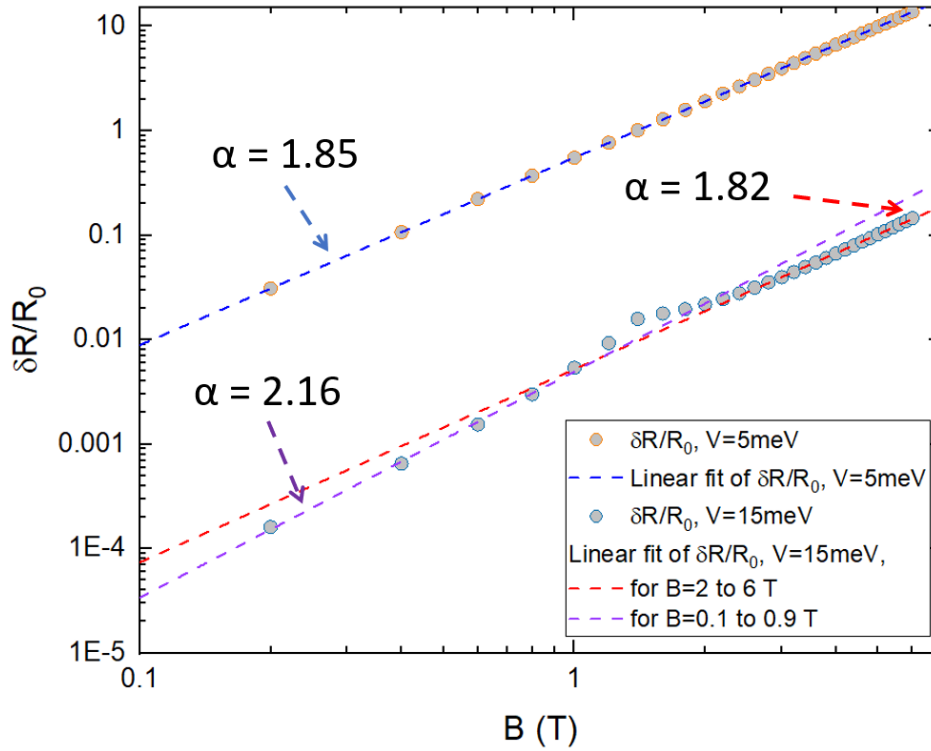


FIGURE 4.11: Numerical calculations of the XMR for two different disorder, orange circle corresponding to an XMR with $\zeta = 5$ nm and $V = 5$ meV and blue circle with $\zeta = 5$ nm and $V = 15$ meV. The dashed lines are their respective fits.

the quadratic behavior is hence expected and observed with a power-law minimum of around 1.6 for both $V = 25$ meV and $\zeta = 5$ nm or for $V = 5$ meV and $\zeta = 20$ nm.

Hence, two different pairs of ζ and V can be found for a power law with $\alpha = 1.8$, that corresponds to the different degrees of disorder in S1 and S3. Focusing on S1, S2 and S3 and fixing one of the microscopic parameters ζ or V , it is possible to qualitatively describe the nature of the disorder by considering the RRR value. Fixing for instance ζ , S5 can be described by the smallest amplitude of the disorder, whereas S3 and S4 (same RRR) correspond to a larger amplitude. Larger values are found for S2 and S1, in agreement with their RRR values (reduced mobilities). This analysis leads us to finally understand the relation between the RRR and the power-law exponent and, in this case to explain why the sample S2, showing a RRR between S1 and S4 leads to a power law smaller than the two other samples.

The complexity of the relation between the disorder and the magnetoresistance is illustrated in figure 4.11, where it is possible to see on a logarithmic-logarithmic scale, a perfectly linear fit between 0.1 and 6 T for a subquadratic law with $\zeta = 5$ nm and $V = 5$ meV while another type of disorder ($\zeta = 5$ nm and $V = 15$ meV), leads to clear deviation from the power-law behavior with two behaviors clearly identified in this magnetic field range. This echoes our experimental data, and shows that

numerical simulations even reveal some power-law behavior with an exponent larger than 2 over a restricted magnetic field range. Finally, for some parameters values, we note that numerical simulations show, in agreement with experimental data, very accurate subquadratic power-law over a surprisingly large magnetic field range that might be not related to the multiband nature of the transport but rather to a subtle effect implying a renormalization of the band structure by the magnetic field and the disorder. This point still needs to be better understood and is the subject of current investigations.

4.6 Conclusion

In this chapter, we showed that the two-band model was not accurate enough to do quantitative analysis of the transport properties in WTe_2 . More precisely, it does not consider the carrier densities extracted from Shubnikov-de Haas analysis and does not succeed to reproduce the subquadratic law of the extremely large magnetoresistance. A comparison study between the different samples grown by different techniques allowed us to compare the RRR and the power law exponent and to highlight that there is no simple relation between the RRR and the power-law exponent. Numerical simulations allow us nevertheless to qualitatively understand the effect of the disorder on the subquadratic behavior.

We developed a multi-band model and we used the approximation of a three-band model, assuming hence that the two electron pockets have carrier mobilities and densities very similar as it is expected since their positions are very close to each other in the Brillouin zone. From this approximation, the transport properties of the system were analysed with two hole bands and one electron band, taking the carrier densities extracted from Shubnikov-de Haas. This approach succeeds to reproduce the subquadratic law that is originating in a significant difference between the mobilities of the two hole bands. Moreover, although the Hall resistance was not quantitatively reproduced likely due to the contact geometry, a good qualitative agreement could be found between the three-band model fit for the same parameters used for the longitudinal MR and therefore taking the carrier densities inferred from SdHO analysis. Finally, numerical simulations allow us to unveil the non-trivial relation between the nature of the disorder and the magnetoresistance in particular, the non-monothonic behavior of the power-law exponent as a function of ζ and V .

TOPOLOGY AND TRANSPORT PROPERTIES AT VERY LOW TEMPERATURE

5.1 Motivation

In the search of Weyl physics signatures, the negative longitudinal magnetoresistance (NMR) has been the focus of many studies. Indeed, the NMR could result from the chiral anomaly, which is due to an imbalance in the number of particles of each chirality in a Weyl semimetal. Yet, as already mentioned in chapter 2, the negative longitudinal magnetoresistance can also appear due to current jetting. Due to the Weyl type-II nature of WTe_2 , the chiral anomaly is expected to be anisotropic and to depend on the current direction with respect to the crystal orientation [Soluyanov et al., 2015]. Indeed, an anisotropic NMR has been reported in experiments, appearing with an electric field and magnetic field in the b-axis direction only [Wang et al., 2016a][Li et al., 2017b]. It was also predicted [Sharma et al., 2017] and experimentally reported [Lv et al., 2017] that in the classical regime ($\mu B \ll 1$), this chiral anomaly can become isotropic, that is, with no difference if the colinear electric and magnetic fields are applied along either the a-axis or the b-axis. Nevertheless, in these experimental studies, the presence of a large magnetoresistance attributed to a charge compensation raises the question of the position of the Fermi level with respect to the Weyl nodes. Indeed, the regime of charge compensation implies that the Weyl nodes are located at 52 and 58 meV above the Fermi level, which casts strong doubts about the possible influence of the chiral anomaly mechanism on transport properties. Furthermore, it was recently shown that disorder induces some significant interband scattering between two Weyl nodes or between topological and trivial bands [Sykora et al., 2020b]. Such a coupling is expected to strongly reduce the amplitude of signatures related to the chiral anomaly in transport measurements.

In this chapter, we report on a detailed study of the magneto-transport properties at very low temperatures, in the sub-Kelvin range. Remarkably, a resistivity upturn is evidenced below 4 K, which comes along with an isotropic negative longitudinal magneto-resistance at low fields. This behavior was reproduced in all the nanostructures measured (S1, S2, S3 and S4) and applying the magnetic field in all directions using a 2T-sphere 3D vector magnet (in-plane orientation parallel to the current, in-plane orientation perpendicular to the current and out-of-plane orientation). The isotropic nature of the NMR was further confirmed by a complete 2D mapping with an in-plane magnetic field for sample S1. These experimental results are well reproduced by numerical simulations based on the exact band structure of WTe_2 , which allows us to identify a novel mechanism for the NMR due to the band structure topology, as a signature of high-energy Weyl fermions, when the Fermi energy lies far away from the Weyl nodes.

5.2 Low-field transport properties

5.2.1 In-plane Magnetoresistance at 4.2K

At 4.2 K, the three samples show a large MR for a magnetic field applied out-of plane, which corresponds to the XMR, discussed in Chapter 4. Due to this large response, some special care was taken for in-plane measurements, so as to reduce misalignment effects. Furthermore, since the XMR has nearly no more temperature dependence

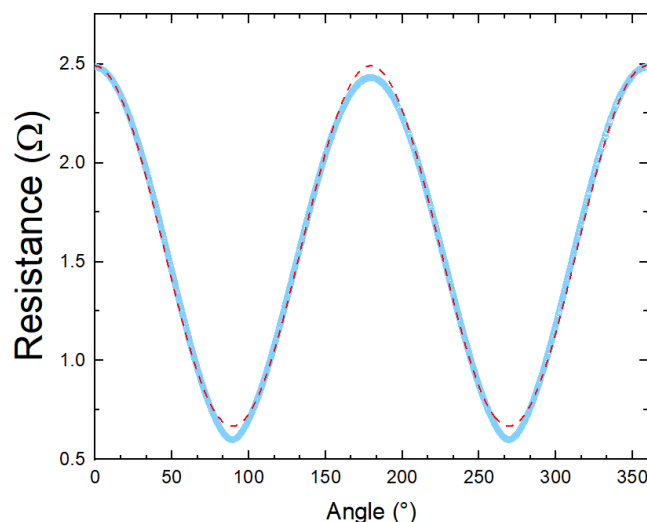


FIGURE 5.1: Angular dependence of the resistance for sample S3, measured at $T = 4.2$ K and with a 2 T magnetic field rotated from the out-of-plane orientation ($\theta = 0^\circ$) to an in-plane direction ($\theta = 90^\circ$). A fit with a sine function in red dashed line is used to determine the angular shift corresponding to the misalignment.

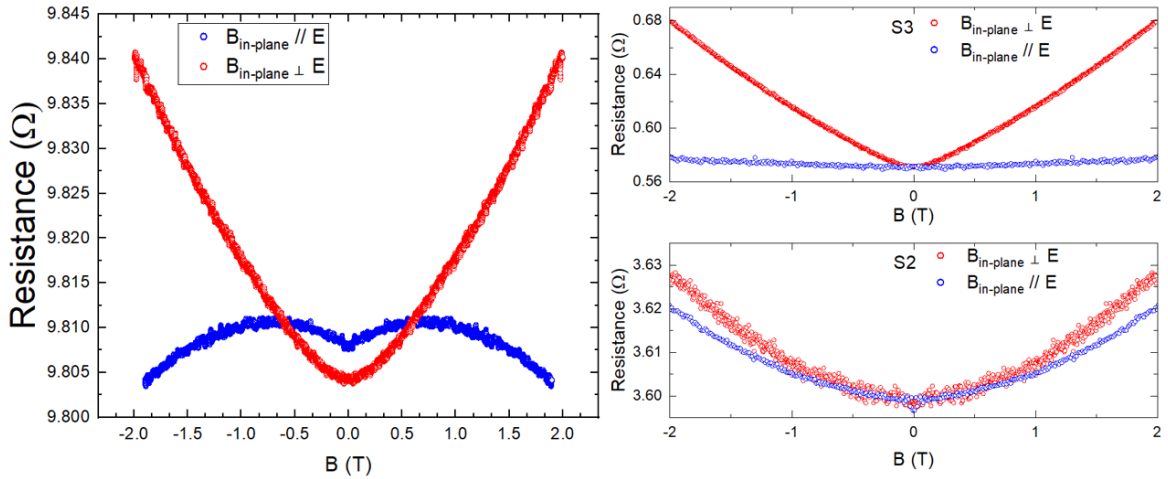


FIGURE 5.2: In-plane magneto-resistance of samples S1, S2 and S3, as measured at $T = 4.2$ K for a current $I = 10 \mu\text{A}$

below 4.2 K and because at this temperature the low-field NMR is vanishingly small, the XMR contribution could be easily removed by subtracting this measurement from our data at very low temperature. This allows us to reveal an effect that remains several orders of magnitude smaller than the XMR. The misalignment between the sample normal and the perpendicular field could be identified by rotating the magnetic field around one of the in-plane axis and analysing the cosine dependence, a misalignment of less than 5° could be identified depending on the axis and of the sample (figure 5.1).

The in-plane magnetoresistance of our samples at 4.2 K is presented in figure 5.2. In this figure, the in-plane magnetoresistance is very small as compared to the out-of-plane magnetoresistance. Nevertheless, a negative MR is clearly observed in the in-plane configuration, when the magnetic field is applied parallel to the electric field. Due to its small amplitude, the careful sample alignment is necessary to unveil this contribution. A deeper analysis of this negative magnetoresistance at very low temperature, where this effect is orders of magnitude larger, will be made in the next section.

Even for a good alignment, when the in-plane magnetic field is applied perpendicular to the current, our three samples all show different amplitude of the magnetoresistance. A small misalignment leading to an out-of-plane component of the MR could be invoked for the samples S1 and S2 since the MR is almost quadratic. However, the strong linear behavior of the MR of S3 can not be ascribed to an XMR component due to such a small misalignment. More quantitatively, the positive MR can be fitted with a power law B^α with $\alpha = 1.15$. Such a power law was already reported by others [Zhao et al., 2015], but its origin remains elusive. Song and al

attributed for instance a linear MR to the presence of a smooth disorder for materials with large carrier mobilities [Song et al., 2015]. Nevertheless, our numerical simulations were not able to reproduce this power law dependence of the in-plane positive MR at $T = 4.2$ K.

5.2.2 Very low temperature dependence of the longitudinal resistance

By cooling further the nanostructures in a dilution fridge, an upturn in the resistance appears at around $T \approx 4$ K. As shown in figure 5.3, the resistance increases between 7 to 14 % between 4 K and 100 mK depending on the sample. The gap in the different curves is due to the difficulty to stabilize the temperature in the range 850-1200 mK with the ^3He - ^4He dilution refrigerator.

In order to avoid any temperature gradient between the thermometer and the sample, we compared the resistance of S1 measured during the cooldown with some measurements realized using a temperature stabilization. With this method, the sample is first cooled down to the base temperature ($T = 100$ mK) temperature where it stabilizes during a significant time in order to reach the electronic base temperature. Then, the temperature of the sample is increased in steps of 100 mK and at each temperature, we wait until a stable state is reached (10 mn). Finally, we measure the sample resistance with respect of time and average the value of the resistance over the last 30 points to further decrease the error bar. This allow us to have a time equilibrium measurement of the resistance. On the measurements of sample S1, a large noise appeared between 600 and 800 mK due to some temperature instabilities

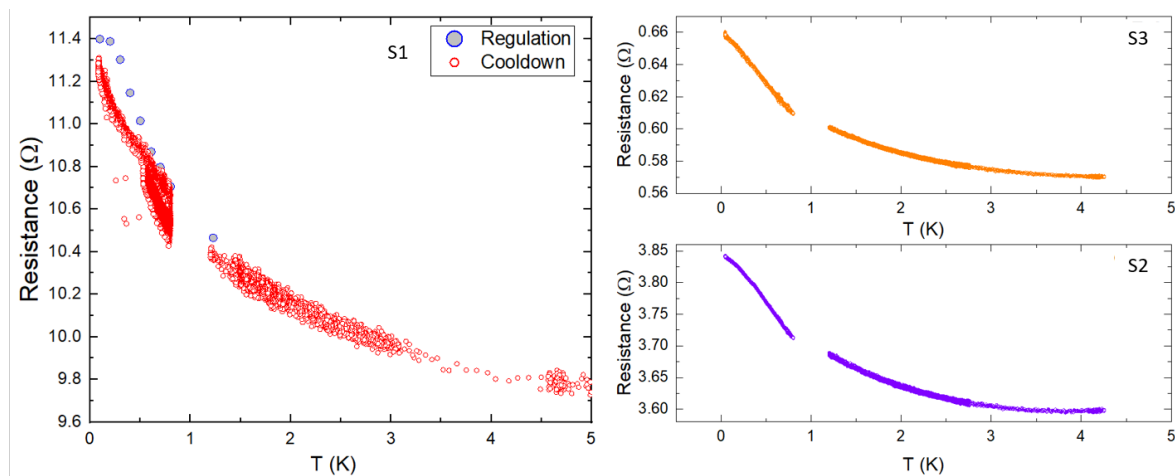


FIGURE 5.3: Temperature dependence of the resistance, for all three samples, as measured with a current $I = 1 \mu\text{A}$. S1 was measured in a first cooldown while S2 and S3 were measured together in a second cooldown.

during this cooldown. The temperature dependence of S2 and S3 was taken during a slow warm up of the system between 1.2 and 4.2 K and during a slow cooldown of the system (8 hours) between 0.05 to 0.8 K.

The temperature dependence of S1 shows an onset of a plateau at $T < 200$ mK possibly indicating either that the actual electronic base temperature is about 200 mK for these measurements or more probably that it is a saturation of the effect leading to the negative magnetoresistance at very low temperature. The amplitude of this effect is about 14 % for S1 and S3, 7 % for S2. As mentioned in the chapter 4, S1, S2 and S3 are showing different disorder (amplitude and correlation length). Hence these differences of amplitude could be related to the disorder. Indeed, S1 and S3 are described by the same exponent of the XMR power-law and show a similar amplitude of the negative magnetoresistance.

5.2.3 Isotropic negative magneto-resistance

To better understand the nature of this resistance increase at very low temperatures, we investigated the in-plane MR in details. The results are shown for sample S1, but similar results were obtained with samples S2 and S3. As seen in 5.4 (left), the MR is associated to a positive magneto-conductance, which shows its suppression under moderate magnetic fields. Almost equivalent results are obtained for an in-plane magnetic field being applied either parallel or perpendicular to the current. A very small anisotropy is visible, an effect that will be explained in more details in the next section. Using a 3D vector magnet, this in-plane magnetoresistance was mapped

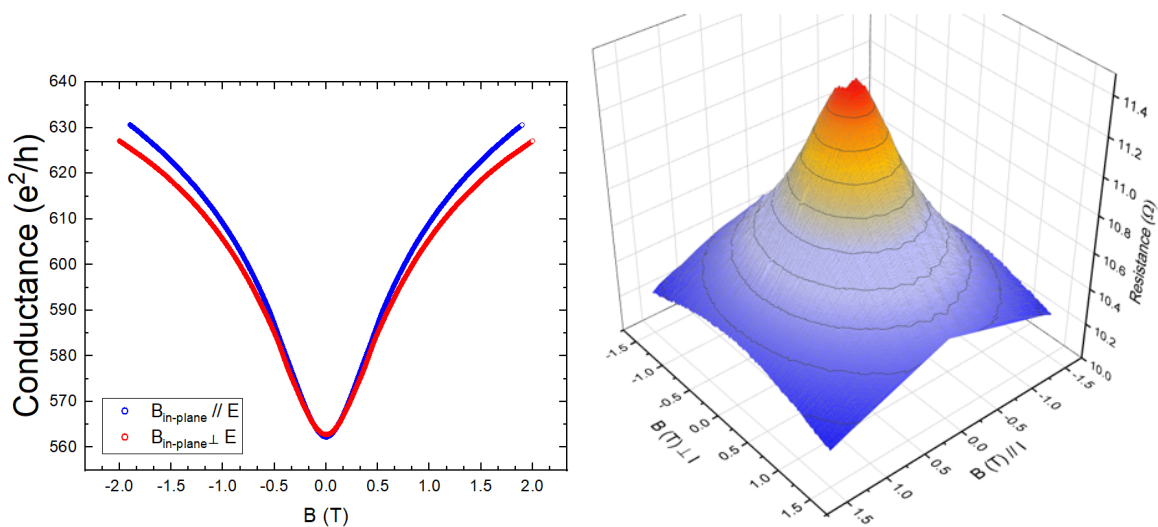


FIGURE 5.4: Left : In-plane magnetoresistance of S1, measured at 100 mK for $I = 1 \mu\text{A}$. Right : Mapping of the in-plane magnetoresistance of S1, measured at 100 mK for $I = 1 \mu\text{A}$, done by setting the magnetic field parallel to the electrical field and sweeping the magnetic field perpendicular to the electric field.

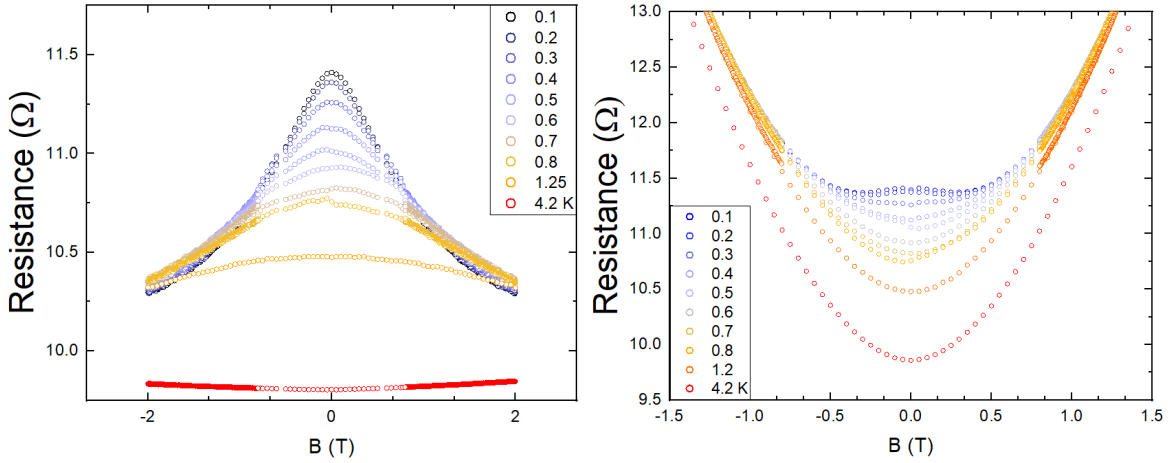


FIGURE 5.5: Evolution of the magnetoresistance for different temperatures of S1 and a current $I = 1 \mu\text{A}$: a) in-plane, b) out-of-plane

for a magnetic field along all in-plane directions, thus confirming the isotropy of this negative MR. The amplitude of the MR excludes any quantum coherence effect like the weak-antilocalization since its amplitude is about $35 G_0$ at 2 T, G_0 being the quantum of conductance [Datta, 1995].

To investigate the temperature dependence of this negative MR, the temperature was stabilized at different temperature and the magnetic field swept. Due to possible heating effects occurring at low magnetic fields when the field is swept through zero, we also performed some static measurements in the low-field regime. In this case, we fixed both the temperature and the magnetic field and recorded the resistance as

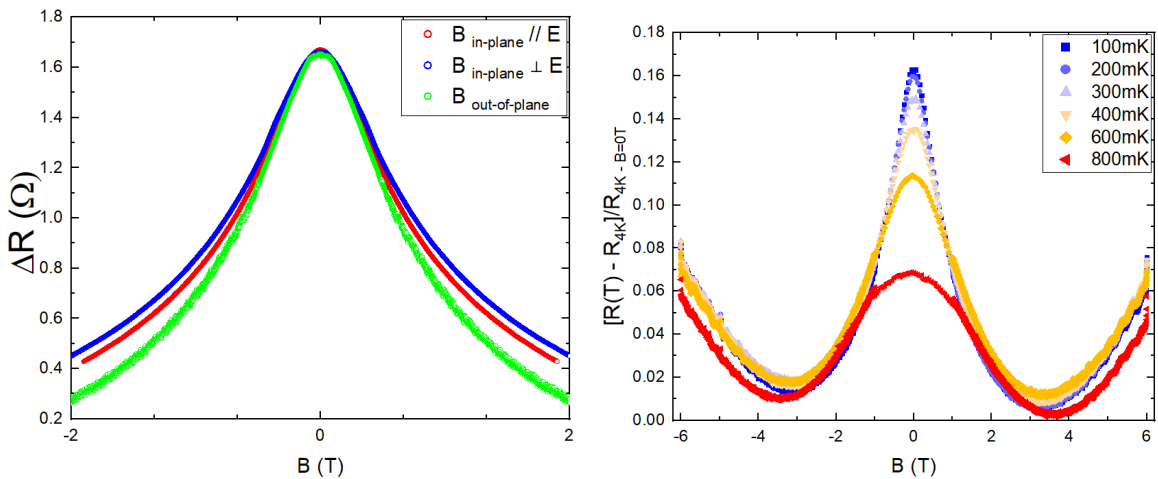


FIGURE 5.6: a) Comparison of the relative magnetoresistance $\Delta R(B) = R(T = 100 \text{ mK}, B) - R(T = 4.2 \text{ K}, B)$ of S1 for the three different magnetic field direction, b) Temperature dependence of the relative resistance $(R(T) - R(4.2 \text{ K})) / R(4.2 \text{ K}, B = 0 \text{ T})$ of S1 as a function of an out-of-plane magnetic field, showing both the temperature-dependent negative MR and the temperature independent positive MR

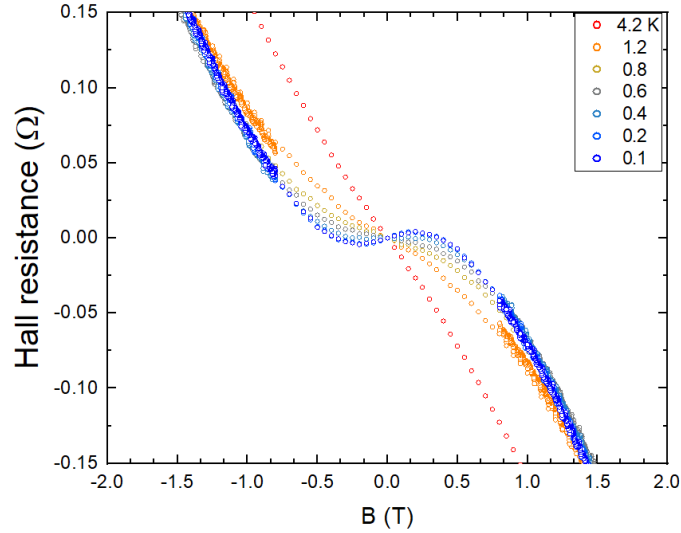


FIGURE 5.7: Hall resistivity as a function of an out-of-plane magnetic field of S1 for different temperatures and a current of $1 \mu\text{A}$

a function of time. After stabilization, we averaged our data over 30 measurements in order to reduce the noise level, and the magnetic field was then changed step by step. Static measurements were made between -200 mT and 200 mT whereas slow magnetic field sweeps were realized for $|B| > 200 \text{ mT}$, with a perfect continuity, these data are patched together and shown at different temperatures in figure 5.5. The temperature dependence of the magnetoresistance was measured from 100 mK to 1.25 K for an in-plane magnetic field perpendicular to the current as well as for an out-of-plane magnetic field.

Considering the out-of-plane MR at very low temperature, the negative longitudinal magnetoresistance appears as shown in the right panel of figure 5.6, after subtracting the background measured at 4.2 K . From the plot of $\Delta R(B) = R(T=100\text{mK}, B) - R(T=4.2\text{K}, B)$, performed for all three directions, it is very clear that this effect is almost isotropic. This result was confirmed on the four nanostructures measured (S1, S2, S3 and S4). Importantly, this evolution of the negative MR goes along with a significant change of the Hall resistance.

The origin of this MR cannot be attributed to a chiral anomaly for the following reasons :

- the position of the Fermi energy is far away below the two Weyl nodes
- the coupling between the two Weyl nodes of opposite chirality by a static disorder strongly reduces a possible chiral imbalance for $B \parallel E$ [Sykora et al., 2020b]
- the negative MR is isotropic.

Instead, our alternative explanation consider the effect of the magnetic field and the disorder on the band structure and its consequences on the transport properties. This evolution is corroborated by the change observed in the Hall resistivity at very low temperature (figure 5.7). In the next section, we discuss this novel mechanism, related to the Weyl nature of the band structure, which captures all details of our experimental findings.

5.3 Theory and discussion

In the chapter 4, we already saw that numerical simulations considering the exact band structure of WTe_2 are able to reproduce with a good accuracy the magnetoresistance at high temperature ($T > 4.2$ K), allowing us to understand the origin of the XMR subquadraticity and the role played by disorder. Here again, such numerical treatment shed light on this phenomena and give us some unambiguous understanding of the origin of both the negative magnetoresistance and the change in the Hall magnetoresistance. Using the same formalism as already described above, it was possible to show that, in order to maintain the global charge neutrality, the chemical potential drifts at very low temperature. Such a drift implies a temperature dependence of the resistance that is very likely at the origin of the resistance upturn observed in our experiments. A very similar effect happens when the magnetic field is applied (figure 5.8). Considering such a drift of the chemical potential, it is possible to reproduce the negative MR results.

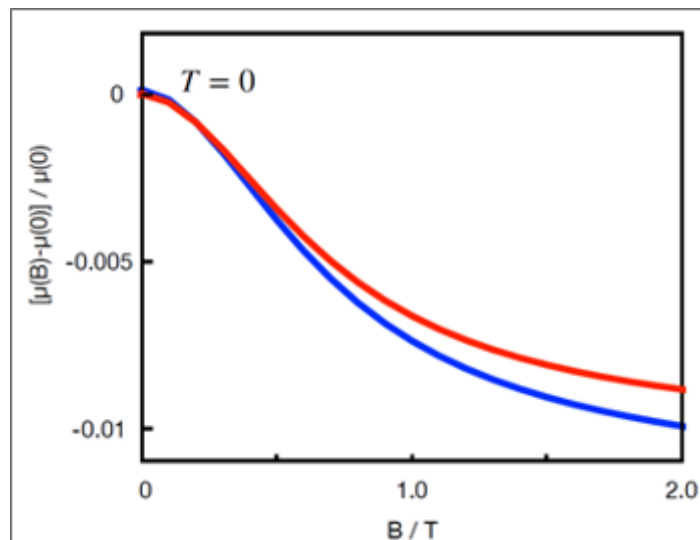


FIGURE 5.8: Numerical calculations of the chemical potential versus the magnetic field

Magnetic field dependence

The effect of a magnetic field is at first sight to move the Weyl nodes of different chirality apart from each other. This can be easily understood by considering the effect of a Zeeman interaction in both a normal metal and a Weyl semimetal. In a normal metal, a Zeeman term leads to an energy splitting of the spin up and spin down electronic bands, as shown in the left panel of figure 5.9. Generally, the total density of states changes only very weakly and the MR measured is therefore very small.

The case of Weyl semimetals is qualitatively different. For the sake of clarity, we consider now the case of a Weyl semimetal of type I but similar effects occur in a type II Weyl semimetal. In such a system the minimal Hamiltonian including the Zeeman term is :

$$\mathcal{H} = \pm \hbar v \sigma \cdot k + \mu_B g B \cdot \sigma \quad (5.1)$$

with \pm depending on the chirality, v the fermi velocity, σ the Pauli matrices, k the wave vector, g the gyromagnetic ratio and B the magnetic field. Considering a

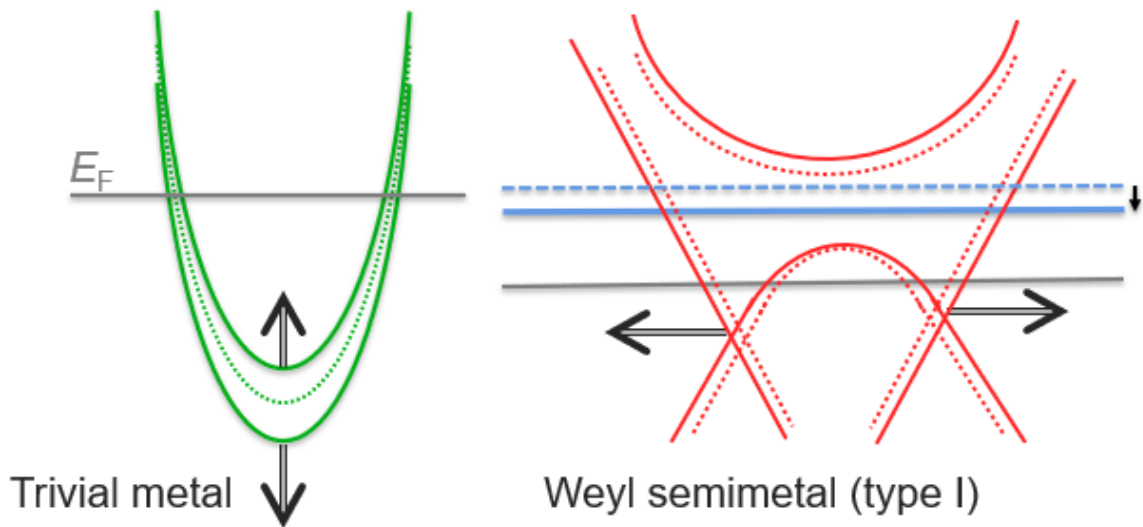


FIGURE 5.9: Sketch of the modification of the band structure with a Zeeman energy in a) a trivial metal, b) a Weyl semimetal. The dot lines represent the band structure for a magnetic field $B=0$ whereas the straight lines correspond to $B \neq 0$. If $B \neq 0$, a Zeeman term in the Hamiltonian shifts the electron band of spin up and spin down apart in a trivial metal. In the case of a Weyl semimetal two cases have to be distinguished : if the Fermi energy is far away from the Weyl nodes (blue dashed line), a Zeeman term shift the Weyl nodes in momentum, increasing the DOS at the Fermi level and leading to a shift of the chemical potential (blue straight line). This effect does not take place if the Fermi energy is close to the Weyl nodes (grey line).

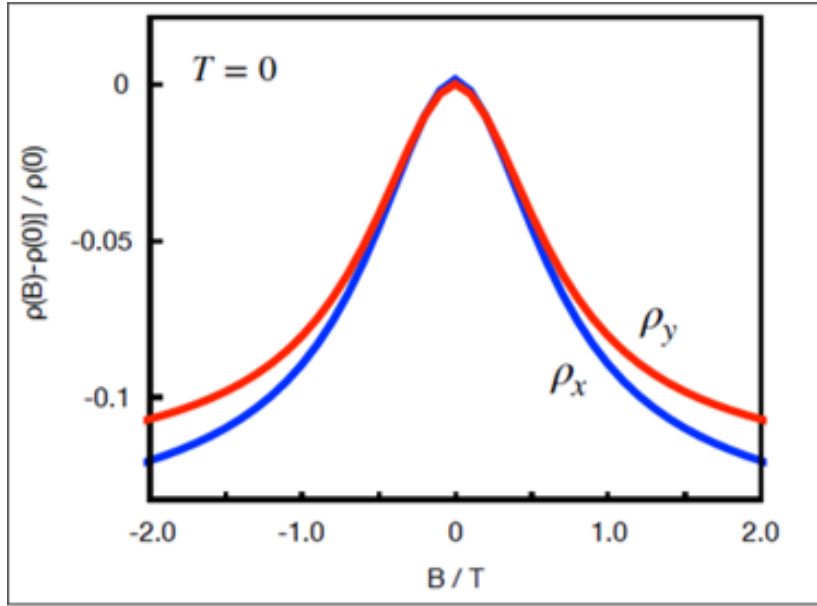


FIGURE 5.10: Numerical simulation of the magnetoresistivity at 0 K for a magnetic field parallel to the current ρ_x and perpendicular to the current ρ_y

magnetic field in the x direction, it reads :

$$\mathcal{H} = \pm \hbar v \sigma_y k_y \pm \hbar v \sigma_z k_z \pm \hbar v \sigma_x k_x + \mu_B g B_x \sigma_x \quad (5.2)$$

In this case, the Zeeman term shifts the Weyl nodes position of a wave vector $\delta k_x = \pm \frac{\mu_B g B_x}{\hbar v}$ depending on their chirality.

This effect is illustrated in figure 5.8. Very importantly, this effect only matters when the Fermi energy is far enough from the Weyl nodes, above the Lifshitz transition. Indeed, if E_F is close to the Weyl nodes (the grey line on the figure 5.9), the position of the Fermi pockets changes in the real space but not their size. Therefore, the position of the Fermi energy is not influenced by an external magnetic field. On the contrary, if the Fermi energy is far away from the Weyl nodes (beyond the Lifshitz transition, blue line in figure 5.9), the magnetic field strongly influences the size of the Fermi pockets. Due to charge conservation, this effect induces a shift of the chemical potential in order to ensure the charge neutrality. This shift changes the density of states, which explains the magnetoresistance observed in both the longitudinal and the Hall measurements.

As shown in chapter 4, it is possible to calculate the magnetoresistance by numerical simulations including a finite disorder. As shown in figure 5.10, the magnetoresistance for an in-plane magnetic field parallel or perpendicular to the current orientation is well reproduced. The simulations capture the almost isotropic

behavior and also reveal the small in-plane anisotropy between the two in-plane axes. We note that not only the shape of the MR is reproduced but there is also a rather good quantitative agreement between experiments and calculations. This work is still in progress, with the aim to understand the effect of the disorder (amplitude and nature -short range or long range-) on this negative MR, in order to better fit our experimental data.

Temperature dependence

To better understand the temperature dependence of the negative MR, let us consider the formula of the conductivity at $T = 0$ and $T \neq 0$:

$$\sigma_{T=0} = e^2 \text{DOS} \times D = e^2 \text{DOS} \times \frac{v_F l_{\text{tr}}}{d} \quad (5.3)$$

$$\sigma_{T \neq 0} = e^2 \int_{-\infty}^{+\infty} \text{DOS}(E) \times \frac{v_F(E) l_{\text{tr}}(E)}{d} \frac{\partial f_{\text{FD}}(E)}{\partial E} dE \quad (5.4)$$

with D the diffusion coefficient, DOS the density of states, l_{tr} the transport length and d the dimensionality of the system. In the expression, two parameters could explain such a change in the resistivity, either an abrupt change in the density of states or an abrupt change in the transport length. There is no reason for the Fermi velocity to change at such a low temperature if the density of states is not changing. As shown in figure 5.11, the DOS calculated from numerical simulations shows only

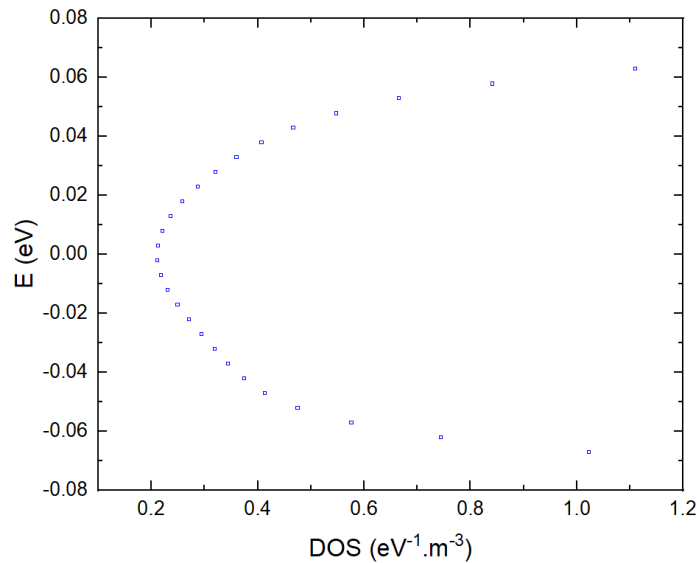


FIGURE 5.11: Density of states of WTe₂ calculated around the compensation

a few percent change around $E_F = 0$ eV over an energy range given by $4 k_B T$ which is about 1.2 meV at 4 K. The conductivity can be therefore expressed as:

$$\sigma_{T \neq 0} = e^2 \text{DOS} \times v_F \int_{-\infty}^{+\infty} \frac{l_{\text{tr}}(E)}{d} \frac{\partial f_{FD}(E)}{\partial E} dE \quad (5.5)$$

The origin of the temperature dependence of the conductivity at very low temperature is very likely induced by the energy dependence of the transport length. Ongoing numerical simulations are focusing on this specific question of the temperature dependence of the transport length in order to confirm the origin of the upturn of the resistance at very low temperature.

5.4 Conclusion

In this chapter, we have measured the temperature dependence of the resistance of different nanostructures of WTe_2 that all show an upturn of the resistance below 4.2 K. Such a temperature dependence is very probably related to a strong energy dependence of the transport length. Concomitantly, an isotropic negative magnetoresistance was observed at very low temperature; a feature that cannot be attributed to the chiral anomaly but rather to the effect of the magnetic fields on the band structure of WTe_2 .

The NMR was fully characterized as a function of the magnetic field at very low temperature. All samples show some qualitative agreement but with small quantitative differences in their amplitudes that could be related to different degrees of disorder. Numerical simulations show that this new mechanism is related to the Weyl nature of the band structure that is at the origin of an increase of the DOS when the magnetic field is swept. This effect only happens if the Fermi energy is located far away from the Weyl nodes. Due to charge neutrality, the increase of the DOS is compensated by a shift of the chemical potential that induces a NMR.

CONCLUSION

In this thesis, we investigated the magneto-transport properties of monocrystalline disordered nanostructures of WTe_2 , a type-II Weyl semimetal, with the typical degree of disorder and charge doping as investigated by other groups. High-quality nanostructures were obtained by two different growth methods, with the initial goal to perform a comparative study so as to better understand the influence of disorder on charge transport properties. Our results show that the complex band structure of WTe_2 still plays a primary role and that its multi-band nature must be considered in order to describe the magneto-resistance processes in disordered nanostructures. Furthermore, we evidenced that the non-trivial topology of this Weyl semimetal results in a low-field negative magneto-resistance due to high-energy Weyl quasi-particles. This new mechanism thus occurs when the Fermi energy is far away from the Weyl nodes, contrary to that one related to the chiral anomaly, and it exists in the nearly charge-compensation regime, where the XMR is also observed.

This study of WTe_2 nanostructures allowed us to understand the extremely large magnetoresistance of this material, beyond previous studies. The Shubnikov-de Haas analysis revealed the different carrier densities, for each band, and showed the robustness of the charge compensation in WTe_2 , with charge carrier densities equal to $3 \times 10^{19} \text{ cm}^{-3}$ for both electrons and holes for thicknesses larger than 50 nm. For thinner nanostructures, a study of Shubnikov-de Haas oscillations has reported that the band structure is slowly changing with the thickness, with an increasing electron-hole band gap, [Xiang et al., 2018], leading at the monolayer limit to the realization of a quantum spin Hall insulator. In the bulk-band limit, our analysis revealed some limits of the two-band approximation used in some previous studies, which cannot give access to the exact average carrier densities nor account for the XMR subquadratic behavior. A multi-band model was thus developed and some calculations within a three-band model (two hole bands and a single electron band),

taking carrier densities inferred from SdH oscillations into account, allowed us to better understand the subquadratic behavior. This power-law dependence was shown not to be directly related to the degree of disorder but, rather, to be the consequence of large difference in the carrier mobilities between the bands. Considering the real band structure of bulk WTe₂, some numerical simulations with a gaussian potential for disorder, acting on the multi-band structure, was investigated. These calculations showed a non-monothonic behavior of the power-law coefficient and helped us to better understand why the subquadratic law is not directly related to RRR values (degree of disorder).

Nevertheless, further studies are still needed in order to better reproduce both the longitudinal and transverse magneto-resistances. To go further from an experimental point of view, it will be necessary to pattern Hall bars in order to avoid any artefact from ohmic contacts, and confirm the role of a higher mobility hole band. For the numerical simulations, more work needs to be done to better understand the influence of scattering by disorder on multi-band transport. For example, a power law coefficient above two was identified by theory, but never observed in experiments.

Importantly, this work has clarified the apparent paradox that both the extremely-large positive MR and the low-field negative MR could be observed in the near-charge compensation regime. Whereas the latter is often interpreted as the signature of the chiral anomaly for low-energy Weyl fermions, we give evidence for another mechanism that is associated to high-energy Weyl fermions. This effect takes its root in the shift in impulsion of the Weyl nodes by a magnetic field, leading to an increase of the DOS if the Fermi energy is far away from the Weyl nodes. This results in a shift of the chemical potential and to a nearly isotropic negative magnetoresistance, independent from the relative orientation of the magnetic and electric fields.

Whereas the magnetic-field dependence of the negative MR, as well as its small in-plane anisotropy, is well captured by our model, a better understanding of the temperature dependence still requires some more experiments, possibly using an electrical gate. For instance, starting with a Fermi level at the perfect compensation, it will be interesting to shift it closer to the Weyl nodes, this could validate the picture that close to the Weyl nodes, the density of states does not change and so the chemical potential does not shift in an experimental study. It will also be interesting to do quantum capacitance measurements that would give direct access to the density of states. In addition, new numerical calculations are needed so as to better understand the influence of both the band structure and disorder on the amplitude and anisotropy of the negative MR. For instance, the amplitude was found to vary from sample to sample in our experiments. This could be related to the different degrees

of disorder in the nanostructures or could be due to a different position of the Fermi level. Furthermore, the anisotropic in-plane magnetoresistance that already appears at 4.2 K is not yet understood. This anisotropic magnetoresistance could be the reason for a misinterpretation of the negative MR in terms of the chiral anomaly, as reported in some studies. Our study highlights the need for a careful analysis of the negative magnetoresistance, if to confirm it as a signature of the chiral anomaly in Weyl semimetal.

More generally, this work calls for a similar multi-band analysis of magneto-transport measurements in other materials related to WTe_2 . The analysis of the XMR subquadratic law realized here can also be made for $MoTe_2$ and other solid solution compounds $W_{1-x}Mo_xTe_2$, all with similar band structures [Deng et al., 2016] [Huang et al., 2016] [Belopolski et al., 2016]. Regarding the negative magnetoresistance far from the Weyl nodes, the origin of the temperature dependence related to a possible change of the transport length needs to be confirmed but it would be interesting to study the solid solution compounds because as x increases, the Fermi energy increases and gets closer to the Weyl nodes. This could be an interesting alternative to the study of the energy dependence of the negative MR in WTe_2 . Ultimately, by decreasing the energy of Weyl fermions, a crossover may be observed from the nearly-isotropic to the anisotropic negative MR, the latter being induced by the chiral anomaly, provided that the inter-band scattering rate remains small (that is, for a small degree of disorder). On the other hand, due to a too large difference in their band structures, other type-II Weyl semimetals such as WP_2 or $TaIrTe_4$ may not show similar effects as those studied here with WTe_2 as shown in the Appendix A [Belopolski et al., 2017] [Koepernik et al., 2016]. To precise this point and considering WP_2 , the two Weyl points next to each other in the band structure are of the same chirality, thus, the magnetic field will not increase the density of states for a Fermi energy far away from the Weyl nodes.

BIBLIOGRAPHY

- [Adler, 1969] S. L. Adler. Axial-vector vertex in spinor electrodynamics. *Physical Review*, 177(5):2426–2438, jan 1969.
- [Ali et al., 2014] M. N. Ali, J. Xiong, S. Flynn, J. Tao, Q. D. Gibson, L. M. Schoop, T. Liang, N. Haldolaarachchige, M. Hirschberger, N. P. Ong, and R. J. Cava. Large, non-saturating magnetoresistance in WTe₂. *Nature*, 514(7521):205–208, oct 2014.
- [Altland and Zirnbauer, 1997] A. Altland and M. R. Zirnbauer. Nonstandard symmetry classes in mesoscopic normal-superconducting hybrid structures. *Physical Review B - Condensed Matter and Materials Physics*, 55(2):1142–1161, jan 1997.
- [Argyres and Adams, 1956] P. N. Argyres and E. N. Adams. Longitudinal magnetoresistance in the quantum limit. *Physical Review*, 104(4):900–908, nov 1956.
- [Armitage et al., 2018] N. P. Armitage, E. J. Mele, and A. Vishwanath. Weyl and Dirac semimetals in three-dimensional solids. *Reviews of Modern Physics*, 90(1):15001, 2018.
- [Autès et al., 2016] G. Autès, D. Gresch, M. Troyer, A. A. Soluyanov, and O. V. Yazyev. Robust Type-II Weyl Semimetal Phase in Transition Metal Diphosphides X P₂ (X=Mo, W). *Physical Review Letters*, 117(6):066402, aug 2016.
- [Behrends et al., 2016] J. Behrends, A. G. Grushin, T. Ojanen, and J. H. Bardarson. Visualizing the chiral anomaly in Dirac and Weyl semimetals with photoemission spectroscopy. *Physical Review B*, 93(7):075114, feb 2016.
- [Bell and Jackiw, 1969] J. S. Bell and R. Jackiw. A PCAC puzzle: $\pi^0 \rightarrow \gamma\gamma$ in the σ -model. *Il Nuovo Cimento A*, 60(1):47–61, mar 1969.
- [Belopolski et al., 2016] I. Belopolski, D. S. Sanchez, Y. Ishida, X. Pan, P. Yu, S. Y. Xu, G. Chang, T. R. Chang, H. Zheng, N. Alidoust, G. Bian, M. Neupane, S. M. Huang, C. C. Lee, Y. Song, H. Bu, G. Wang, S. Li, G. Eda, H. T. Jeng, T. Kondo, H. Lin, Z. Liu, F. Song, S. Shin, and M. Zahid Hasan. Discovery of a new type of topological Weyl fermion semimetal state in Mo_xW_{1-x}Te₂. *Nature Communications*, 7(1):1–9, dec 2016.
- [Belopolski et al., 2017] I. Belopolski, P. Yu, D. S. Sanchez, Y. Ishida, T. R. Chang, S. S. Zhang, S. Y. Xu, H. Zheng, G. Chang, G. Bian, H. T. Jeng, T. Kondo, H. Lin, Z. Liu, S. Shin, and M. Z. Hasan. Signatures of a time-reversal symmetric Weyl semimetal with only four Weyl points. *Nature Communications*, 8(1):12, dec 2017.

- [Bernevig et al., 2006] B. A. Bernevig, T. L. Hughes, and S. C. Zhang. Quantum spin hall effect and topological phase transition in HgTe quantum wells. *Science*, 314(5806):1757–1761, dec 2006.
- [Berry, 1984] M. Berry. Quantal phase factors accompanying adiabatic changes. *Proceedings of the Royal Society of London. A. Mathematical and Physical Sciences*, 392(1802):45–57, mar 1984.
- [Berry, 1989] M. Berry. Quantum scars of classical closed orbits in phase space. *Proceedings of the Royal Society of London. A. Mathematical and Physical Sciences*, 423(1864):219–231, may 1989.
- [Bradlyn et al., 2016] B. Bradlyn, J. Cano, Z. Wang, M. G. Vergniory, C. Felser, R. J. Cava, and B. A. Bernevig. Beyond Dirac and Weyl fermions: Unconventional quasiparticles in conventional crystals. *Science*, 353(6299), aug 2016.
- [Bulmash et al., 2014] D. Bulmash, C. X. Liu, and X. L. Qi. Prediction of a Weyl semimetal in Hg_{1-x}YCd_xMn_yTe. *Physical Review B - Condensed Matter and Materials Physics*, 89(8):081106, feb 2014.
- [Burkov, 2014] A. A. Burkov. Anomalous hall effect in weyl metals. *Physical Review Letters*, 113(18):187202, oct 2014.
- [Burkov, 2015] A. A. Burkov. Chiral anomaly and transport in Weyl metals. *Journal of Physics Condensed Matter*, 27(11), 2015.
- [Burkov and Balents, 2011] A. A. Burkov and L. Balents. Weyl semimetal in a topological insulator multilayer. *Physical Review Letters*, 107(12), 2011.
- [Cao and Chen, 2019] C. Cao and J. Chen. Quantum Spin Hall Materials. *Advanced Quantum Technologies*, 2(10):1900026, 2019.
- [Chambers, 1990] R. G. Chambers. *Electronics in Metals and Semiconductors*. Springer Netherlands, 1990. ISBN 978-0-412-36840-0.
- [Chandni et al., 2015] U. Chandni, E. A. Henriksen, and J. P. Eisenstein. Transport in indium-decorated graphene. *Physical Review B - Condensed Matter and Materials Physics*, 91(24):245402, jun 2015.
- [Chang, 2020] C. Z. Chang. Marriage of topology and magnetism. *Nature Materials*, 19(5):484–485, may 2020.
- [Chang et al., 2013] C. Z. Chang, J. Zhang, X. Feng, J. Shen, Z. Zhang, M. Guo, K. Li, Y. Ou, P. Wei, L. L. Wang, Z. Q. Ji, Y. Feng, S. Ji, X. Chen, J. Jia, X. Dai, Z. Fang, S. C. Zhang, K. He, Y. Wang, L. Lu, X. C. Ma, and Q. K. Xue. Experimental observation of the quantum anomalous Hall effect in a magnetic topological Insulator. *Science*, 340(6129):167–170, apr 2013.

- [Chang et al., 2015] C. Z. Chang, W. Zhao, D. Y. Kim, H. Zhang, B. A. Assaf, D. Heiman, S. C. Zhang, C. Liu, M. H. Chan, and J. S. Moodera. High-precision realization of robust quantum anomalous Hall state in a hard ferromagnetic topological insulator. *Nature Materials*, 14(5):473–477, may 2015.
- [Chiu et al., 2016] C. K. Chiu, J. C. Teo, A. P. Schnyder, and S. Ryu. Classification of topological quantum matter with symmetries. *Reviews of Modern Physics*, 88(3):1–63, 2016.
- [Cresti et al., 2014] A. Cresti, D. Van Tuan, D. Soriano, A. W. Cummings, and S. Roche. Multiple quantum phases in graphene with enhanced spin-orbit coupling: From the quantum spin hall regime to the spin hall effect and a robust metallic state. *Physical Review Letters*, 113(24):246603, dec 2014.
- [Dalibard, 2016] J. Dalibard. Lecture notes. 2016. URL http://www.phys.ens.fr/~dalibard/CdF/2018/notes_cours_1.pdf.
- [Das et al., 2020] B. Das, D. Sen, and S. Mahapatra. Tuneable quantum spin Hall states in confined 1T' transition metal dichalcogenides. *Scientific Reports*, 10(1):1–13, dec 2020.
- [Das et al., 2019] P. K. Das, D. Di Sante, F. Cilento, C. Bigi, D. Kopic, D. Soranzio, A. Sterzi, J. A. Krieger, I. Vobornik, J. Fujii, T. Okuda, V. N. Strocov, M. B. H. Breese, F. Parmigiani, G. Rossi, S. Picozzi, R. Thomale, G. Sangiovanni, R. J. Cava, and G. Panaccione. Electronic properties of candidate type-II Weyl semimetal WTe₂. A review perspective. *Electronic Structure*, 1(1):014003, mar 2019.
- [Datta, 1995] S. Datta. *Electronic Transport in Mesoscopic Systems*. Cambridge University Press, sep 1995. ISBN 9780442312213.
- [De Waele, 2011] A. T. De Waele. Basic operation of cryocoolers and related thermal machines. *Journal of Low Temperature Physics*, 164(5-6):179–236, sep 2011.
- [Deng et al., 2018] J. Deng, B. Xia, X. Ma, H. Chen, H. Shan, X. Zhai, B. Li, A. Zhao, Y. Xu, W. Duan, S. C. Zhang, B. Wang, and J. G. Hou. Epitaxial growth of ultraflat stanene with topological band inversion. *Nature Materials*, 17(12):1081–1086, dec 2018.
- [Deng et al., 2016] K. Deng, G. Wan, P. Deng, K. Zhang, S. Ding, E. Wang, M. Yan, H. Huang, H. Zhang, Z. Xu, J. Denlinger, A. Fedorov, H. Yang, W. Duan, H. Yao, Y. Wu, S. Fan, H. Zhang, X. Chen, and S. Zhou. Experimental observation of topological Fermi arcs in type-II Weyl semimetal MoTe₂. *Nature Physics*, 12(12):1105–1110, dec 2016.
- [Dirac, 1928] A. M. Dirac. The quantum theory of the electron. *Proceedings of the Royal Society of London. Series A, Containing Papers of a Mathematical and Physical Character*, 117(778):610–624, feb 1928.
- [dos Reis et al., 2016] R. D. dos Reis, M. O. Ajeesh, N. Kumar, F. Arnold, C. Shekhar, M. Naumann, M. Schmidt, M. Nicklas, and E. Hassinger. On the search for the chiral anomaly

- in Weyl semimetals: the negative longitudinal magnetoresistance. *New Journal of Physics*, 18(8):085006, aug 2016.
- [Du et al., 2015] L. Du, I. Knez, G. Sullivan, and R. R. Du. Robust helical edge transport in gated InAs/GaSb bilayers. *Physical Review Letters*, 114(9), 2015.
- [Du et al., 2017] L. Du, X. Li, W. Lou, G. Sullivan, K. Chang, J. Kono, and R. R. Du. Evidence for a topological excitonic insulator in InAs/GaSb bilayers. *Nature Communications*, 8(1): 1–8, 2017.
- [Ekin, 2006] J. Ekin. Experimental Techniques for Low-Temperature Measurements: Cryostat Design, Material Properties and Superconductor Critical-Current Testing. *Experimental Techniques for Low-Temperature Measurements: Cryostat Design, Material Properties and Superconductor Critical-Current Testing*, 9780198570547:1–704, 2006.
- [Fatemi et al., 2017] V. Fatemi, Q. D. Gibson, K. Watanabe, T. Taniguchi, R. J. Cava, and P. Jarillo-Herrero. Magnetoresistance and quantum oscillations of an electrostatically tuned semimetal-to-metal transition in ultrathin WTe₂. *Physical Review B*, 95(4):041410, jan 2017.
- [Fatemi et al., 2018] V. Fatemi, S. Wu, Y. Cao, L. Bretheau, Q. D. Gibson, K. Watanabe, T. Taniguchi, R. J. Cava, and P. Jarillo-Herrero. Electrically tunable low-density superconductivity in a monolayer topological insulator. *Science*, 362(6417):926–929, nov 2018.
- [Fei et al., 2017] Z. Fei, T. Palomaki, S. Wu, W. Zhao, X. Cai, B. Sun, P. Nguyen, J. Finney, X. Xu, and D. H. Cobden. Edge conduction in monolayer WTe₂. *Nature Physics*, 13(7):677–682, jul 2017.
- [Finocchiaro et al., 2017] F. Finocchiaro, F. Guinea, and P. San-Jose. Quantum spin hall effect in twisted bilayer graphene. *2D Materials*, 4(2):025027, jun 2017.
- [Fu and Kane, 2007] L. Fu and C. L. Kane. Topological insulators with inversion symmetry. *Physical Review B - Condensed Matter and Materials Physics*, 76(4):045302, jul 2007.
- [Fu et al., 2007] L. Fu, C. L. Kane, and E. J. Mele. Topological insulators in three dimensions. *Physical Review Letters*, 98(10):106803, mar 2007.
- [Gao et al., 2017] W. Gao, N. Hao, F. W. Zheng, W. Ning, M. Wu, X. Zhu, G. Zheng, J. Zhang, J. Lu, H. Zhang, C. Xi, J. Yang, H. Du, P. Zhang, Y. Zhang, and M. Tian. Extremely Large Magnetoresistance in a Topological Semimetal Candidate Pyrite PtBi₂. *Physical Review Letters*, 118(25):256601, jun 2017.
- [Garcia et al., 2020] J. H. Garcia, M. Vila, C. H. Hsu, X. Waintal, V. M. Pereira, and S. Roche. Canted Persistent Spin Texture and Quantum Spin Hall Effect in WTe₂. *Physical Review Letters*, 125(25):256603, dec 2020.

- [Grauer et al., 2015] S. Grauer, S. Schreyeck, M. Winnerlein, K. Brunner, C. Gould, and L. W. Molenkamp. Coincidence of superparamagnetism and perfect quantization in the quantum anomalous Hall state. *Physical Review B - Condensed Matter and Materials Physics*, 92(20):201304, nov 2015.
- [Grushin and Bardarson, 2017] A. G. Grushin and J. H. Bardarson. How to Make Devices with Weyl Materials. *Physics*, 10, 2017.
- [Halász and Balents, 2012] G. B. Halász and L. Balents. Time-reversal invariant realization of the Weyl semimetal phase. *Physical Review B - Condensed Matter and Materials Physics*, 85(3):035103, jan 2012.
- [Haldane, 1983] F. D. Haldane. Nonlinear field theory of large-spin Heisenberg antiferromagnets: Semiclassically quantized solitons of the one-dimensional easy-axis Néel state. *Physical Review Letters*, 50(15):1153–1156, 1983.
- [Halperin, 1982] B. I. Halperin. Quantized Hall conductance, current-carrying edge states, and the existence of extended states in a two-dimensional disordered potential. *Physical Review B*, 25(4):2185–2190, feb 1982.
- [Hansen et al., 2020] F. Hansen, M. Wels, S. Froeschke, A. Popov, D. Wolf, B. Büchner, P. Schmidt, and S. Hampel. Thermodynamic Evaluation and Chemical Vapor Transport of Few-Layer WTe₂. *Crystal Growth & Design*, 20(11):7341–7349, nov 2020.
- [Hasan and Kane, 2010] M. Z. Hasan and C. L. Kane. Colloquium: Topological insulators. *Reviews of Modern Physics*, 82(4):3045–3067, 2010.
- [Hills et al., 2017] R. D. Hills, A. Kusmartseva, and F. V. Kusmartsev. Current-voltage characteristics of Weyl semimetal semiconducting devices, Veselago lenses, and hyperbolic Dirac phase. *Physical Review B*, 95(21):214103, jun 2017.
- [Hsieh et al., 2008] D. Hsieh, D. Qian, L. Wray, Y. Xia, Y. S. Hor, R. J. Cava, and M. Z. Hasan. A topological Dirac insulator in a quantum spin Hall phase. *Nature*, 452(7190):970–974, apr 2008.
- [Hsieh et al., 2009] D. Hsieh, Y. Xia, D. Qian, L. Wray, J. H. Dil, F. Meier, J. Osterwalder, L. Patthey, J. G. Checkelsky, N. P. Ong, A. V. Fedorov, H. Lin, A. Bansil, D. Grauer, Y. S. Hor, R. J. Cava, and M. Z. Hasan. A tunable topological insulator in the spin helical Dirac transport regime. *Nature*, 460(7259):1101–1105, aug 2009.
- [Huang et al., 2016] L. Huang, T. M. McCormick, M. Ochi, Z. Zhao, M. T. Suzuki, R. Arita, Y. Wu, D. Mou, H. Cao, J. Yan, N. Trivedi, and A. Kaminski. Spectroscopic evidence for a type II Weyl semimetallic state in MoTe₂. *Nature Materials*, 15(11):1155–1160, nov 2016.

- [Huang et al., 2015a] S. M. Huang, S. Y. Xu, I. Belopolski, C. C. Lee, G. Chang, B. Wang, N. Alidoust, G. Bian, M. Neupane, C. Zhang, S. Jia, A. Bansil, H. Lin, and M. Z. Hasan. A Weyl Fermion semimetal with surface Fermi arcs in the transition metal monpnictide TaAs class. *Nature Communications*, 6(1):1–6, jun 2015a.
- [Huang et al., 2015b] X. Huang, L. Zhao, Y. Long, P. Wang, D. Chen, Z. Yang, H. Liang, M. Xue, H. Weng, Z. Fang, X. Dai, and G. Chen. Observation of the Chiral-Anomaly-Induced Negative Magnetoresistance in 3D Weyl Semimetal TaAs. *Physical Review X*, 5(3):031023, aug 2015b.
- [Iftikhar et al., 2016] Z. Iftikhar, A. Anthore, S. Jezouin, F. D. Parmentier, Y. Jin, A. Cavanna, A. Ouerghi, U. Gennser, and F. Pierre. Primary thermometry triad at 6 mK in mesoscopic circuits. *Nature Communications*, 7(1):1–7, sep 2016.
- [Jia et al., 2016] S. Jia, S. Y. Xu, and M. Z. Hasan. Weyl semimetals, Fermi arcs and chiral anomalies. *Nature Materials*, 15(11):1140–1144, oct 2016.
- [Jia et al., 2015] Z. Jia, B. Yan, J. Niu, Q. Han, R. Zhu, D. Yu, and X. Wu. Transport study of graphene adsorbed with indium adatoms. *Physical Review B - Condensed Matter and Materials Physics*, 91(8):085411, feb 2015.
- [Jiang et al., 2015] J. Jiang, F. Tang, X. C. Pan, H. M. Liu, X. H. Niu, Y. X. Wang, D. F. Xu, H. F. Yang, B. P. Xie, F. Q. Song, P. Dudin, T. K. Kim, M. Hoesch, P. K. Das, I. Vobornik, X. G. Wan, and D. L. Feng. Signature of Strong Spin-Orbital Coupling in the Large Nonsaturating Magnetoresistance Material WTe₂. *Physical Review Letters*, 115(16):166601, oct 2015.
- [Kane and Mele, 2005] C. L. Kane and E. J. Mele. Z₂ topological order and the quantum spin hall effect. *Physical Review Letters*, 95(14):146802, sep 2005.
- [Kang et al., 2019] K. Kang, T. Li, E. Sohn, J. Shan, and K. F. Mak. Nonlinear anomalous Hall effect in few-layer WTe₂. *Nature Materials*, 18(4):324–328, apr 2019.
- [Kitaev, 2009] A. Kitaev. Periodic table for topological insulators and superconductors. In *AIP Conference Proceedings*, volume 1134, pages 22–30. AIP, may 2009.
- [Kiyohara et al., 2016] N. Kiyohara, T. Tomita, and S. Nakatsuji. Giant Anomalous Hall Effect in the Chiral Antiferromagnet Mn₃Ge. *Physical Review Applied*, 5(6):064009, jun 2016.
- [Klitzing et al., 1980] K. V. Klitzing, G. Dorda, and M. Pepper. New method for high-accuracy determination of the fine-structure constant based on quantized hall resistance. *Physical Review Letters*, 45(6):494–497, aug 1980.
- [Koepernik et al., 2016] K. Koepernik, D. Kasinathan, D. V. Efremov, S. Khim, S. Borisenko, B. Büchner, and J. Van Den Brink. TaIrTe₄: A ternary type-II Weyl semimetal. *Physical Review B*, 93(20):201101, may 2016.

- [Kong et al., 2015] W. D. Kong, S. F. Wu, P. Richard, C. S. Lian, J. T. Wang, C. L. Yang, Y. G. Shi, and H. Ding. Raman scattering investigation of large positive magnetoresistance material WTe₂. *Applied Physics Letters*, 106(8):081906, feb 2015.
- [König et al., 2007] M. König, S. Wiedmann, C. Brüne, A. Roth, H. Buhmann, L. W. Molenkamp, X. L. Qi, and S. C. Zhang. Quantum spin hall insulator state in HgTe quantum wells. *Science*, 318(5851):766–770, nov 2007.
- [König et al., 2008] M. König, H. Buhmann, L. W. Molenkamp, T. Hughes, C. X. Liu, X. L. Qi, and S. C. Zhang. The quantum spin Hall effect: Theory and experiment. *Journal of the Physical Society of Japan*, 77(3), mar 2008.
- [Kosterlitz and Thouless, 1973] J. M. Kosterlitz and D. J. Thouless. Ordering, metastability and phase transitions in two-dimensional systems. *Journal of Physics C: Solid State Physics*, 6(7):1181–1203, 1973.
- [Kumar et al., 2017] N. Kumar, Y. Sun, N. Xu, K. Manna, M. Yao, V. Süß, I. Leermakers, O. Young, T. Förster, M. Schmidt, H. Borrmann, B. Yan, U. Zeitler, M. Shi, C. Felser, and C. Shekhar. Extremely high magnetoresistance and conductivity in the type-II Weyl semimetals WP₂ and MoP₂. *Nature Communications*, 8(1):1–8, dec 2017.
- [Ky, 1968] V. D. Ky. Planar Hall Effect in Ferromagnetic Films. *physica status solidi (b)*, 26(2): 565–569, jan 1968.
- [Lara-Avila et al., 2015] S. Lara-Avila, S. Kubatkin, O. Kashuba, J. A. Folk, S. Lüscher, R. Yakimova, T. J. Janssen, A. Tzalenchuk, and V. Fal’ko. Influence of Impurity Spin Dynamics on Quantum Transport in Epitaxial Graphene. *Physical Review Letters*, 115(10):106602, sep 2015.
- [Li et al., 2018] H. Li, H. W. Wang, H. He, J. Wang, and S. Q. Shen. Giant anisotropic magnetoresistance and planar Hall effect in the Dirac semimetal Cd₃As₂. *Physical Review B*, 97(20):1–6, 2018.
- [Li et al., 2019a] J. Li, Y. Li, S. Du, Z. Wang, B. L. Gu, S. C. Zhang, K. He, W. Duan, and Y. Xu. Intrinsic magnetic topological insulators in van der Waals layered MnBi₂Te₄-family materials. *Science Advances*, 5(6):5685, jun 2019a.
- [Li et al., 2017a] L. Li, H. H. Xie, J. S. Zhao, X. X. Liu, J. B. Deng, X. R. Hu, and X. M. Tao. Ternary Weyl semimetal NbIrTe₄ proposed from first-principles calculation. *Physical Review B*, 96(2):024106, jul 2017a.
- [Li et al., 2017b] P. Li, Y. Wen, X. He, Q. Zhang, C. Xia, Z. M. Yu, S. A. Yang, Z. Zhu, H. N. Alshareef, and X. X. Zhang. Evidence for topological type-II Weyl semimetal WTe₂. *Nature Communications*, 8(1):1–8, dec 2017b.

- [Li et al., 2019b] P. Li, C. Zhang, Y. Wen, L. Cheng, G. Nichols, D. G. Cory, G. X. Miao, and X. X. Zhang. Anisotropic planar Hall effect in the type-II topological Weyl semimetal WTe₂. *Physical Review B*, 100(20):1–7, 2019b.
- [Liang et al., 2019] D. D. Liang, Y. J. Wang, W. L. Zhen, J. Yang, S. R. Weng, X. Yan, Y. Y. Han, W. Tong, W. K. Zhu, L. Pi, and C. J. Zhang. Origin of planar Hall effect in type-II Weyl semimetal MoTe₂. *AIP Advances*, 9(5), 2019.
- [Liang et al., 2018] S. Liang, J. Lin, S. Kushwaha, J. Xing, N. Ni, R. J. Cava, and N. P. Ong. Experimental Tests of the Chiral Anomaly Magnetoresistance in the Dirac-Weyl Semimetals Na₃Bi and GdPtBi. *Physical Review X*, 8(3):1–13, jul 2018.
- [Liang et al., 2015] T. Liang, Q. Gibson, M. N. Ali, M. Liu, R. J. Cava, and N. P. Ong. Ultrahigh mobility and giant magnetoresistance in the Dirac semimetal Cd₃As₂. *Nature Materials*, 14(3):280–284, nov 2015.
- [Liu et al., 2008] C. Liu, T. L. Hughes, X. L. Qi, K. Wang, and S. C. Zhang. Quantum spin hall effect in inverted type-II semiconductors. *Physical Review Letters*, 100(23):1–4, 2008.
- [Liu et al., 2018] E. Liu, Y. Sun, N. Kumar, L. Muechler, A. Sun, L. Jiao, S. Y. Yang, D. Liu, A. Liang, Q. Xu, J. Kroder, V. Süß, H. Borrmann, C. Shekhar, Z. Wang, C. Xi, W. Wang, W. Schnelle, S. Wirth, Y. Chen, S. T. Goennenwein, and C. Felser. Giant anomalous Hall effect in a ferromagnetic kagome-lattice semimetal. *Nature Physics*, 14(11):1125–1131, nov 2018.
- [Liu et al., 2020] J. Liu, H. Wang, C. Fang, L. Fu, and X. Qian. Van der Waals Stacking-Induced Topological Phase Transition in Layered Ternary Transition Metal Chalcogenides. *Nano Letters*, 17(1):467–475, jan 2020.
- [Luo et al., 2015] Y. Luo, H. Li, Y. M. Dai, H. Miao, Y. G. Shi, H. Ding, A. J. Taylor, D. A. Yarotski, R. P. Prasankumar, and J. D. Thompson. Hall effect in the extremely large magnetoresistance semimetal WTe₂. *Applied Physics Letters*, 107(18):182411, nov 2015.
- [Lv et al., 2015] B. Q. Lv, H. M. Weng, B. B. Fu, X. P. Wang, H. Miao, J. Ma, P. Richard, X. C. Huang, L. X. Zhao, G. F. Chen, Z. Fang, X. Dai, T. Qian, and H. Ding. Experimental Discovery of Weyl Semimetal TaAs. *5*, 5(3):31013, jul 2015.
- [Lv et al., 2017] Y. Y. Lv, X. Li, B. B. Zhang, W. Y. Deng, S. H. Yao, Y. B. Chen, J. Zhou, S. T. Zhang, M. H. Lu, L. Zhang, M. Tian, L. Sheng, and Y. F. Chen. Experimental Observation of Anisotropic Adler-Bell-Jackiw Anomaly in Type-II Weyl Semimetal WTe_{1.98} Crystals at the Quasiclassical Regime. *Physical Review Letters*, 118(9):096603, mar 2017.
- [Ma et al., 2019] Q. Ma, S. Y. Xu, H. Shen, D. MacNeill, V. Fatemi, T. R. Chang, A. M. Mier Valdivia, S. Wu, Z. Du, C. H. Hsu, S. Fang, Q. D. Gibson, K. Watanabe, T. Taniguchi, R. J. Cava, E. Kaxiras, H. Z. Lu, H. Lin, L. Fu, N. Gedik, and P. Jarillo-Herrero. Observation

- of the nonlinear Hall effect under time-reversal-symmetric conditions. *Nature*, 565(7739): 337–342, jan 2019.
- [Mar et al., 1992] A. Mar, S. Jobic, and J. A. Ibers. Metal-Metal vs Tellurium-Tellurium Bonding in WTe₂ and Its Ternary Variants TaIrTe₄ and NbIrTe₄. *Journal of the American Chemical Society*, 114(23):8963–8971, nov 1992.
- [Matsuura et al., 2013] S. Matsuura, P. Y. Chang, A. P. Schnyder, and S. Ryu. Protected boundary states in gapless topological phases. *New Journal of Physics*, 15(25pp):65001, jun 2013.
- [Maxwell et al., 1953] E. A. Maxwell, D. Hilbert, S. Cohn-Vossen, and P. Nemenyi. Geometry and the Imagination. *The Mathematical Gazette*, 37(322):295, 1953.
- [McCormick et al., 2017] T. M. McCormick, I. Kimchi, and N. Trivedi. Minimal models for topological Weyl semimetals. *Physical Review B*, 95(7):1–13, 2017.
- [Menon and Basu, 2020] A. Menon and B. Basu. Anomalous Hall transport in tilted multi-Weyl semimetals. *Journal of Physics Condensed Matter*, 33(4):045602, oct 2020.
- [Murakami and Kuga, 2008] S. Murakami and S. I. Kuga. Universal phase diagrams for the quantum spin Hall systems. *Physical Review B - Condensed Matter and Materials Physics*, 78(16):165313, oct 2008.
- [Murakami et al., 2004] S. Murakami, N. Nagaosa, and S. C. Zhang. Spin-Hall insulator. *Physical Review Letters*, 93(15):156804, oct 2004.
- [Murakami et al., 2017] S. Murakami, M. Hirayama, R. Okugawa, and T. Miyake. Emergence of topological semimetals in gap closing in semiconductors without inversion symmetry. *Science Advances*, 3(5), 2017.
- [Nandy et al., 2017] S. Nandy, G. Sharma, A. Taraphder, and S. Tewari. Chiral Anomaly as the Origin of the Planar Hall Effect in Weyl Semimetals. *Physical Review Letters*, 119(17), 2017.
- [Nielsen and Ninomiya, 1983] H. B. Nielsen and M. Ninomiya. The Adler-Bell-Jackiw anomaly and Weyl fermions in a crystal. *Physics Letters B*, 130(6):389–396, nov 1983.
- [Novoselov et al., 2004] K. S. Novoselov, A. K. Geim, S. V. Morozov, D. Jiang, Y. Zhang, S. V. Dubonos, I. V. Grigorieva, and A. A. Firsov. Electric field in atomically thin carbon films. *Science*, 306(5696):666–669, oct 2004.
- [O’Brien et al., 2016] T. E. O’Brien, M. Diez, and C. W. Beenakker. Magnetic Breakdown and Klein Tunneling in a Type-II Weyl Semimetal. *Physical Review Letters*, 116(23):236401, jun 2016.

- [Otrokov et al., 2019] M. M. Otrokov, I. I. Klimovskikh, H. Bentmann, D. Estyunin, A. Zeugner, Z. S. Aliev, S. Gaß, A. U. Wolter, A. V. Koroleva, A. M. Shikin, M. Blanco-Rey, M. Hoffmann, I. P. Rusinov, A. Y. Vyazovskaya, S. V. Eremeev, Y. M. Koroteev, V. M. Kuznetsov, F. Freyse, J. Sánchez-Barriga, I. R. Amiraslanov, M. B. Babanly, N. T. Mamedov, N. A. Abdullayev, V. N. Zverev, A. Alfonsov, V. Kataev, B. Büchner, E. F. Schwier, S. Kumar, A. Kimura, L. Petaccia, G. Di Santo, R. C. Vidal, S. Schatz, K. Kißner, M. Ünzelmann, C. H. Min, S. Moser, T. R. Peixoto, F. Reinert, A. Ernst, P. M. Echenique, A. Isaeva, and E. V. Chulkov. Prediction and observation of an antiferromagnetic topological insulator. *Nature*, 576(7787):416–422, dec 2019.
- [Peixoto et al., 2016] T. R. Peixoto, H. Bentmann, S. Schreyeck, M. Winnerlein, C. Seibel, H. Maaß, M. Al-Baidhani, K. Treiber, S. Schatz, S. Grauer, C. Gould, K. Brunner, A. Ernst, L. W. Molenkamp, and F. Reinert. Impurity states in the magnetic topological insulator $V:(Bi, Sb)_2Te_3$. *Physical Review B*, 94(19):195140, 2016.
- [Pippard, 1989] A. B. Pippard. *Magnetoresistance in Metals*. Cambridge University Press, 1989. ISBN 9780521118804.
- [Pletikosić et al., 2014] I. Pletikosić, M. N. Ali, A. V. Fedorov, R. J. Cava, and T. Valla. Electronic structure basis for the extraordinary magnetoresistance in WTe_2 . *Physical Review Letters*, 113(21), nov 2014.
- [Potter et al., 2014] A. C. Potter, I. Kimchi, and A. Vishwanath. Quantum oscillations from surface Fermi arcs in Weyl and Dirac semimetals. *Nature Communications*, 5(1):1–6, oct 2014.
- [Prange and Girvin, 1990] R. E. Prange and S. M. Girvin. *The Quantum Hall effect*. Springer-Verlag, 1990. ISBN 9780387971773.
- [Qian et al., 2014] X. Qian, J. Liu, L. Fu, and J. Li. Quantum spin hall effect in two - Dimensional transition metal dichalcogenides. *Science*, 346(6215):1344–1347, dec 2014.
- [Qu et al., 2015] F. Qu, A. J. Beukman, S. Nadj-Perge, M. Wimmer, B. M. Nguyen, W. Yi, J. Thorp, M. Sokolich, A. A. Kiselev, M. J. Manfra, C. M. Marcus, and L. P. Kouwenhoven. Electric and Magnetic Tuning between the Trivial and Topological Phases in InAs/GaSb Double Quantum Wells. *Physical Review Letters*, 115(3), 2015.
- [Ralph, 2020] D. C. Ralph. Berry curvature, semiclassical electron dynamics, and topological materials: Lecture notes for Introduction to Solid State Physics. 2020. URL <http://arxiv.org/abs/2001.04797>.
- [Ryu et al., 2010] S. Ryu, A. P. Schnyder, A. Furusaki, and A. W. Ludwig. Topological insulators and superconductors: Tenfold way and dimensional hierarchy. *New Journal of Physics*, 12(6):065010, jun 2010.

- [Sajadi et al., 2018] E. Sajadi, T. Palomaki, Z. Fei, W. Zhao, P. Bement, C. Olsen, S. Luescher, X. Xu, J. A. Folk, and D. H. Cobden. Gate-induced superconductivity in a monolayer topological insulator. *Science*, 362(6417):922–925, nov 2018.
- [Sanchez-Yamagishi et al., 2017] J. D. Sanchez-Yamagishi, J. Y. Luo, A. F. Young, B. M. Hunt, K. Watanabe, T. Taniguchi, R. C. Ashoori, and P. Jarillo-Herrero. Helical edge states and fractional quantum Hall effect in a graphene electron-hole bilayer. *Nature Nanotechnology*, 12(2):118–122, feb 2017.
- [Sharma et al., 2017] G. Sharma, P. Goswami, and S. Tewari. Chiral anomaly and longitudinal magnetotransport in type-II Weyl semimetals. *Physical Review B*, 96(4):1–6, 2017.
- [Shekhar et al., 2015] C. Shekhar, A. K. Nayak, Y. Sun, M. Schmidt, M. Nicklas, I. Leermakers, U. Zeitler, Y. Skourski, J. Wosnitza, Z. Liu, Y. Chen, W. Schnelle, H. Borrmann, Y. Grin, C. Felser, and B. Yan. Extremely large magnetoresistance and ultrahigh mobility in the topological Weyl semimetal candidate NbP. *Nature Physics*, 11(8):645–649, jul 2015.
- [Shi et al., 2019] S. Shi, S. Liang, Z. Zhu, K. Cai, S. D. Pollard, Y. Wang, J. Wang, Q. Wang, P. He, J. Yu, G. Eda, G. Liang, and H. Yang. All-electric magnetization switching and Dzyaloshinskii–Moriya interaction in WTe₂/ferromagnet heterostructures. *Nature Nanotechnology*, 14(10):945–949, 2019.
- [Šmejkal et al., 2017] L. Šmejkal, T. Jungwirth, and J. Sinova. Route towards Dirac and Weyl antiferromagnetic spintronics. *Physica Status Solidi - Rapid Research Letters*, 11(4):1700044, apr 2017.
- [Soluyanov et al., 2015] A. A. Soluyanov, D. Gresch, Z. Wang, Q. Wu, M. Troyer, X. Dai, B. A. Bernevig, A. Bernevig, B. A. Bernevig, and A. Bernevig. Type-II Weyl semimetals. *Nature*, 527(7579):495–498, nov 2015.
- [Son and Spivak, 2013] D. T. Son and B. Z. Spivak. Chiral anomaly and classical negative magnetoresistance of Weyl metals. *Physical Review B*, 88:104412, 2013.
- [Song et al., 2015] J. C. Song, G. Refael, and P. A. Lee. Linear magnetoresistance in metals: Guiding center diffusion in a smooth random potential. *Physical Review B - Condensed Matter and Materials Physics*, 92(18):180204, nov 2015.
- [Song et al., 2014] Z. Song, C. C. Liu, J. Yang, J. Han, M. Ye, B. Fu, Y. Yang, Q. Niu, J. Lu, and Y. Yao. Quantum spin Hall insulators and quantum valley Hall insulators of BiX/SbX (X=H, F, Cl and Br) monolayers with a record bulk band gap. *NPG Asia Materials*, 6(12):e147, jan 2014.
- [Sonin, 2010] E. B. Sonin. Spin currents and spin superfluidity. *Advances in Physics*, 59(3):181–255, may 2010.

- [Sürgers, 2018] C. Sürgers. Electrical switching of the anomalous Hall effect: The anomalous Hall effect in an antiferromagnet can be switched on and off using an electric field to alter the strain in the material. *Nature Electronics*, 1(3):154–155, 2018.
- [Sykora et al., 2020a] S. Sykora, A. Hübsch, and K. W. Becker. Generalized diagonalization scheme for many-particle systems. *Physical Review B*, 102(16):1–19, 2020a.
- [Sykora et al., 2020b] S. Sykora, J. Schoop, L. Graf, G. Shipunov, I. V. Morozov, S. Aswartham, B. Büchner, C. Hess, R. Giraud, and J. Dufouleur. Disorder-induced coupling of Weyl nodes in WTe₂. *Physical Review Research*, 2, 2020b.
- [Tachibana, 2017] M. Tachibana. *Beginner's Guide to Flux Crystal Growth*. NIMS Monographs. Springer Japan, 2017. ISBN 9784431565864.
- [Tan et al., 2020] A. Tan, V. Labracherie, N. Kunchur, A. U. B. Wolter, J. Cornejo, J. Dufouleur, B. Büchner, A. Isaeva, and R. Giraud. Metamagnetism of Weakly Coupled Antiferromagnetic Topological Insulators. *Physical Review Letters*, 124(19), 2020.
- [Tang et al., 2017] S. Tang, C. Zhang, D. Wong, Z. Pedramrazi, H. Z. Tsai, C. Jia, B. Moritz, M. Claassen, H. Ryu, S. Kahn, J. Jiang, H. Yan, M. Hashimoto, D. Lu, R. G. Moore, C. C. Hwang, C. Hwang, Z. Hussain, Y. Chen, M. M. Ugeda, Z. Liu, X. Xie, T. P. Devereaux, M. F. Crommie, S. K. Mo, and Z. X. Shen. Quantum spin Hall state in monolayer 1T'-WTe₂. *Nature Physics*, 13(7):683–687, jul 2017.
- [Thouless et al., 1982] D. J. Thouless, M. Kohmoto, M. P. Nightingale, and M. Den Nijs. Quantized hall conductance in a two-Dimensional periodic potential. *Physical Review Letters*, 49(6):405–408, aug 1982.
- [Thoutam et al., 2015] L. R. Thoutam, Y. L. Wang, Z. L. Xiao, S. Das, A. Luican-Mayer, R. Divan, G. W. Crabtree, and W. K. Kwok. Temperature-Dependent Three-Dimensional Anisotropy of the Magnetoresistance in WTe₂. *Physical Review Letters*, 115(4), jul 2015.
- [Wan et al., 2011] X. Wan, A. M. Turner, A. Vishwanath, and S. Y. Savrasov. Topological semimetal and Fermi-arc surface states in the electronic structure of pyrochlore iridates. *Physical Review B - Condensed Matter and Materials Physics*, 83(20):205101, may 2011.
- [Wang and Qian, 2019] H. Wang and X. Qian. Ferroelectric nonlinear anomalous Hall effect in few-layer WTe₂. *npj Computational Materials*, 5(1):1–8, dec 2019.
- [Wang et al., 2016a] Y. Wang, E. Liu, H. Liu, Y. Pan, L. Zhang, J. Zeng, Y. Fu, M. Wang, K. Xu, Z. Huang, Z. Wang, H. Z. Lu, D. Xing, B. Wang, X. Wan, and F. Miao. Gate-tunable negative longitudinal magnetoresistance in the predicted type-II Weyl semimetal WTe₂. *Nature Communications*, 7(May):1–6, oct 2016a.
- [Wang et al., 2016b] Y. Wang, K. Wang, J. Reutt-Robey, J. Paglione, and M. S. Fuhrer. Breakdown of compensation and persistence of nonsaturating magnetoresistance in gated WTe₂ thin flakes. *Physical Review B*, 93(12):121108, 2016b.

- [Wang et al., 2019] Y. Wang, L. Wang, X. Liu, H. Wu, P. Wang, D. Yan, B. Cheng, Y. Shi, K. Watanabe, T. Taniguchi, S.-J. Liang, and F. Miao. Direct Evidence for Charge Compensation-Induced Large Magnetoresistance in Thin WTe₂. *Nano Letters*, 19(6):3969–3975, jun 2019.
- [Wang et al., 2013] Z. Wang, H. Weng, Q. Wu, X. Dai, and Z. Fang. Three-dimensional Dirac semimetal and quantum transport in Cd₃As₂. *Physical Review B - Condensed Matter and Materials Physics*, 88(12):125427, sep 2013.
- [Weeks et al., 2011] C. Weeks, J. Hu, J. Alicea, M. Franz, and R. Wu. Engineering a Robust Quantum Spin Hall State in Graphene via Adatom Deposition. *Physical Review X*, 1(2):1–15, oct 2011.
- [Weng et al., 2015] H. Weng, C. Fang, Z. Fang, B. Andrei Bernevig, and X. Dai. Weyl semimetal phase in noncentrosymmetric transition-metal monophosphides. *Physical Review X*, 5(1):011029, mar 2015.
- [White and Meeson, 2002] G. K. White and P. J. Meeson. *Experimental techniques in low-temperature physics*. Oxford University Press, 4 edition, 2002. ISBN 978-0198514275.
- [Woods et al., 2017] J. M. Woods, J. Shen, P. Kumaravadivel, Y. Pang, Y. Xie, G. A. Pan, M. Li, E. I. Altman, L. Lu, and J. J. Cha. Suppression of Magnetoresistance in Thin WTe₂ Flakes by Surface Oxidation. *ACS Applied Materials and Interfaces*, 9(27):23175–23180, 2017.
- [Wu et al., 2018] S. Wu, V. Fatemi, Q. D. Gibson, K. Watanabe, T. Taniguchi, R. J. Cava, and P. Jarillo-Herrero. Observation of the quantum spin Hall effect up to 100 kelvin in a monolayer crystal. *Science*, 359(6371):76–79, jan 2018.
- [Wu et al., 2015] Y. Wu, N. H. Jo, M. Ochi, L. Huang, D. Mou, S. L. Bud'Ko, P. Canfield, N. Trivedi, R. Arita, and A. Kaminski. Temperature-Induced Lifshitz Transition in WTe₂. *Physical Review Letters*, 115(16):1–6, oct 2015.
- [Xia et al., 2009] Y. Xia, D. Qian, D. Hsieh, L. Wray, A. Pal, H. Lin, A. Bansil, D. Grauer, Y. S. Hor, R. J. Cava, and M. Z. Hasan. Observation of a large-gap topological-insulator class with a single Dirac cone on the surface. *Nature Physics*, 5(6):398–402, may 2009.
- [Xiang et al., 2018] F. X. Xiang, A. Srinivasan, Z. Z. Du, O. Klochan, S. X. Dou, A. R. Hamilton, and X. L. Wang. Thickness-dependent electronic structure in WTe₂ thin films. *Physical Review B*, 98(3):35115, 2018.
- [Xu et al., 2015] S. Y. Xu, I. Belopolski, N. Alidoust, M. Neupane, G. Bian, C. Zhang, R. Sankar, G. Chang, Z. Yuan, C. C. Lee, S. M. Huang, H. Zheng, J. Ma, D. S. Sanchez, B. K. Wang, A. Bansil, F. Chou, P. P. Shibayev, H. Lin, S. Jia, and M. Z. Hasan. Discovery of a Weyl fermion semimetal and topological Fermi arcs. *Science*, 349(6248):613–617, aug 2015.

- [Yang et al., 2011] Y. Yang, Z. Xu, L. Sheng, B. Wang, D. Y. Xing, and D. N. Sheng. Time-reversal-symmetry-broken quantum spin Hall effect. *Physical Review Letters*, 107(6):066602, aug 2011.
- [Yao et al., 2019] M. Y. Yao, N. Xu, Q. S. Wu, G. Autès, N. Kumar, V. N. Strocov, N. C. Plumb, M. Radovic, O. V. Yazyev, C. Felser, J. Mesot, and M. Shi. Observation of Weyl Nodes in Robust Type-II Weyl Semimetal WP2. *Physical Review Letters*, 122(17):176402, may 2019.
- [Yoshimi et al., 2015] R. Yoshimi, A. Tsukazaki, Y. Kozuka, J. Falson, K. S. Takahashi, J. G. Checkelsky, N. Nagaosa, M. Kawasaki, and Y. Tokura. Quantum Hall effect on top and bottom surface states of topological insulator $(\text{Bi}_{1-x}\text{Sb}_x)_2\text{Te}_3$ films. *Nature Communications*, 6(1):1–6, apr 2015.
- [Young et al., 2012] S. M. Young, S. Zaheer, J. C. Teo, C. L. Kane, E. J. Mele, and A. M. Rappe. Dirac semimetal in three dimensions. *Physical Review Letters*, 108(14):140405, apr 2012.
- [Zhang et al., 2017] E. Zhang, R. Chen, C. Huang, J. Yu, K. Zhang, W. Wang, S. Liu, J. Ling, X. Wan, H. Z. Lu, and F. Xiu. Tunable Positive to Negative Magnetoresistance in Atomically Thin WTe₂. *Nano Letters*, 17(2):878–885, feb 2017.
- [Zhang et al., 2009] H. Zhang, C.-X. Liu, X.-L. Qi, X. Dai, Z. Fang, and S.-C. Zhang. Topological insulators in Bi₂Se₃, Bi₂Te₃ and Sb₂Te₃ with a single Dirac cone on the surface. *Nature Physics*, 5(6):438–442, 2009.
- [Zhao and Wang, 2020] A. Zhao and B. Wang. Two-dimensional graphene-like Xenex as potential topological materials. *APL Materials*, 8(3):030701, mar 2020.
- [Zhao et al., 2020] B. Zhao, D. Khokhriakov, Y. Zhang, H. Fu, B. Karpiak, A. M. Hoque, X. Xu, Y. Jiang, B. Yan, and S. P. Dash. Observation of charge to spin conversion in Weyl semimetal WTe₂ at room temperature. *Physical Review Research*, 2(1):13286, 2020.
- [Zhao et al., 2015] Y. Zhao, H. Liu, J. Yan, W. An, J. Liu, X. Zhang, H. Wang, Y. Liu, H. Jiang, Q. Li, Y. Wang, X. Z. Li, D. Mandrus, X. C. Xie, M. Pan, and J. Wang. Anisotropic magnetotransport and exotic longitudinal linear magnetoresistance in WTe₂ crystals. *Physical Review B - Condensed Matter and Materials Physics*, 92(4), jul 2015.
- [Zhao and Wang, 2013] Y. X. Zhao and Z. D. Wang. Topological classification and stability of Fermi surfaces. *Physical Review Letters*, 110(24):240404, jun 2013.
- [Zheng et al., 2016] F. Zheng, C. Cai, S. Ge, X. Zhang, X. Liu, H. Lu, Y. Zhang, J. Qiu, T. Taniguchi, K. Watanabe, S. Jia, J. Qi, J. H. Chen, D. Sun, and J. Feng. On the Quantum Spin Hall Gap of Monolayer 1T'-WTe₂. *Advanced Materials*, 28(24):4845–4851, jun 2016.
- [Zyuzin and Burkov, 2012] A. A. Zyuzin and A. A. Burkov. Topological response in Weyl semimetals and the chiral anomaly. *Physical Review B - Condensed Matter and Materials Physics*, 86(11):115133, sep 2012.

Appendix A

TWO-BAND MODEL FITS OF S3 DATA

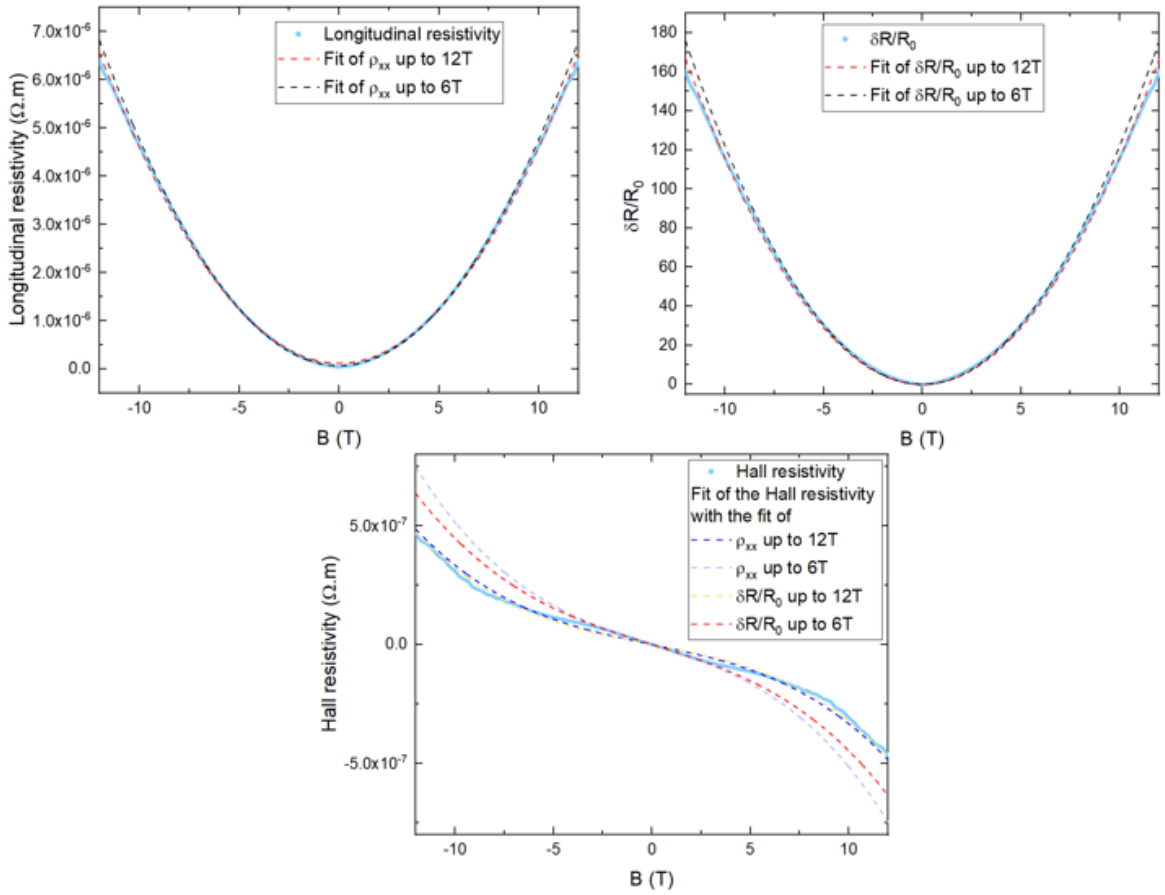


FIGURE A.1: Two-band model fit of the longitudinal resistivity, relative resistivity and Hall resistivity considering different magnetic field range at 4.2 K

In chapter 4, the analysis of the Shubnikov-de Haas oscillations show that the electron and hole carrier densities were equal to $3 \times 10^{19} \text{ cm}^{-3}$. Considering the two-band model approximation to fit our data, it was shown that all the samples were not giving this same carrier densities. To complete this discussion, the longitudinal resistivity and Hall resistivity of the sample S3 are fitted considering different magnetic field ranges and the relative resistivity $\delta R/R_0$ instead of the longitudinal

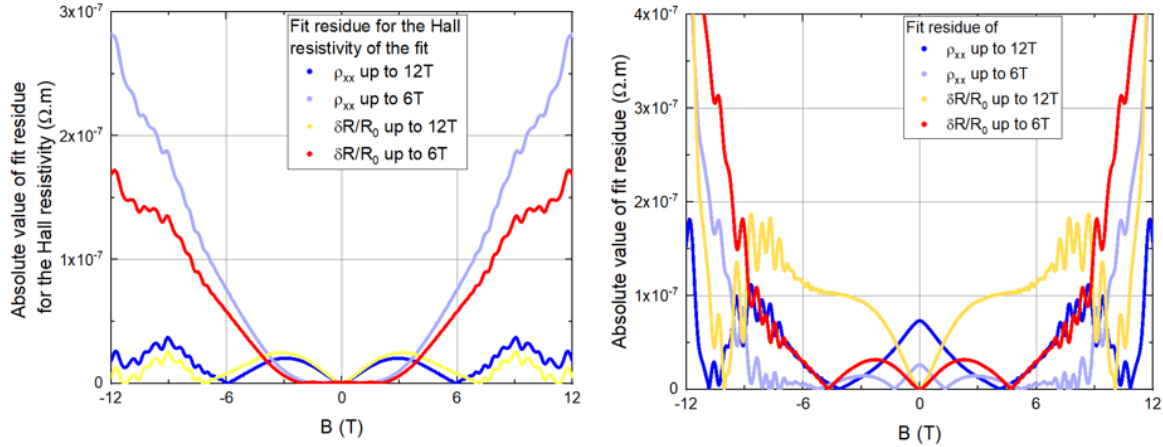


FIGURE A.2: Residue of the two-band model fit of the longitudinal resistivity, relative resistivity (multiplied by ρ_0 to be able to compare it with the residue of the longitudinal resistivity fit) and Hall resistivity considering different magnetic field range at 4.2 K

one. As shown in figure A.1, the longitudinal resistivity is best fitted at low magnetic field for the range up to 6 T contrary to 12 T but also taking into account the relative resistivity. As a consequence, the parameters given for these fits are approaching the carrier densities extracted from the SdHO. These fits confirms the limited range to use the two-band model to do a quantitative analysis of the extremely large magnetoresistance.

We note also that reducing the magnetic field range of the fit leads to better reproduce the Hall resistivity. The departure of this fit from the data at higher magnetic field cannot be considered due to the possible reduction of the signal from the contacts too deep in the structure as mentioned in chapter 4. This results also in a correction of the parameters and could lead on a deviation from the carrier densities of the Shubnikov-de Haas. Nevertheless, as you can see, the longitudinal resistivity is one order of magnitude higher than the Hall resistivity, hence reducing the error of the Hall resistivity on this fit. A similar weight were made for the fit between the Hall resistivity and relative resistivity.

Appendix B

TYPE II WEYL SEMIMETALS INFORMATIONS

In the conclusion, we discussed shortly the difference between the different type II Weyl semimetals and the possibility to see the negative magnetoresistance in other materials of this type. The table B.1 below contains the informations of the non-centrosymmetric type II Weyl semimetals such as :

1. the irreducible number of Weyl nodes and the total number due to reflections,
2. how the Fermi arcs connect the different Weyl nodes,
3. the position in energy of the Weyl nodes,
4. if it is possible, the position in energy where an XMR was seen due to charge compensation.

Material	Number of Weyl nodes	Energy of the Weyl node (in eV)			Compensation	References
		W1	W2	W3		
WTe ₂	2 irreducible reflected 4× for a total of 8	52	58	/	XMR at E _F	[Soluyanov et al., 2015]
MoTe ₂	8 as in WTe ₂	20	30	/	XMR at E _F	[Deng et al., 2016] [Huang et al., 2016]
W _{0.75} Mo _{0.25} Te ₂	8 as in WTe ₂	5	60	/	No data	[Belopolski et al., 2016]
WP ₂	2 irreducible of same chirality, Fermi arc connect k _y to opposite chirality at -k _y	-471	-364	/	XMR 60 meV above E _F	[Yao et al., 2019] [Kumar et al., 2017]
MoP ₂	8 as in WP ₂	-410	-364	/	Energy of the XMR not given compare to DFT	[Yao et al., 2019] [Autès et al., 2016] [Kumar et al., 2017]
TaIrTe ₄	1 irreducible node, the Fermi arcs connecting k _y to opposite chirality at -k _y	83	/	/	No data	[Koepernik et al., 2016] [Belopolski et al., 2017]
NbRhTe ₄	8 as in WTe ₂ but the Fermi arcs connect reflection even though the 2 nodes next to each other have different chiralities	125	-66	/	No data	[Liu et al., 2020]
NbIrTe ₄	3 irreducible, 2 type II and 1 type I, 1 type II is reflected 8× due to non-nul k _z for a total of 16 Weyl nodes	142	140	-84	Energy of the XMR not given compare to DFT	[Li et al., 2017a]

TABLE B.1: Non-centrosymmetric type II Weyl semimetals list with the number of Weyl nodes, the Fermi energy of these nodes and if the XMR due to charge compensation was observed and if so at which Fermi energy.

Appendix C

COLD FINGER DESIGN

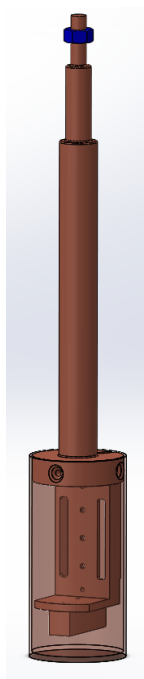


FIGURE C.1: Drawing made by Solidworks of the new cold finger that will be used on the He-3 system

During my PhD work, I designed a new cold finger for a new Helium-3 system that I present here as an appendix. A cold finger is the bottom part of an insert that is screwed in the coldest part of it. Due to the large decrease of heat conductivity of most of materials at very low temperature, this part need to be well designed to handle the thermalization of the sample and to be well anchor to the cold part of the insert [Ekin, 2006]. For this purpose, the cold finger was made in copper free-oxygen and then was gold plated due to the property of the material to catch oxygen and degas during pumping. The design for this insert was made with the software Solidworks (figure C.1). A particularity of transport measurements in nanostructures is that we connect this nanostructures to a chip carrier. This carrier chip is then

plugged on the cold finger. The need to apply a large magnetic field in different directions of the sample lead to a removal of the wire bound that could damage the structure. To avoid this, it is possible to use small adaptator to put the sample in different directions. In a dilution fridge or ^3He system, the space allocated to the chip carrier is small and the possibility to use an adaptator is not possible. For this purpose, I designed a cold finger with two different positions for the chip carrier to be plugged. The thermalization of the sample is managed by a small cylinder that enclose the sample part. When the cold finger is screwed in the insert, a bolt is used to avoid the cold finger to rotate and also tighten the gasket between the cold finger and the cold part of the insert.

LIST OF FIGURES

1	Illustration of the band structure of WTe_2	16
1.1	Path \mathcal{C} in the parameter space followed by the system to acquire a Berry phase	21
1.2	Foucault's pendulum at the Pantheon in Paris	21
1.3	Comparison of 2 classes of 3D objects (genus equal to 0 and 1)	22
1.4	Classification of topological states in quantum matter	24
1.5	Representation of the interface between a normal insulator and a Quantum Hall state/a Quantum spin Hall state	26
1.6	Edge channel in a 2DTI Hall bar	27
1.7	Quantum spin hall phase and conductance plateaus	28
1.8	WTe_2 : a QSHI and a superconductor in its 2D limit	29
1.9	Band structures of Bi_2Se_3 family materials	30
1.10	Topological elements to create new topological phases	31
2.1	a) Representation of an heterostructure made of topological insulator layers intercalated with normal insulator layers; b) Phase diagram of the heterostructure for a spin splitting $m = 0$ and $m \neq 0$. Adapted from [Burkov and Balents, 2011]	34
2.2	Schematic of different band structure in topological semimetal, from left to right : Dirac Semimetal, Weyl type I and type II semimetal	36
2.3	Weyl semimetal topological properties	38
2.4	Temperature dependence of the anomalous Hall effect under zero field in Mn_3Ge	39
2.5	Comparison of the anomalous Hall angle as a function of the anomalous Hall conductivity in different materials	40
2.6	Perpendicular magnetoresistance of NbP measured at different temperatures up to 9 T	41
2.7	Chiral anomaly in a Weyl semimetal	42
2.8	Band structure and extremely large magnetoresistance in WTe_2	44
2.9	Subquadratic behavior of the XMR	45
2.10	Fermi-arc-induced Weyl orbit in WTe_2	46

2.11	Indication of Weyl type II semimetals in WTe_2	47
2.12	Planar Hall effect in WTe_2	50
3.1	Crystal structure of WTe_2	52
3.2	Optical image of a YSZ substrate after CVT growth showing nanosheets (orange arrows) and clusters (green arrows) of WTe_2 randomly distributed on its surface	53
3.3	EDX measurement (30 kV) of a bulky crystal cluster showing the composition expected for WTe_2 . Adapted from [Hansen et al., 2020]	55
3.4	Polarized Raman spectroscopy on CVT growth structures	55
3.5	TEM analysis of a nanosheet of WTe_2	56
3.6	SEM electron microscopy image of a WTe_2 cleaved macrocrystal from Te-flux growth and EDX analysis	57
3.7	Exfoliated sample on SiO_2 substrate, 30 nm structure	58
3.8	Exfoliated sample on SiO_2 substrate, sample S3	59
3.9	Optical images of three WTe_2 nanostructures grown by CVT with their respective dimensions (in-plane in red, thickness in blue).	60
3.10	Nanofabrication process, step by step on SiO_2/Si and YSZ substrates	61
3.11	Optical images of CVT and exfoliated nanostructures connected	62
3.12	Schematic of a dilution fridge	64
4.1	Temperature dependence of the longitudinal resistivity of the nanostructures S2 and S3	69
4.2	Longitudinal and Hall resistivity of sample S1 fit with a two-band model	70
4.3	Longitudinal and Hall resistivity of sample Exf fit with a two-band model	71
4.4	Resistance with the background removed as a function of the magnetic field up to 12 T showing clear Shubnikov-de Haas oscillations	73
4.5	FFT analysis of the Shubnikov-de Haas oscillations in sample S3	74
4.6	Sample comparisons of MR vs B in log log scale	75
4.7	Longitudinal resistivity as a function of a perpendicular magnetic field in a two-band model for different ratio n_h/n_e	78
4.8	Mapping of the power law exponent α in the framework of a three-band model	79
4.9	Three-band model fit for the relative magnetoresistance and the Hall resistivity for the sample S3	80
4.10	Coefficient α of the power-law, top : as a function of the amplitude of the disorder for a correlation length $\zeta = 5$ nm; bottom : as a function of the correlation length of the disorder for an amplitude of the disorder $V = 5$ meV. The line is a guide for the eye.	84

4.11	Numerical calculations of the XMR for two different disorder, orange circle corresponding to an XMR with $\xi = 5$ nm and $V = 5$ meV and blue circle with $\xi = 5$ nm and $V = 15$ meV.	86
5.1	Angular dependence of the resistance for sample S3, measured at $T = 4.2$ K and with a 2 T magnetic field	90
5.2	In-plane magneto-resistance of samples S1, S2 and S3, as measured at $T = 4.2$ K	91
5.3	Temperature dependence of the different samples below 4K	92
5.4	In-plane magnetoresistance of S1, measured at 100 mK	93
5.5	Evolution of the magnetoresistance for different temperatures of S1	94
5.6	a) Comparison of the relative magnetoresistance $\Delta R(B) = R(T = 100 \text{ mK}, B) - R(T = 4.2 \text{ K}, B)$ of S1 for the three different magnetic field direction, b) Temperature dependence of the relative resistance $(R(T) - R(4.2 \text{ K})) / R(4.2 \text{ K}, B = 0 \text{ T})$ of S1 as a function of an out-of-plane magnetic field, showing both the temperature-dependent negative MR and the temperature independent positive MR	94
5.7	Hall resistivity as a function of an out-of-plane magnetic field of S1 for different temperatures and a current of 1 μA	95
5.8	Numerical calculations of the chemical potential μ vs B	96
5.9	Sketch of the modification of the band structure with a Zeeman energy in a) a trivial metal, b) a Weyl semimetal.	97
5.10	Numerical simulation of the magnetoresistivity at 0 K	98
5.11	Density of states of WTe_2 calculated around the compensation	99
A.1	Two-band model fit of the longitudinal resistivity, relative resistivity and Hall resistivity considering different magnetic field range at 4.2 K	119
A.2	Residue of the two-band model fit of the longitudinal resistivity, relative resistivity (multiplied by ρ_0 to be able to compare it with the residue of the longitudinal resistivity fit) and Hall resistivity considering different magnetic field range at 4.2 K	120
C.1	Cold finger for He-3 system	123

LIST OF TABLES

3.1	Thickness distribution of WTe_2 nanostructures grown by CVT on 2 different YSZ substrates	59
4.1	Informations on the different samples measured	70
4.2	Carrier densities and mobilities for different two-band model fit of the relative resistance, longitudinal and Hall resistivity of S1, S3 and S4	72
B.1	Non-centrosymmetric type II Weyl semimetals list with the number of Weyl nodes, the Fermi energy of these nodes and if the XMR due to charge compensation was observed and if so at which Fermi energy. . . .	122

LIST OF PUBLICATIONS

- A. Tan, V. Labracherie, N. Kunchur, A. U.B. Wolter, J. Cornejo, J. Dufouleur, B. Büchner, A. Isaeva, and R. Giraud, "Metamagnetism of Weakly Coupled Antiferromagnetic Topological Insulators", *Phys. Rev. Lett.* 124, 197201 (2020)
- G. Shipunov, I. Kovalchuk, B. R. Piening, V. Labracherie, A. Veyrat, D. Wolf, A. Lubk, S. Subakti, R. Giraud, J. Dufouleur, S. Shokri, F. Caglieris, C. Hess, D. V. Efremov, B. Büchner, and S. Aswartham, "Polymorphic PtBi₂: Growth, structure, and superconducting properties", *Phys. Rev. Materials* 4, 124202 (2020)
- A. Veyrat, V. Labracherie, R. Acharya, D. L. Bashlakov, F. Caglieris, J. I. Facio, G. Shipunov, L. Graf, J. Schoop, Y. Naidyuk, R. Giraud, J. van den Brink, B. Büchner, C. Hess, S. Aswartham, J. Dufouleur, "Berezinskii-Kosterlitz-Thouless transition in the Weyl system PtBi₂", arXiv:2101.01620

Long résumé en Français

Transport électrique dans des nanostructures du semimétal de Weyl WTe_2

par Valentin LABRACHERIE

Une limitation majeure du développement des équipements électroniques d'aujourd'hui est la consommation électrique. Depuis la loi de Moore, le nombre de transistors intégré dans les circuits électriques a doublé chaque année depuis plusieurs décennies. Alors que les dimensions des composants logiques n'a cessé de diminuer, la consommation électrique due aux interconnexions est devenue si large qu'elle peut chauffer les composants adjacents jusqu'à même les endommager. Une possibilité de régler ce problème et d'utiliser des courants de spins au lieu de courants électriques, qui peuvent aussi être sans dissipation [Sonin, 2010] [Šmejkal et al., 2017]. Dans cette branche de la spintronique, des nouveaux matériaux sont étudiés afin d'en trouver pouvant générer, détecter et manipuler des larges courants de spins, ou simplement les propager. Une classe de ces matériaux sont les matériaux dits topologiques qui possèdent une texture de spin dite "chirale" due à fort couplage spin-orbite, avec des quasiparticules robustes contre les perturbations, plus particulièrement au désordre.

Parmi ces matériaux, les semimétaux topologiques de Weyl ont été rapidement identifiés comme une nouvelle famille de matériaux d'intérêt pour investiguer le transport de spins chiraux. Parmi les bandes massives, la structure de bande de volume montre une dispersion linéaire associée à des fermions de Weyl possédant une chiralité de spin bien définie [Armitage et al., 2018]. Ainsi, contrairement aux isolants topologiques 3D, les semimétaux de Weyl ont des états de surface topologiques mais aussi des propriétés topologiques de volume. Ces états de volume viennent de paires avec des cônes de Dirac de chiralité de spin opposée, appelés cônes de Weyls, liés l'un à l'autre par des arcs de Fermi qui connectent leur projection sur la surface. Important pour leur transport en volume, ces paires de nœuds de Weyl sont des sources ou puits parfaits de courbure de Berry. Chaque cône ayant sa propre chiralité, les fermions de Weyl sont prédits pour produire de nouveaux effets de transport comme un important effet Hall anormal ou une magnéto-résistance négative liée à l'anomalie chirale. Ce dernier effet résulte d'une anomalie quantique qui se traduit par un transfert de charge entre les deux cônes de chiralité opposés, pour des champs électriques (E) et magnétiques (B) parallèles. Puisque l'anomalie chirale n'existe que pour B appliqué suivant la direction de E , ceci est associé à une magnéto-résistance anisotrope et, ainsi, pourrait contribuer à un effet Hall planaire.

Une magnéto-résistance anisotropique et un effet Hall planaire ont en effet été reporté pour des films minces de WTe_2 , un semimétal de Weyl de type II. Différents groupes ont été étudié l'effet Hall planaire anisotropique [Li et al., 2019b] ou l'anomalie chirale [Wang et al., 2016a] [Li et al., 2017b] [Lv et al., 2017] [Zhang et al., 2017]. Pour des échantillons très fin, en-dessous de 10 nm, une ouverture progressive du gap apparaît [Zheng et al., 2016]. Dans le cas de quelques couches ou monocouche, des études récentes ont révélés les effets de la courbure de Berry sur les propriétés de transport. L'observation d'un effet Hall anormale non-linéaire a été reportés [Kang et al., 2019] [Ma et al., 2019] [Wang and Qian, 2019] et l'effet Hall quantique de spin a été mis en évidence [Tang et al., 2017] [Fei et al., 2017] [Wu et al., 2018]. WTe_2 a une structure non-centrosymétrique avec un fort couplage spin-orbit qui prédit une large contribution à l'effet Hall de spin [Zhao et al., 2020]. Plusieurs études se concentre sur les potentiels applications des propriétés du matériau pour le développement de source de courant de spins dans des composants logiques [Shi et al., 2019] [Zhao et al., 2020]. Du à sa nature de Weyl de type II, la structure de bande spécifiques de WTe_2 est composé d'un croisement entre des bande de conduction et de valences, menant à la coexistence de poches de trous et d'électrons, pour laquelle une parfaite compensation de charge est possible. Une étude des oscillations de Shubnikov-de Haas de volume et dans des films minces ont montrés un changement de la structure de bandes pour des échantillons d'épaisseur comprises entre 10 et 40 nm, les bandes de trous descendant en énergie alors que les bandes d'électrons montés [Xiang et al., 2018]. Ce changement a pour conséquences une modification des densités de porteurs de trou et d'électron a la compensation parfaite. La coexistence de trou et d'électron a pour conséquence l'apparition d'une magnéto-résistance extrêmement large mise en évidence dans des macrocristaux [Ali et al., 2014] [Luo et al., 2015] et des films minces [Thoutam et al., 2015]. Cette magnéto-résistance n'est pas liés à des propriétés topologiques mais est de grand intérêt pour extraire des paramètres de transport comme les mobilités et densités de porteurs.

Cependant, de simples considérations basés sur la structure de bande simplifiés, comme montré en figure 1, apporte déjà importantes questions à propos de l'interprétation de certains résultats de transport en termes de propriétés topologiques. Premièrement, les noeuds de Weyl sont bien au-dessus de l'énergie où la compensation de charge a lieu, a peu près 50 meV. Cela apporte certains doute sur l'apparition de la XMR et l'anomalie chirale pour un dopage donné. En général, l'énergie de Fermi de WTe_2 est positionné dans le régime de compensation de charge, et la XMR est bien mise en évidence à basse température. Cela implique que l'observation de l'anomalie chirale n'est pas possible à ce niveau de Fermi. Une autre importante caractéristique lié à la XMR n'a pas été étudié à sa racine : il a été

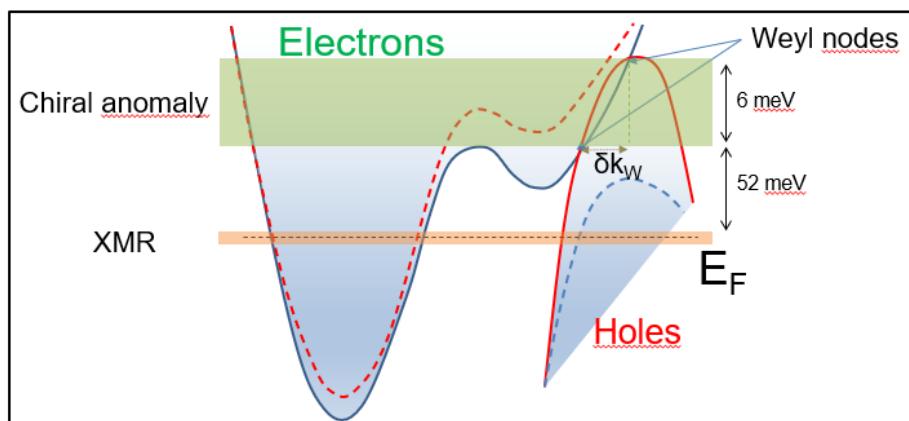


FIGURE 1: Illustration de la structure de bande de WTe_2 avec les noeuds de Weyl indiqués par les flèches. La dégénérescence de spin des bandes de valences et de conduction sont levés par le couplage spin-orbit, menant à deux bands peu shiftés en energy (lignes pleines et en tirets). Deux niveaux d'énergie sont indiqués dans la structure de bande, en orange pour la compensation parfaite ($n = p$), menant à des poches de trous et d'électron contribuant au transport et en vert où la réalisation de l'anomalie chirale a lieu.

reporté que la structure de bande peut être approximé par un modèle 2 bandes à la compensation parfaite ce qui mène a une magnétorésistance quadratique sans saturation même à haut champ magnétique aussi haut que 60 T [Ali et al., 2014]. Cependant, une loi sous-quadratique a toujours été reporté sans explication [Thoutam et al., 2015] [Wang et al., 2016b] [Fatemi et al., 2017] [Wang et al., 2019]. Deuxièmement, même si l'énergie de Fermi pourrait être amené au niveau des noeuds de Weyl, l'influence du désordre ne peut pas être négligé puisque les diffusions entre noeuds peuvent efficacement supprimer les contributions topologiques au transport de charge [Sykora et al., 2020b]. Comme discuté dans la thèse (chapitre 5), la magnétorésistance négative peut être attribué aux propriétés non-topologiques de la structure de bandes loin des noeuds de Weyl, au-delà de la transition de Lifshitz.

Dans cette thèse, la XMR positive à haut champ et la magnétorésistance négative à bas champ sont étudiés en détails, en regardant les propriétés de magnéto-transport de nanostructures de WTe_2 désordonnées et obtenus par différentes méthodes de croissance, avec différent degrés de désordre. Ce manuscrit est divisé en cinq chapitres. Le chapitre 1 donne une introduction générale des concepts topologiques, avec une revue de l'effet Hall quantique entier et des isolants topologiques. Dans le chapitre 2, la phase des semimétaux topologiques de Weyl est introduite, et les propriétés de transport spécifiques sont discutées. Dans le chapitre 3, les méthodes de croissances, la nanofabrication et le set-up de mesure sont décrits en détails. Les deux derniers chapitre se concentrent sur les résultats obtenus durant la thèse. Le chapitre 4 rapporte l'étude menés sur les propriétés de transport de WTe_2 entrepris à

fort champs (12 T) et décrit la magnéto-résistance extrêmement large dans la cadre d'un modèle multi-bandes. L'influence du désordre, son amplitude et sa portée, sur la XMR est étudié en comparant des résultats obtenus avec des nanostructures avec différentes densités de défauts et des simulations numériques. Dans le chapitre 5, une magnéto-résistance négative est nouvellement interprété comme l'influence de fermions de Weyl loins des noeuds, comme montré par des simulations numériques. Notre étude expérimental montre des preuves solides pour rejeter la possibilité d'une conséquence de l'anomalie chirale pour cette magnéto-résistance négative dans WTe_2 . Au lieu de cela, un nouveau mécanisme identifié dans ce travail révèle qu'une contribution topologique au transport de charge existe aussi pour un niveau de Fermi positionnée dans le régime de compensation, même loin des noeuds de Weyl, une condition réalisée dans WTe_2 .

Lange abstrakt auf Deutsch

Elektrischer Transport in Nanostrukturen des Weyl-Halbmietalls WTe_2

von Valentin LABRACHERIE

Heutzutage ist eine entscheidende Beschränkung in der Entwicklung von elektronischen Geräten der Energieverbrauch. Nach dem Moor'schen Gesetz hat sich die Anzahl an Transistoren in integrierten Schaltkreisen seit Jahrzehnten jedes Jahr verdoppelt. Während die Größe der logischen Komponenten stetig sinkt, steigt der Energieverbrauch auf Grund von Schaltungsverbindungen so sehr, dass die Komponenten im Umfeld stark aufgeheizt und beschädigt werden können. Eine mögliche Lösung dieses Problems ist es Spinströme zu nutzen, die sogar dissipationslos sein können [Sonin, 2010] [Šmejkal et al., 2017]. In diesem Bereich der Spintronik werden neue Materialien erforscht, die starke Spinströme generieren, finden und manipulieren können oder sie weitertragen können. Eine Klasse von Materialien, die diese Eigenschaften besitzen, sind topologische Materialien, die chirale Spinstrukturen auf Grund starker Spinbahnkopplung haben, sowie lückenlose Quasiteilchen, die widerstandsfähig gegenüber Perturbationen, die beispielsweise durch Unordnung auftreten, sind.

Topologische Weyl Halbmietalle wurden schnell als wichtige Gruppe von Materialien identifiziert, die auf chiralen Spintransport untersucht werden können. Abgesehen davon, dass sie sehr große Bänder besitzen, zeigt ihre Bandstruktur in der Masse lineare Excitationen der Quasipartikel, die sich Weyl Fermionen nennen und eine gut definierte Chiralität der Spins besitzen [Armitage et al., 2018]. Im Gegenteil zu 3D topologischen Isolatoren haben Weyl Halbmietalle topologische Oberflächenzustände, aber auch lückenlose topologische Massenzustände. Diese Massenzustände sind Paare von Dirac Kegeln mit entgegengesetzten Spin Chiralitäten, die Weyl Kegel genannt werden und durch ihre Fermibögen verknüpft sind, die auf der Oberfläche durch ihre Projektionen verbunden sind. Ein wichtiger Aspekt der Transporteigenschaften ist die Tatsache, dass die Weyl Knoten eine ideale Quelle und Abfluss für die Berrykrümmung sind. Da jeder Kegel eine eigene Chiralität besitzt, ist zu erwarten, dass die Weyl Fermionen neue Effekte, wie zum Beispiel einen starken, intrinsisch-anomalen Hall Effekt oder negativen Magnetowiderstand, der auf die chirale Anomalie zurückzuführen ist, verursachen. Die chirale Anomalie ist auf eine Quantenanomalie zurückzuführen, die einen Ladungsträgeraustausch zwischen Kegeln mit entgegengesetzten Chiralitäten verursacht, wenn das elektrische (E) und das magnetische (B) Feld parallel zueinander sind. Da die chirale Anomalie

nur dann existiert, wenn B und E parallel sind, wird diese mit einem anisotropischen Magnetowiderstand assoziiert und dementsprechend wirkt sie sich auch auf den planaren Hall Effekt aus.

Ein anisotropischer Magnetowiderstand und der planare Hall Effekt wurden in der Tat bereits in dünnen Schichten von Typ II Weyl Halbmetallen, wie beispielsweise WTe_2 , nachgewiesen. Verschiedene Gruppen haben den anisotropisch-planaren Hall Effekt [Li et al., 2019b] und die chirale Anomalie untersucht [Wang et al., 2016a] [Li et al., 2017b] [Lv et al., 2017] [Zhang et al., 2017]. In sehr dünnen Proben, unter 10 nm, öffnet sich die Bandlücke von WTe_2 langsam. Des Weiteren wurden in jüngsten Studien die Auswirkungen der Berrykrümmung im wenig bis einlagigem Limit auf ihre Transporteigenschaften untersucht. In diesen wurde von einem nichtlinearen anomalen Hall Effekt [Kang et al., 2019] [Ma et al., 2019] [Wang and Qian, 2019], sowie von einem quanten Spin Hall Effekt [Tang et al., 2017] [Fei et al., 2017] [Wu et al., 2018]. Außerdem führt die nichtzentrosymmetrische Struktur von WTe_2 mit starker Spinbahnkopplung zu der Vorhersage eines sehr großen Spin Hall Effekts [Zhao et al., 2020]. Verschiedene Studien haben sich auf eine Anwendung der Eigenschaften von WTe_2 auf die Entwicklung von Spinstromquellen spezialisiert, die Anwendung in Datenspeichern und Logischen Geräten findet. Auf Grund seiner spezifischen Bandstruktur, die auf die Typ II Eigenschaften des Systems zurückzuführen ist, besitzt WTe_2 eine Überlappung der Valenz und Leitungsbänder, welche eine Koexistenz von Elektronen und Löchern hervorruft, die wiederum Ladungsträgerkompensation möglich macht. Eine Studie der Shubnikov-de Haas Oszillationen in sowohl Massen, als auch in dünnen Schichten hat ergeben, dass sich die Bandstruktur im Bereich zwischen 40 und 10 nm dahingehend verändert, dass die Lochbänder weniger Energie besitzen als zuvor und die Elektronenbänder mehr Energie aufweisen [Xiang et al., 2018]. Diese Veränderung führt zu verschiedenen Ladungsträgerkonzentrationen bei idealer Kompensation vom Massen- zum dünn-schichtigen Zustand, wenn dieser dünner als 40 nm ist. Die Elektronen-Loch Koexistenz führt zu einem extrem großen Magnetowiderstand, der sowohl in der Masse [Ali et al., 2014] [Luo et al., 2015], als auch in dünnen Schichten nachgewiesen wurde [Thoutam et al., 2015]. Dieser Magnetowiderstand ist nicht auf die topologischen Eigenschaften von WTe_2 zurückzuführen, ist aber trotzdem von großem Interesse bei der Ableitung von Transportparameter, wie beispielsweise Ladungsträgermobilitäten und -konzentrationen.

Nichtsdestotrotz werfen simple Annahmen der vereinfachten Bandstruktur, wie in Figur 1 skizziert, bereits wichtige Fragen zu der Interpretation der Transportergebnisse im Bezug auf die topologischen Eigenschaften auf. Erstens sind die

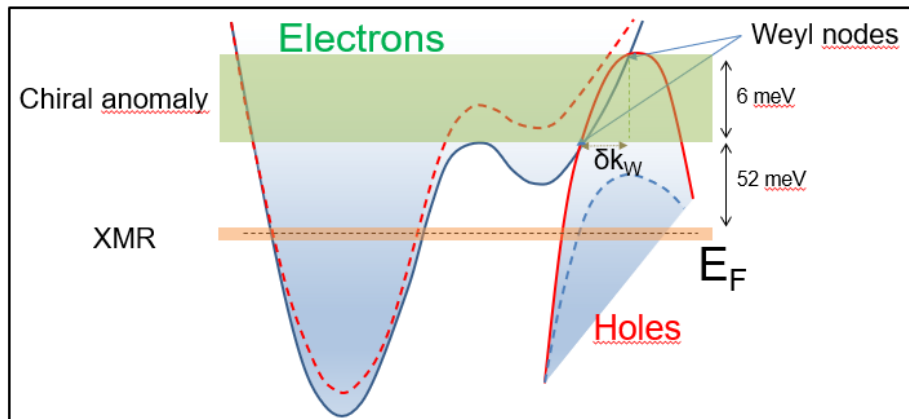


FIGURE 1: Illustration der Bandstruktur von WTe₂ in der die Weyl Knoten als zwei Pfeile angegeben sind. Die Entartung der Spins in den Leitungs- und Valenzbändern wird durch die Spinbahnkopplung aufgehoben und führt zu der Existenz von zwei unterschiedlichen Bändern die leicht verschobene Energien besitzen (durchgezogene und gestrichelte Linien). Zwei wichtige Energieniveaus sind hier in der Bandstruktur angegeben, ein Niveau für die ideale Kompensation ($n = p$) in orange, was zu zwei nichtentartete Elektronen- und Lochtaschen führt, die zum Transport beitragen und in grün, dort wo die Verwirklichung der chiralen Anomalie auftritt.

Weyl Knoten um ca. 50 meV von der Ladungsträgerkompensationsenergie verschoben. Dies wirft Unsicherheiten bei der Beobachtung von sowohl der XMR und der chiralen Anomalie für eine bestimmte Ladungsträgerdotierung auf. Im Allgemeinen ist die Fermienergie in WTe₂ nahe dem Ladungsträgerkompensationsbereich gelegen und die XMR kann außerdem bei tiefen Temperaturen nachgewiesen werden. Das bedeutet, dass die Beobachtung der chiralen Anomalie bei einer solchen Energie unwahrscheinlich ist. Eine weitere Besonderheit die dem extrem großen Magnetowiderstand zugeordnet werden kann, hat bisher noch keinen Ursprung: es wurde berichtet, dass die Bandstruktur an der idealen Kompensation durch ein Zweibandmodell angenähert werden kann, welches zu einem quadratischen Magnetowiderstand ohne Sättigung, auch bei hohen Magnetfeldern von bis zu 60 T, führen kann [Ali et al., 2014]. Nichtsdestotrotz wurde schon vermehrt von einem subquadratisches Gesetz ohne Erklärung berichtet [Thoutam et al., 2015] [Wang et al., 2016b] [Fatemi et al., 2017] [Wang et al., 2019]. Zweitens, selbst wenn die Fermienergie bis zu den Weyl Knoten hochgebracht werden kann, darf der Einfluss der Unordnung nicht vernachlässigt werden, da Streuung innerhalb der Knoten die topologische Beteiligung am Ladungsträgertransport effizient unterdrücken kann [Sykora et al., 2020b]. Wie im Kapitel 5 diskutiert wird, kann der negative Magnetowiderstand der nicht trivialen Topologie der Bandstruktur weit weg der Weyl Knoten und weit von dem Lifshitz-Übergang entfernt, zugeordnet werden.

In dieser Dissertation werden sowohl der positive Magnetowiderstand bei

hohen Feld, als auch der negative niedrig-Feld Magnetowiderstand im Detail betrachtet, indem die Magnetotransporteigenschaften von WTe_2 Nanostrukturen, die verschiedene Grade von Unordnung aufweisen und mit verschiedenen Wachstumsprozessen hergestellt sind, untersucht wurden. Das Manuskript besitzt fünf Kapitel. Im ersten Kapitel wird eine allgemeine Einleitung zu topologischen Konzepten gegeben mit einer Zusammenfassung von sowohl dem Quanten Hall Effekt, als auch topologischen Isolatoren. Im zweiten Kapitel wird die Weyl Halbmetallphase vorgestellt und ihre speziellen Transporteigenschaften diskutiert. Im dritten Kapitel werden die Wachstumsprozesse im Detail vorgestellt, sowie die Nanoherstellungsprozesse und der Aufbau der Transportmessungen. Die letzten zwei Kapitel befassen sich mit den Ergebnissen, die während dieser Doktorarbeit erlangt wurden. Kapitel 4 berichtet von der Studie der Transporteigenschaften von WTe_2 in hohen Magnetfeldern und beschreibt den extrem großen Magnetowiderstand mit Bezug auf das Multibandmodell. Der Einfluss der Stärke der Unordnung und der Reichweite dieser (langer im Vergleich zu kurzer Reichweite) auf den extrem großen Magnetowiderstand wird des Weiteren untersucht, indem die Ergebnisse von Nanostrukturen mit verschiedenen Dichten von Punktdefekten mit numerischen Berechnungen verglichen werden. In Kapitel 5 wird der negative Magnetowiderstand als Einfluss der Weyl Fermionen weit weg von den Weyl Knoten neu interpretiert, was durch die numerischen Berechnungen gefestigt wird. Unsere experimentelle Studie erweist sich als ausreichender Beweis, um die chirale Anomalie als Ursprung des negative Magnetowiderstand in WTe_2 auszuschließen. Ferner, wird ein neuer Mechanismus identifiziert, der den nichttrivialen, topologischen Beitrag zum Ladungsträgertransport beschreibt, welcher auch für eine Fermienergie im Ladungsträgerkompensationsbereich existiert, auch wenn diese weit weg von den Weyl Knoten in WTe_2 ist.

Declaration of Authorship

I herewith declare that I have produced this paper without the prohibited assistance of third parties and without making use of aids other than those specified; notions taken over directly or indirectly from other sources have been identified as such. This paper has not previously been presented in identical or similar form to any other German or foreign examination board.

The thesis was produced at the IFW Dresden (Germany) and Spintec (France) under the scientific supervision of Prof. Dr. Berndt Büchner and Dr. Romain Giraud.

Signed:



Date:

29.04.2021